THE UNIVERSITY OF WARWICK

Development and Application of Evanescent Wave Cavity Ring-Down Spectroscopy for Studies of Electrochemical and Interfacial Processes

by

Mathias Schnippering

A thesis submitted for the degree of Doctor of Philosophy

University of Warwick

Department of Chemistry

December 2009

Für meine Eltern

Contents

List of Figures

List of Tables

Acknowledgements

Firstly, I would like to thank Prof. Pat Unwin for his help, support and advice throughout this PhD. Without his enthusiasm and encouragement, this thesis would not have been possible. Thanks must go to Dr. Stuart Mackenzie at the University of Oxford and Dr. Mikhail Mazurenka whose help and expertise was invaluable. I would like to thank Prof. Julie Macpherson for all her support and Dr. Vas Stavros for much needed advice in laser spectroscopy. Also thanks to our collaborates at the Chemical Engineering Department of the University of Cambridge, Dr. Johan Hult and Dr. Toni Laurila as well as Dr. Justin Langridge from the Chemistry Department of the University of Cambridge.

Special thanks must go to my lab buddy Hayley Powell without her continuous support (finite element modelling and common sense) and her cheerfulness nothing would have worked in the lab. Also thanks to Dr. Meiqin Zhang for all her help with electrochemical measurements.

I would also like to than all the members of the Electrochemistry and Interfaces group at Warwick. Huge thanks especially to the „C111 crew" (past and current members) for all their support and friendship. Thanks to Massimo, Martin and Mike OC for all the useful scientific and non-scientific discussions.

Thank to Marcus Grant and Lee Butcher in mechanical workshop for all their help. I would also like to thank our neighbours, the Tim Jones group, especially Stefan, Lara, Virendra, Jay, Tom, Paul, Luke, Edd and Ian for all the good time we had and have. Special thanks must go to Nicola for her help, support and understanding through the last year of this PhD. Finally I would like to thank my family, especially my parents, for all their emotional support throughout this degree.

Declaration

The work presented in this thesis is entirely original and my own work, except where acknowledged in the text. I confirm that this thesis has not been submitted for a degree at another University.

The theoretical models presented in chapter 4 and 6 were created together with Hayley Powell. Hayley Powell also contributed to evanescent wave cavity ring-down spectroscopy and UV-vis experiments in chapter 6. Dr. Meiqin Zhang performed the scanning electrochemical microscopy experiments in chapter 5.

Broadband cavity enhanced absorption spectroscopy was carried out in collaboration with Mikhail Mazurenka, Simon Neil, Stuart Mackenzie (University of Oxford) and Toni Laurila, Johan Hult, Clemens Kaminski, Justin Langridge, Rod Jones (University of Cambridge).

Parts of this thesis have been published or submitted for publication as detailed below:

Mathias Schnippering, Hayley V. Powell, Meiqin Zhang, Julie V. Macpherson, Patrick R. Unwin, Mikhail Mazurenka and Stuart R. Mackenzie, „Surface Assembly and Redox Dissolution of Silver Nanoparticles Monitored by Evanescent Wave Cavity Ring-Down Spectroscopy" *Journal of Physical Chemistry C* 2008, 112, 15274-15280.

Mathias Schnippering, Patrick R. Unwin, Johan Hult, Toni Laurila, Clemens F. Kaminski, Justin M. Langridge, Rod L. Jones, Mikhail Mazurenka and Stuart R. Mackenzie, "Evanescent Wave Broadband Cavity Enhanced Absorption Spectroscopy Using Supercontinuum Radiation: A New Probe of Electrochemical Processes" *Electrochemistry Communications* 2008, *10*, 1827-1830.

Mathias Schnippering, Hayley V. Powell, Stuart R. Mackenzie and Patrick R. Unwin, "Real-Time Monitoring of Polyaniline Nanoparticle Formation on Surfaces" *Journal of Physical Chemistry C* 2009, 113, 20221-20227.

Lineke van der Sneppen, Gus Hancock, Clemens Kaminski, Toni Laurila, Stuart R. Mackenzie, Simon R. T. Neil, Robert Peverall, Grant A. D. Ritchie, Mathias Schnippering and Patrick R. Unwin, "Following Interfacial Kinetics in Real Time Using Broadband Evanescent Wave Cavity-Enhanced Absorption Spectroscopy: A Comparison of Light-emitting Diodes and Supercontinuum Sources" *Analyst* 2010 (Advance Article).

Mathias Schnippering, Simon R. T. Neil, Stuart R. Mackenzie and Patrick R. Unwin, "Evanescent Wave Cavity Ring-Down Spectroscopy as a Probe of Interfacial Processes" submitted to *Chemical Society Reviews*.

Hayley V. Powell, Mathias Schnippering, Michelle Cheung, Julie V. Macpherson, Vasilios Stavros and Patrick R. Unwin, "Probing Redox

Reactions of Immobilized Cytochrome c using Evanescent Wave Cavity

Ring-Down Spectroscopy in a Thin Layer Electrochemical Cell"

ChemPhysChem, acctepted.

Abbreviations

Abbreviation	Description
AFM	Atomic force microscopy
ATR	Attenuated total internal reflection spectroscopy
BB-CEAS	Broadband cavity enhanced absorption spectroscopy
BBO	b-barium borate
CCD	Charge-coupled device
CEAS	Cavity enhanced absorption spectroscopy
CRDS	Cavity ring-down spectroscopy
CV	Cyclic voltammetry
CW	Continuous wave
DAQ	Data acquisition
DMP^+I^-	*trans*-4-[4-(dibutylamino)styril]-1-methylpyridinium iodide
DP	*trans*-4-[4-(dibutylamino)styril]-1-(3-sulfopropyl) pyridinium
DPI	Dual Polarisation Interferometry
ET	Electron transfer
EW-CRDS	Evanescent wave cavity ring-down spectroscopy
fcc	face-centred cubic
F-CRDS	Fibre optic cavity ring-down spectroscopy
$FeEDTA^{2-}$	Ethylenediaminetetraacetic acid iron(II) complex
ITO	Indium doped tin oxide
JMA	Johnson-Mehl-Avrami
LDCU	Laser diode control unit
LED	Light emitting diode
OPO	Optical parametric oscillator
PAni	Polyaniline
PCF	Photonic Crystal fibre
PFV	Protein Film Voltammetry
PGA	Poly-L-glutamic acid
PLL	Poly-L-lysine

PMT	Photomultiplier tube
PTFE	polytetrafluoroethylene
QCM	Quartz crystal microbalance
SAM	Self-assembled monolayer
SCR	Supercontinuum radiation
SECM	Scanning electrochemical microscopy
SERS	Surface-enhanced Raman scattering
SHG	Second harmonic generation
SPR	Surface Plasmon resonance
TEM	Transverse electromagnetic mode
THG	Third harmonic generation
TIR	Total internal reflection
TM-AFM	Tapping mode atomic force microscopy
UME	Ultra microelectrode
UV	Ultraviolet
VI	Virtual instrument

Glossary of Symbols

Symbol	Description
$(\alpha l)_{min}$	Minimal detectable extinction coefficient
α	Absorption coefficient
A	Absorbance
a	Radius
α	Electron transfer coefficient
β	Group velocity dispersion
c_L	Speed of light
c	Concentration
c^*	Bulk concentration
γ	Angle of incidence
γ_c	Critical angle
D	Diffusion coefficient
δ	Average secondary electron yield
d_p	Penetration depth
$\mathbf{E}$	Electric field
$\mathbf{e}$	Unit vector
E	Potential
ε	Extinction coefficient
f	Statistical frequency
F	Faraday constant
Φ''	Group velocity dispersion per cm
g	g-Parameter
G	Current amplification factor
Γ^*	Number of monomers
I	Intensity
I_0	Initial intensity

j	Current density
k	Rate constant
L	Length of the cavity
λ	Wavelength
M	Molecular weight
n_i	Refractive index of species i
ν	Scan rate
n	Number of electrons
N	Number of dynodes
N_a	Avogadro's constant
p	Longitudinal mode index
θ	Surface coverage
θ_B	Brewster angle
Θ	Fractional coverage
R	Reflectivity
ρ	Density
R	Gas constant
S	Area of electrode
$\sigma(t)$	Time-dependent surface area
τ	Ring-down time
t	Time
T	Temperature
t_{pulse}	Pulse duration
τ_0	Reference ring-down time
V	Volume

Abstract

This thesis is concerned with the application of evanescent wave cavity ring-down spectroscopy (EW-CRDS) and evanescent wave broadband cavity enhanced absorption spectroscopy (EW-BB-CEAS) for studies of electrochemical and interfacial processes. These include nanoparticle adsorption/dissolution, polymer nanoparticle formation and surface-bound electrochemical redox reactions. Different experimental setups have been designed to investigate these systems.

EW-CRDS is a surface sensitive technique, which allows absorption measurements at solid/liquid and solid/air interfaces. Surface reactions can easily be monitored in real time. A pulsed or modulated laser beam is coupled into an optical cavity which consists of at least one optical element, in which the beam is total internal reflected. At the position of total internal reflection (TIR), an evanescent field is established with the amplitude decaying exponentially with distance from the boundary. The evanescent field can be exploited to investigate the absorbance properties of the liquid phase in the first few hundred nanometres of the solution above the silica surface. These types of instruments have high temporal resolution (up to 2 kHz repetition rate), coupled with high sensitivity (minimum detectable interfacial absorbance per pass: ~80 ppm) which enables the investigation of a variety of processes relating to fundamental questions in the field of physical chemistry and materials science. The aforementioned sensitivity and resolution make EW-CRDS an ideal tool for those investigations, especially if combined with other techniques such as electrochemistry or microfluidic and hydrodynamic techniques. In this thesis, different instrumentational setups will be discussed.

EW-BB-CEAS is another example for a TIR based absorption spectroscopic technique and can give additional spectral information about the investigated surface processes by employing broadband light such as supercontinuum radiation. In this case, the amplified light intensity within the optical cavity is measured rather than the light decay.

By employing complementary techniques, such as electrochemistry and atomic force microscopy and by fitting experimental data using finite-element modelling, surface processes can not only be described accurately but also kinetic information such as rate constants for the aforementioned systems can be calculated.

1 Introduction

This thesis is concerned with studying the dynamics of various interfacial processes using evanescent wave cavity ring-down spectroscopy (EW-CRDS). This chapter provides a background for the different variants of cavity ring-down spectroscopy (CRDS) and the evolution of this technique from the gas phase into the condensed phase. This includes sections about different light sources, cavity configurations and their applications in the field of physical chemistry. Additionally, some basic considerations about atomic force microscopy (AFM) and electrochemistry are also described.

EW-CRDS is a surface sensitive technique, which allows absorption measurements at interfaces, with most applications hitherto at solid/liquid and solid/air interfaces. Surface reactions can easily be monitored in real time. A pulsed or modulated laser beam is coupled into an optical cavity which consists of at least one optical element, herein a silica prism, at which the beam undergoes total internal reflection (TIR). At the position of TIR, an evanescent field is established with the amplitude decaying exponentially with distance from the boundary. The evanescent field can be exploited to investigate the absorbance properties of the liquid phase in the first few hundred nanometres of the solution above the silica prism surface. These types of instruments have good spatial and temporal resolution, coupled with high spectral sensitivity which enables the investigation of a

variety of processes relating to fundamental questions in the field of physical chemistry and materials science. The aforementioned sensitivity and resolution make EW-CRDS an ideal tool for those investigations, especially if combined with other techniques such as basic electrochemical measurements or microfluidic and hydrodynamic techniques, which are developed throughout this thesis. In this section, different configurations for EW-CRDS will be discussed, along with instrumentation aspects. Additionally, several examples of the use of EW-CRDS will be demonstrated to exemplify this technique in more detail.

1.1 Cavity Ring-down Spectroscopy

The following two sections discuss the basic principles of CRDS, using simple gas phase measurements for illustrative purposes. It is hence shown, how the CRDS technique can be extended in order to measure adsorption at surfaces or reaction kinetics in condensed phases, especially through the use of the EW-CRDS variant.

1.1.1 Gas Phase CRDS

Introduced in 1988 by O'Keefe and Deacon,[1] CRDS has been used in the gas phase as a powerful technique for trace analysis[2] and spectroscopic studies of molecules and clusters. Many of these developments are summarised in several reviews.[3-6] Even small temporal variations in the sample concentration can be monitored using fast femtosecond pulsed lasers.[7] The extended path length provided by the multiple roundtrips is

responsible for the exceptionally high sensitivity and CRDS is now established as a reliable spectroscopic technique with applications ranging from trace gas detection, absorption spectroscopy, dynamical studies in the gas phase and even atmospheric gas detection. Instead of optical cavities employing highly reflective mirrors, this technique can also be operated using optical fibres.[8]

In CRDS, the exponential decay of the amount of light within an optical cavity (due to the loss of energy resulting from transmission and absorption by the mirrors) is measured with and without an absorber present, after filling the cavity with light to a steady-value and switching off the light abruptly. The time-dependent function for the intensity of the light, $I(t)$, obeys the Beer-Lambert law and depends on the reflectivity of the mirrors and the length of the cavity. It can be shown that for a simple two-mirror cavity (Fabry-Perot cavity) as shown in Figure 1.1, it satisfies

$$I(t) = I_0 e^{-\frac{c_L t}{L}(-\ln R + \alpha L)},$$ (1.1)

where I_0 is the initial intensity of the laser light within the cavity, c_L is the speed of light, L is the length of the cavity, R is the reflectivity of the mirrors and α is the absorption coefficient of the species of interest in the cavity. If we assume that R is close to 1, the measured ring-down time τ, which is conveniently defined as the time taken for the intensity to drop to I_0/e is:

$$\tau = \frac{L}{c_L(1-R) + \alpha L}$$ (1.2)

It is clear that with an absorbing species within the optical cavity, the characteristic ring-down time, τ, will decrease compared to an empty cavity, τ_0. The absorbance is described by

$$A = \log_{10}(e)\frac{\Delta\tau}{\tau\tau_0}\frac{L}{c_{\mathrm{L}}} \quad ,$$

(1.3)

Because of the increased light pathway due to multiple roundtrips, this technique is extremely sensitive to small concentrations.[2,4-5,9-10]
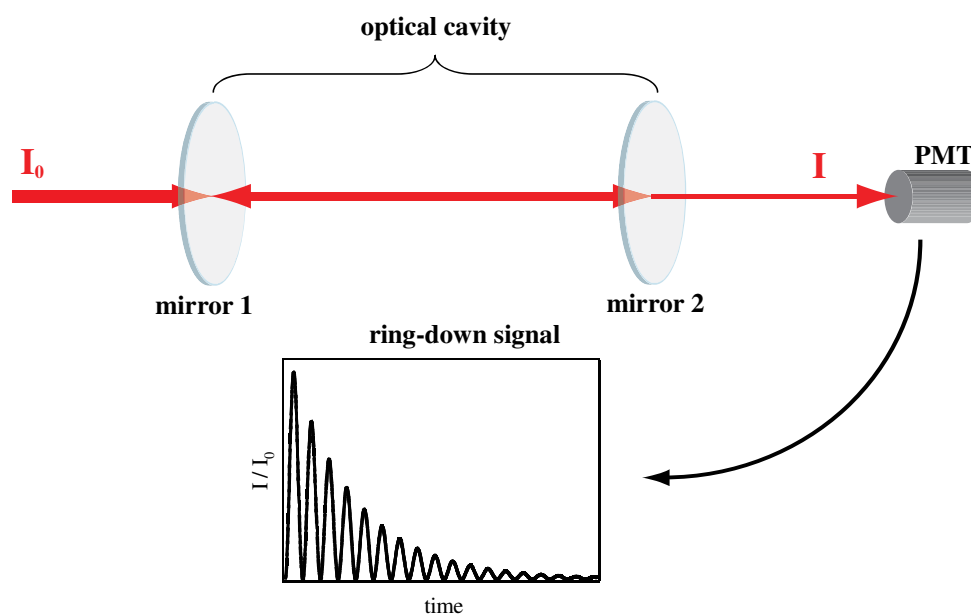
Figure 1.1: Schematic representation of a (linear) Fabry-Perot cavity. The light beam with intensity I_0 enters the cavity from the left through mirror 1. The light intensity, which decays exponentially with time due to the non-perfect reflectivity of the mirrors and absorption within the cavity, partly leaks out behind mirror 2 and is measured with a photomultiplier tube (PMT).

There are many varieties of linear cavities, the properties of which depend on the radii of curvature of the two mirrors (R_1 and R_2) and the length (L). There are three possible arrangements of optical cavities which depend on the curvature of the mirrors: plano-plano, plano-concave and concave-concave. A selection of different optical cavities is shown in table 1.1.

Table 1.1: The conditions and definitions for a range of different optical cavities.

Condition	Optical Cavity
$R_1 = R_2 = L$	confocal
$R_1 = R_2 = L/2$	concentric
$R_1 = R_2 \gg L$	long-radius
$R_1 = L \quad R_2 = \infty$	hemispherical
$R_1 = 2L \quad R_2 = \infty$	semi-confocal
$R_1 = R_2 = \infty$	Fabry-Perot

.

Optical cavities are said to be stable if a light beam is refocused within the cavity after successive reflections from the mirrors and is trapped within the cavity.[6] The criteria for cavity stability are expressed in terms of the so-called g-parameters:[6]

$$0 \leq g_1 g_2 \leq 1 \tag{1.4}$$

where

$$g_1 = \left(1 - \frac{L}{R_1}\right) \tag{1.5}$$

and

$$g_2 = \left(1 - \frac{L}{R_2}\right) \tag{1.6}$$

In unstable cavity systems, the light rays will steadily migrate across the mirrors until they finally escape the cavity. A Fabry-Perot resonator, where $g_1 = g_2 = 1$, is particularly challenging to align,[11] so most optical cavities have at least one concave element, which essentially refocuses the beam within the cavity.

There are a number of advantages of CRDS compared to other absorption spectroscopy techniques. The measurement of the absorbance depends only on the ring-down rate of light inside the optical cavity and

not on the intensity of the transmitted light. This also means that CRDS is insensitive to intensity fluctuation of the laser source. Also, optical resonators are stable and hence less sensitive to changes of the path length or temperature fluctuations.[6] An optical resonator can enhance the path length of the light up to several tens of kilometres (due to multiple reflections) compared to a single pass measurement.[6] By measuring and subtracting the ring-down time of an empty cavity from the sample measurement, absolute absorbance values can be obtained in a direct and simple way.[10]

The previously described model, which describes the decay of light in the ring-down cavity by taking into account the mirror reflectivity is unfortunately too simple. It does not include the fact that only light having frequencies near a cavity mode will be allowed inside the resonator. In any optical cavity, there is a set of allowed frequencies, so-called "modes" which are allowed to propagate and are determined by the geometry of the optical cavity. These are either longitudinal modes or transverse modes. Longitudinal modes determine the frequencies that satisfy the wavelength conditions of the cavity, which means that the electric vector of the light wave is zero at the mirror surface. The allowed frequencies for the longitudinal modes are governed by

$$ \upsilon_p = \frac{c}{2L}\left(p - \frac{\alpha_C}{2\pi} \right) \tag{1.7} $$

where υ_p is the frequency of the radiation, p is the an integer (the longitudinal mode index) and α_C is a corrective term to account for the

fact that the wave is not planar. The spacing between two adjacent longitudinal modes will be

$$\Delta \upsilon = \frac{c}{2L} \tag{1.8}$$

Transverse modes determine the cross-sectional profile of the beam. In this case the condition is that the transverse profile must be the same after one round-trip. The lowest order transverse electromagnetic mode, or fundamental mode (TEM_{00}), has a Gaussian cross-sectional profile.[6] There are an infinite number of transverse modes associated with one longitudinal mode.[6] In order to carry out CRDS experiments, the laser frequency usually has to be scanned in order to obtain a resonance frequency within the resonator. As we will see later, we can avoid this, by choosing a "broadband" light source, which will be able to excite many cavity modes at once.

There have been several approaches to measure surface properties using CRDS. Engeln *et al.* were able to measure one fundamental absorption band of C_{60} by inserting a C_{60}-modified optically transparent ZnSe substrate into a linear cavity.[12] The group of Pipino extended the CRDS technique from gas absorption studies to nanostructured surfaces by depositing Au nanoparticles onto silica. In this way, by using the surface Plasmon resonance (SPR) effect, it was possible to increase in the detection limit for trichloroethylene and dichloroethylene.[13] Their setup included an intracavity flow cell with two flat optical end-windows. These windows were aligned at Brewster angle. The Brewster angle for an air to glass transition is defined as:[14]

$$\theta_{\mathrm{B}} = \tan^{-1}\left(\frac{n_{\mathrm{silica}}}{n_{\mathrm{air}}}\right) \tag{1.9}$$

where n_{silica} and n_{air} are the refractive indices of silica and air, respectively.

For the experiment, one of the optical windows was coated with a thin nanostructured Au film. It was then shown that the SPR effect originating from the Au nanoparticles enhanced the sensitivity for the detection of trichloroethylene and dichloroethylene. This could be verified by comparing the experimental results obtained to an extended Mie calculation taking into account the formation of a dielectric coating on the nanoparticles. In a later paper, the same methodology was used to detect various nitro compounds.[15] It was found that the sensitivity of this approach compared to conventional SPR was approximately 35 times higher. The sensitivity of SPR of Au nanoparticles appeared to increase with the degree of nitration.[15]

1.1.2 Condensed Phase CRDS

There have been many attempts to transfer CRDS to the condensed phase and several approaches to measure thin films have been introduced. Xu *et al.* placed the sample cells directly into the cavity at the Brewster angle in order to reduce reflection losses. This setup enabled the measurement of absorption coefficients as low as 2×10^{-7} cm^{-1} and it was therefore possible to obtain vibrational electronic information of benzene.[16] A similar concept was used by Muir and Alexander to study the absorption features of films of oxazine and malachite green dyes coated on thin borosilicate microscope plates. When the sample was inserted at the Brewster angle, sub-monolayer

coatings in the range of 0.03 monolayers could be investigated.[17] This approach was adapted by Alexander in order to monitor reaction kinetics of nitrate radicals with terpenes in solution.[18] The same author has also demonstrated that CRDS can be used in systems involving liquid jets. With this approach, it was possible achieve a detection limit of $\alpha = 0.0162$ cm^{-1} using Malachite Green as an absorber which corresponds to a concentration of 71 nM.[19]

A further approach to implement CRDS into the condensed phase was presented by Hallock *et al*., by simply filling a standard linear optical cavity with the solution of interest.[20] It was found that the presence of the solvent did not interfere with high-reflective mirrors and did not alter their performance. It was shown that for measurements between 620 nm and 670 nm, a light absorbing compound such as Cu(II) acetate, which possesses a very high extinction coefficient in this range, could be detected at very low concentration. However, due to the long pathway in the linear optical cavity, and to minimise absorption and scattering of light in the solvent, it was necessary to limit the solutions to organic solvents such as hexane, acetonitrile and others which do not absorb in the red. Nevertheless, for strong absorbers, the detection limit was in the range of 1 – 10 pM, or equivalently a minimum detectable absorption coefficient of 1×10^{-6}. A similar approach was employed by the same group to study the reduction of Methylene Blue by ascorbic acid in acetonitrile.[21]

As recently discussed in a review[22] there are several other approaches for transferring CRDS into the condensed phase, but this chapter now

focuses on the EW variants of CRDS, which are directly relevant to the work carried out.

1.2 Evanescent Waves

A relatively new approach to implement CRDS in the condensed phase relies on the concept of evanescent waves. Evanescent waves are formed when a light beam undergoes total internal reflection at an interface consisting of two different media, as described by Snell's law

$$n_1 \sin \gamma_1 = n_1 \sin \gamma_2 \qquad (1.10)$$

where n_1 and n_2 are the refractive indices of the two different media, γ_1 is the angle of incidence of a beam striking the interface from medium 1 and γ_2 is the angle of the direction of propagation formed by the refracted beam with the normal to the surface as shown in Figure 1.2.
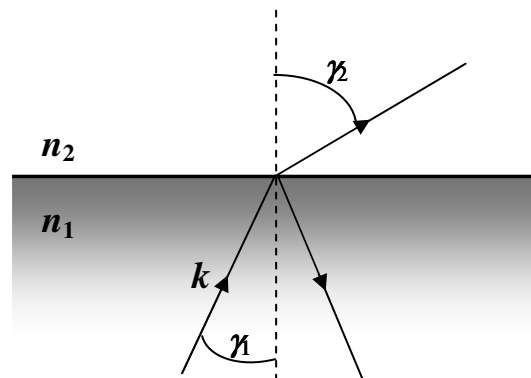
Figure 1.2: Schematic representation of an interface consisting of two media with different refractive indices. An incoming electromagnetic wave k is reflected and transmitted at the interface.

If the incidence angle exceeds the value of the critical angle

$$\gamma_c = \sin^{-1}\left(\frac{n_2}{n_1}\right) \qquad , \qquad (1.11)$$

the light is no longer transmitted into the second medium; rather it is totally

reflected as shown in Figure 1.3.
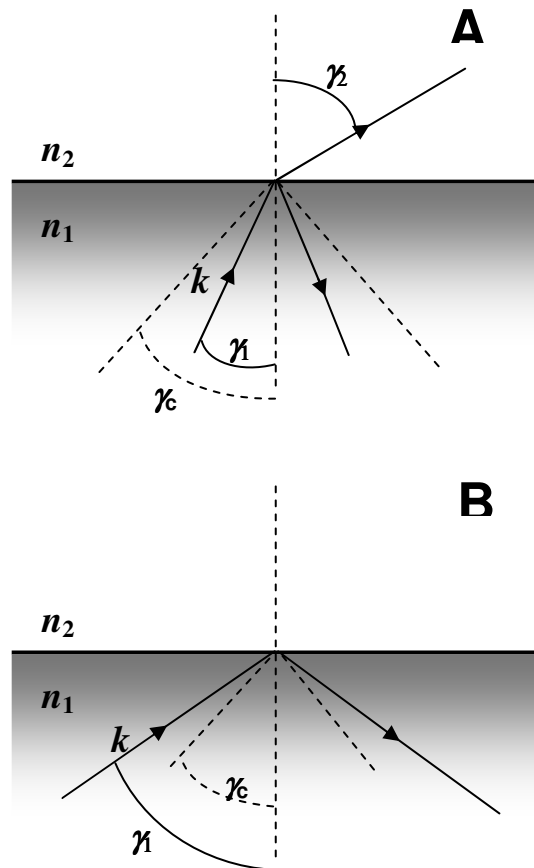
Figure 1.3: Schematic representation of an interface consisting of two media with different refractive indices. In both cases, $n_2 < n_1$. If the angle of incidence is smaller than the critical angle, the incoming electromagnetic wave k is reflected and transmitted at the interface (A). If the angle of incidence is larger than the critical angle, then the wave is totally internal reflected (B).

In the case of TIR (Figure 1.3B), there is still a certain amount of electromagnetic radiation present in the second medium. These waves are referred to as evanescent waves and can be described by taking into

account the boundary conditions on Maxwell's equations at the interface

for the incident and the total internal reflected beam.[23]

The incident plane wave can be represented in terms of two fields

with distinct directions. The p polarisation direction lies parallel to the

incidence plane and the s polarisation direction lies normal to the incidence

plane. The associated corresponding electric fields can be expressed as

$$\vec{E}_{p} = E_{x}\vec{e}_{x} + E_{z}\vec{e}_{z} \qquad \text{and} \qquad \vec{E}_{s} = E_{y}\vec{e}_{y} \qquad (1.12)$$

where $\vec{e}_{i}$ is the unit vector of the coordinate system ($i = (x, y, z)$), where x

and y lie on the interface between the two media and z is the direction from

the more refractive medium towards the less refractive medium and the

$y = 0$ plane is the plane of incidence. The boundary conditions of

Maxwell's equations still have to be fulfilled and are manifested in a non-

zero intensity of the electric field at the interface, since the there has to be a

matching field to the incident radiation on the other side of the interface. It

can be shown that the z-dependence of this evanescent field[23] can be

expressed as

$$\vec{E}_{p}(z) = E_{p}\frac{(2\cos\gamma)exp\left(-\frac{z}{d_{p}}\right)}{n^{2}\cos\gamma + i(\sin^{2}\gamma - n^{2})^{1/2}}\left[-i(\sin^{2}\gamma - n^{2})^{1/2}\vec{e_{x}} + \sin\gamma\vec{e_{z}}\right] (1.13)$$

for the p polarisation and

$$\vec{E}_{s}(z) = E_{s}\frac{(2\cos\gamma)exp\left(-\frac{z}{d_{p}}\right)}{n^{2}\cos\gamma + i(\sin^{2}\gamma - n^{2})^{1/2}}\vec{e_{y}} \qquad (1.14)$$

for the s polarisation, where d_{p} is the penetration depth (see below).

Significantly, it can be seen that the amplitude of the electric field

decreases exponentially with distance from the interface. Equation 1.15

describes d_p where the intensity of the evanescent field has dropped to 1/e of the field intensity at the boundary:

$$d_p = \frac{\lambda}{2\pi\sqrt{n_1^2 \sin^2 \gamma - n_2^2}}$$
(1.15)

where λ is the wavelength of the laser light (in vacuum). In theory, the penetration depth goes from infinity to $\lambda / 2\pi\sqrt{n_1^2 - n_2^2}$ as the incidence angle increases from γ_c to $\pi/2$. Depending on the wavelength of the source, the difference of the refractive indices of the two media and the angle of incidence, the penetration depth ranges usually from 50 nm to a few hundred nm.

1.3 Attenuated Total Internal Reflection Spectroscopy

Attenuated Total Internal Reflection Spectroscopy (ATR) and cavity based ring-down spectroscopic techniques based on evanescent waves rely on the formation of evanescent waves at silica or glass / air interface. ATR uses the evanescent waves of multiple TIR events at a silica / air or silica / solution interface to probe surface concentrations.[24] Figure 1.4 shows a schematic representation of a typical ATR setup. The light enters the ATR crystal on one side and undergoes multiple TIR events before escaping at the other end.
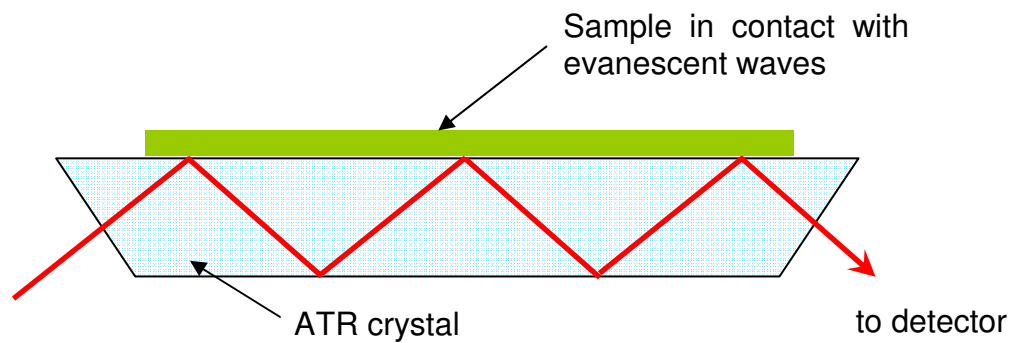
Figure 1.4: Schematic representation of a typical ATR setup. The incident light beam undergoes multiple TIR events. The attenuated beam escaping from the other end of the ATR crystal is measured with a detector.

1.4 Other Surface Sensitive Characterisation Methods

Surface Plasmon Resonance SPR is, similar to ATR, a total internal reflection technique[25-26] and was described for the first time by Kretschmann[27] and Otto[28] SPR is based on the optical excitation of surface plasmons by a laser beam. This technique can be used to monitor changes in the refractive indices of the solid/liquid interface and is a well-known characterisation technique for chemical and biological sensors.[26,29-31] SPR occurs at the interface of two media with dielectric constants of opposite signs *i.e.* a thin metal film or monolayer of metal nanoparticles (mostly Ag or Au) and a dielectric. The charge density oscillations induced by a incident laser beam establish an electromagnetic wave (surface plasma wave) with its maximum at the interface and decaying exponentially in both media. Due to the high losses within the metal, the majority of the field is concentrated in the dielectric. The reflected SPR beam is highly sensitive to the refractive index of the dielectric medium because it

depends on the angle at which the maximum resonance for a given wavelength is achieved. This technique can also be adapted to real-time measurements of changes in the refractive index.[32] SPR determines the angle of incidence at which the reflected light intensity is minimal (absorption maximum). It is either possible to measure the reflectivity as a function of angle (static SPR) or select an angle just below the minimal reflectivity and measure the reflectivity as a function of time (dynamic SPR). The electromagnetic wave is directly related (usually linearly) to the adsorbed amount.

Quartz crystal microbalance is a technique which can measure small changes in mass on a quartz crystal resonator due to the change of frequency during the deposition of thin films. The quartz crystal lies between two metal electrodes which establish a vibrational motion of the crystal at its resonance frequency by applying an alternating electric field. It can measure mass densities as low as a few micrograms per cm^2 and is used for analytical measurements in vacuum, gas phase and liquid phase as well.[33] QCM is therefore a very sensitive analytical method which can measure changes in the sub-monolayer range including molecular adsorption and interaction time resolved, however, it does not discriminate between different deposits since it only monitors the change in mass.

Although mostly used as an imaging tool for 3D topographic imaging, interferometry can also be used to study adsorption on surfaces with high sensitivity. Especially dual polarisation interferometry, DPI, (established by Farfield Sensors Ltd - Swann et *al.*[34]) has proven to be an excellent technique to study structural changes of molecules on surfaces

especially changes in protein structure,[35] protein interactions[36-37] and DNA hybridisation.[38] A polarised laser beam is coupled into stack of two optical waveguides which leads to two light waves in both waveguides which are in phase. Similar to SPR and ATR, DPI uses evanescent fields as sensing elements. The established evanescent wave from the top waveguide interacts with the adsorbed molecules at the surface and introduces a phase shift which with respect to the lower waveguide. In the far-field limit, both light waves will be combined with each other and the resulting interference fringes are measured.[34] The lowest detectable surface coverage for this technique is 20 %.[39]

Ellipsometry is a widely used tool in electrochemistry and surface science to measure thin film thicknesses.[40-41] The principle of ellipsometry is based on a polarised light beam reflected off the sample at various wavelengths and monitor the change in polarisation. In this way the complex optical ratio of the Fresnel reflection coefficients can be determined and, using various modelling tools, the optical parameters of the sample can be obtained. Tiberg *et al.* characterised surfactant self-assembled films using this technique.[42-43] It is also possible to obtain kinetic information using this technique as described by the same group.[44] Although a very sensitive method (< 1 % surface coverage), this method requires a somewhat advanced method for data analysis usually in form of a modelling procedure. Also, the sample should contain well-defined layers that are optically homogenous.

Optical reflectometry[45] can also be used to study the kinetics of reaction dynamics on solid surfaces. A linearly polarised laser beam is

reflected from the sample surface und the intensities of the *s* and *p* components are measured continuously. The amount of adsorbant on the surface can be obtained (after calibration) by monitoring the change of the ratio of these intensities.[46] Compared to ellipsometry, this technique is much simpler and cheaper, although it does not give information about the concentration profile of the adsorbed layer. Both, ellipsometry and reflectometry possess high sensitivity towards changes in the refractive index but need special calibration procedures.[47]

1.5 Evanescent Wave Cavity Ring-down Spectroscopy

The combination of the concept of evanescent waves described in section 1.2 and 1.3 with CRDS is straightforward and enables interfacial absorption measurements at a very high sensitivity. The first description of the concept of EW-CRDS was reported by Pipino *et al*.[48] The spectrometer consisted of a monolithic, TIR ring cavity with a hexagonal geometry as shown in Figure 1.5. A laser beam underwent TIR in a rectangular prism, generating an evanescent wave at the point of reflection. The intensity of the evanescent wave was used to excite the cavity modes in the hexagonal ring cavity. At another side, the decreasing in the light intensity was measured by photon tunnelling via another rectangular prism.
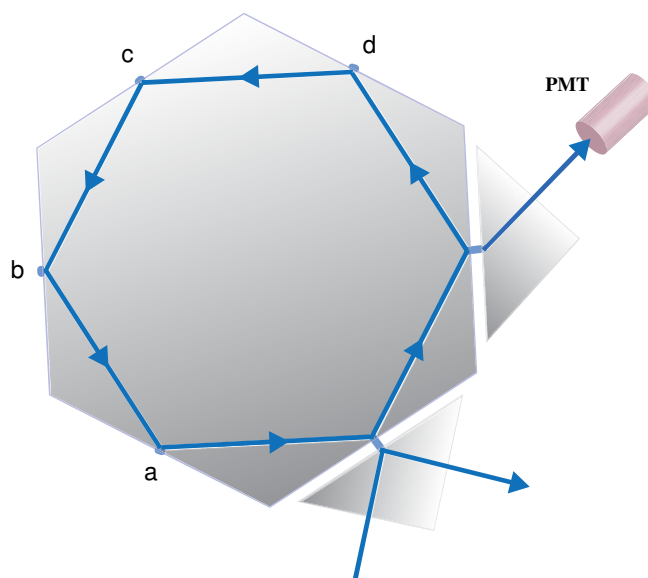
Figure 1.5: The hexagonal monolithic cavity as used by Pipino *et al.*.[48] The incoming light beam is totally reflected by prism A. The evanescent wave then excites the modes of the optical cavity by photon tunneling. At the surfaces (a) – (d) evanescent waves are established which can be used to obtain absorption spectra. The decrease of the light intensity is measured by coupling the light out of the resonator using prism C.

Shaw *et al*. examined the adsorption properties of Crystal Violet at the silica-water interface, incorporating a Dove prism in the optical cavity. With this setup, it was possible to investigate the adsorption of Crystal Violet as a function of the pH and the ionic strength.[49] The same group also investigated the pH-dependence of the absorbance of a Nile Blue derivative at the silica-water interface. The titration of the silica-water interface (*i.e.* the titration of two types of Si-OH groups[50]) was significantly different depending on whether the titration was carried out with increasing or decreasing pH. The absorbance decreased at lower bulk pH, suggesting an increase in the interfacial pH due to a stable charged layer at the surface.[51] A cooperative binding model was developed subsequently to interpret the

adsorption isotherm for a charged chromophore. It has been shown that the isotherm is pH sensitive and dependent on the degree of surface charge.[52]

Various studies have been carried out using a ring cavity with triangular fused-silica prisms. With this type of setup, Zare *et al.* investigated films of Methylene Blue at the air-silica interface[53] and carried out studies involving polymer/solvent interactions.[54] In the latter paper, different relative diffusion rates for methanol and water into a poly(dimethylsiloxane) film were measured. It has been shown by Zare *et al.* that the silica surface consists of two different types of silanol groups[55] which manifests itself in a two-site Langmuir isotherm of Crystal Violet adsorption. To obtain information about different electrostatic interactions, the surface can be functionalised by multilayer assemblies of polyelectrolytes, such as poly-L-lysine (PLL) and poly-L-glutamic acid (PGA). The resulting surface charge is either positive in the case of PLL or negative in the case of a PLL/PGA bilayer (over a wide range of pH). Originally developed by Decher *et al.*,[56-58] the electrostatic assembly of polyelectrolytes provides surfaces with well defined properties such as thickness and surface potential.[59-61]

1.6 Light Sources in EW-CRDS

The next few sections are describe the different cavity arrangements used in the aforementioned examples in more detail.

1.6.1 Diode Lasers

Diode lasers used for EW-CRDS are usually either "narrow band" or "broadband" lasers. The active materials of diode lasers are based on p and n doped semiconductors. By a applying a voltage between the anode and cathode of the photodiode, population inversion is achieved. If a laser with a very narrow bandwidth is used, it is usually necessary to scan the frequency of the laser in order to match the cavity modes of the CRDS set up. This is essential to achieve the resonance condition in the cavity. If, however, a "broadband" laser source with a relatively large bandwidth (~ 1 nm) is used, it is not necessary to scan the cavity, because many different modes of the cavity will be excited, due to the large frequency distribution of the laser. This is a feature of diode lasers.[62] This type of laser is usually not pulsed (*i.e.* it runs in continuous wave mode), but can be modulated, though in a time-scale where the laser is switched on for a duration that is much longer than the time taken for a light pulse to undergo several roundtrips in the cavity. In this case, the cavity is filled with light for a certain amount of time (depending on the modulation frequency). Then the laser is switched off and the decay of the light intensity within the cavity is recorded.[63]

1.6.2 Pulsed dye lasers and optical parametric oscillators (OPOs)

These types of lasers are usually pulsed which enables one to resolve the structure of the ring-down decay, since individual wave packages are

injected into the cavity.[64] With this "bounce-to-bounce" type technique, individual signals of the wave packages after each roundtrip are recorded as shown in the decay curve in Figure 1.1. Due to the high intensity of these lasers, the signal to noise ratio is usually very high and unmatched by other types of light sources. However, it is not possible to run these pulsed laser sources at a high repetition rate (usually only around 10 Hz), which makes fast kinetic measurements impossible. On the other hand, the tunability of the light sources provides the possibility of spectral information and one is not limited to measurements at a single wavelength.

In summary, the light source defines the type of experiment. Diode lasers are cheap, can be run in CW mode and enable fast kinetic measurements but are more lacking in terms of signal to noise ratio and can only give information at a single wavelength. Narrow band, pulsed sources are more expensive but are much higher in sensitivity and it is possible to obtain spectral information. But measurements are limited to the steady-state.

1.7 Cavity Configurations in EW-CRDS

There are many ways of building optical cavities. The most common cavities consist of two highly-reflective mirrors and an optical element, in which the laser beam undergoes total internal reflection. At least one of the elements needs to have a concave face to ensure the optical stability of the cavity (as discussed earlier in section 1.1.1). The evanescent field formed at the point of TIR can be used to monitor the absorbance at the silica/air or

silica/solvent interface.[65] However, there are also other examples such as monolithic optical cavities.[66-67] The following sections describe the most important optical cavities used in EW-CRDS.

1.7.1 Ring Cavity

One approach to extend CRDS into the liquid phase is the introduction of an additional optical element such as a prism. A pulsed laser beam is coupled into an optical cavity which consists of two high reflectivity mirrors and a fused silica prism as shown in Figure 1.6. An evanescent field is established at the position of the TIR. If a cell is fixed on top of the prism, it possible to investigate absorbance properties of the liquid phase in the first few hundred nanometres (within the penetration depth of the evanescent field) of solution above the silica surface.
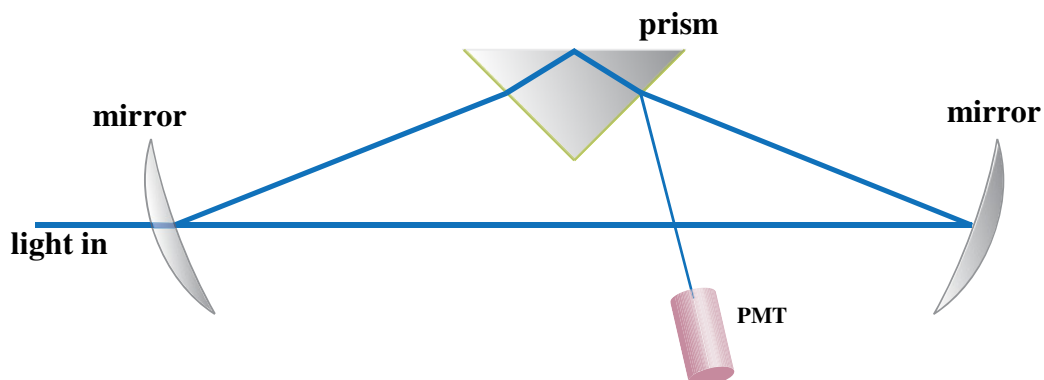
Figure 1.6: Schematic representation of a ring cavity setup.

The exponential decay of the amount of light within the cavity (due to the loss of energy resulting from transmission and absorption by the mirrors, the prism and the species of interest), after extinguishing the light entering the cavity, is measured by a photomultiplier tube (PMT). Figure 1.7 shows

a typical ring-down trace for a ring cavity. The employed laser runs in continuous wave (CW) mode (modulated at *ca.* 2 kHz) and has a bandwidth of 1 nm. Usually, several of these ring-down traces will be averaged to decrease the noise level.
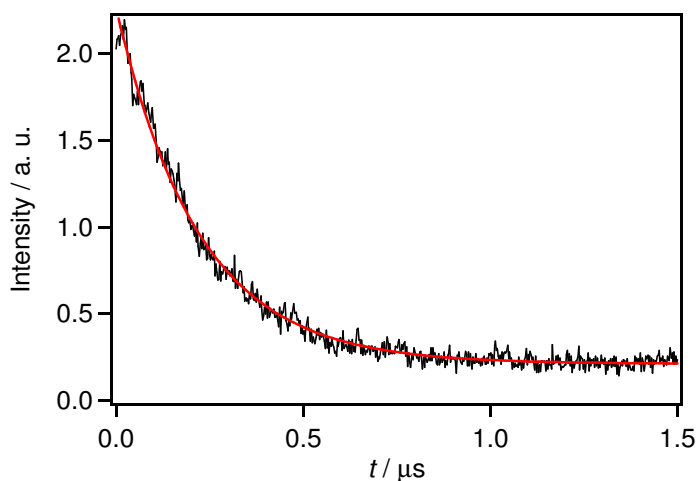
Figure 1.7: Typical ring-down trace for a ring cavity.

If the surface of the prism is modified (e.g. nanostructures, polymers or surface concentrations of molecules) the characteristic ring-down time will decrease due to the absorbance and scattering of these species within the evanescent field. The Absorbance is calculated using equation 1.3. The minimum detectable interfacial absorbance per pass is ~80 ppm[63] and the detection limit is usually limited by the prism itself. Since a large part of the beam is reflected at the prism, the measured signal is rather large and easy to measure. Prisms for the ring cavity can usually be purchased relatively cheaply from several manufacturers (*e.g.* CVI, UK). However, ring-down times are usually quite short compared to other cavity arrangements and the sensitivity is therefore limited, by comparison. Also,

it is not possible to conduct polarisation dependent measurements since the angle of incident where the beam enters the prism is not perpendicular.

1.7.2 Folded Cavity

The optical cavity in this configuration consists of two highly-reflective mirrors and a trapeze-shaped or 60 degree prism. The entrance and exit of the beam is normal to the prism surfaces, therefore there is no need for antireflective coating and the short prism faces. As shown in Figure 1.8, this setup essentially forms three sub-cavities, two between the mirrors and the prism faces and one within the prism itself. Ring-down times in this configuration should, in principle, be higher than in the ring cavity because reflections at the mirrors and at the prism faces are directed back into the laser beam path. The light leaking out of the cavity can therefore only be measured behind one of the mirrors. It should be pointed out that the lack of the antireflective coating also enables polarisation dependent measurements. It was also demonstrated, that this configuration can be used for broadband measurements using supercontinuum radiation because the angle of incident of the light is normal to the prism faces.[68]
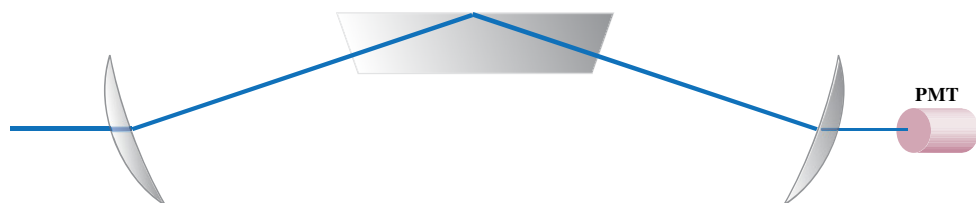
Figure 1.8: Schematic representation of a folded cavity. The beam enters the prism perpendicularly and therefore no antireflective coating is needed. The alignment procedure

is slightly more challenging and the prisms are not commercially available. The major advantage of this configuration is the possibility to carry out polarisation-dependent measurements.

1.7.3 Linear (Dove) Cavity

Another possible optical cavity to conduct EW-CRDS experiments was introduced by Shaw and consisted of a Dove prism in a linear cavity arrangement as shown in Figure 1.9.[49] The sides of the prism are coated with an anti-reflective material which also limits the detection limit somewhat (in the same way as for the ring cavity).

PMT
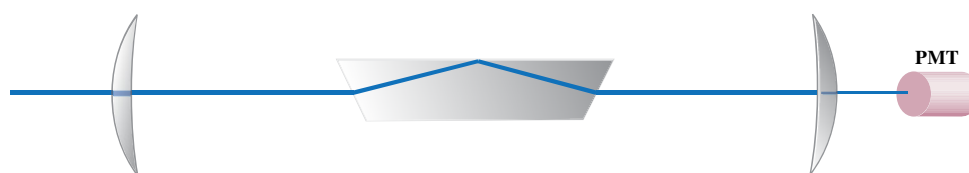
Figure 1.9: Schematic representation of a linear cavity employing a Dove prism.

1.7.4 Pellin-Broca cavity

Introduced by Pipino et al.[65] this cavity arrangement offers the possibility of polarisation dependent experiments. In this type of cavity, two concave mirrors and a silica prism are aligned as shown in Figure 1.10.
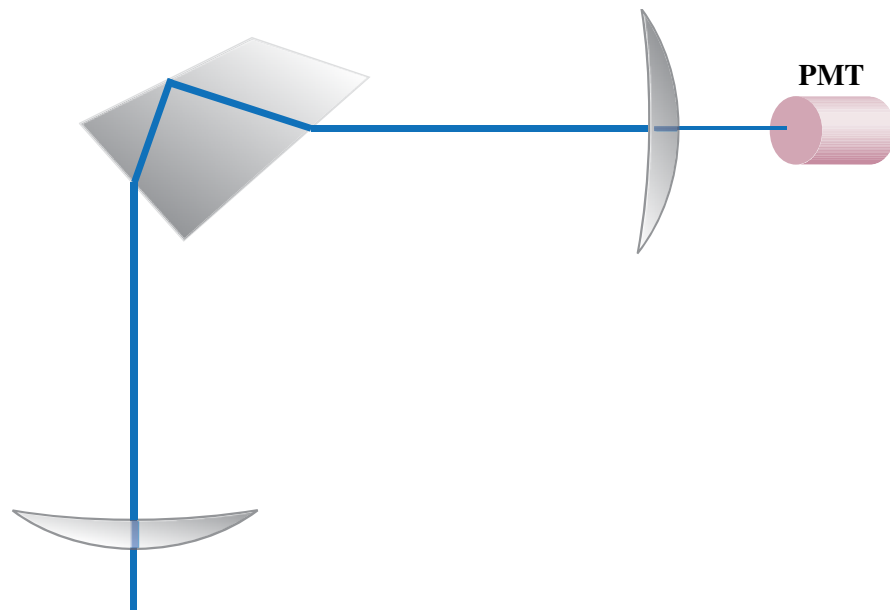
Figure 1.10: Schematic representation of a Pellin-Broca cavity as used by Pipino *et al.*[65] The beam enters and leaves the prism at Brewster angle.

Remarkably long ring-down times, up to microseconds which is much larger than the other cavity configurations discussed so far, can be achieved using this cavity arrangement. This configuration was used to investigate the adsorption, and molecular orientation, of I_2 on silica from the gas phase.[65]

1.7.5 Monolithic Resonators

Monolithic cavities can have different geometries as demonstrated by Pipino *et al.,*[48,66,69-70] but the most common cavities are polygonal resonators.[48,69] All monolithic cavities have in common that the light pulses are reflected within the silica material. There are no losses related to optical elements within the cavity because the light path is always in the same medium and this leads to significantly higher ring-down times.

Polygonal cavities were the first optical cavities to be used in EW-CRDS. An early paper by Pipino *et al.* describes polygonal optical resonator with one convex side where the laser pulse enters the cavity by photon tunnelling using a rectangular prism, as shown in Figure 1.11A.[69] The light undergoes multiple TIR events on all four facets within the monolithic cavity. Another coupling prism is employed to measure the light intensity in the resonator. On the two remain facets, the evanescent waves can be used to probe interfacial absorbances. However, to excite the cavity modes, photon tunnelling is used, which requires precise positioning of the coupling prisms.[66]

In the case of a folded cavity arrangement, the light enters and leaves the monolithic cavity perpendicular to the planar sides of the prism and the evanescent wave is formed at the larger convex face. A schematic is depicted in Figure 1.11B. Note, that this cavity is a further example of a folded cavity, which allows polarisation dependent experiments to measure molecular orientation of adsorbed material. Pipino *et al.*,[67,70-71] who were using these types of cavities for gas adsorption experiments (see below), achieved the highest sensitivity compared to different cavity configurations used by other research groups.
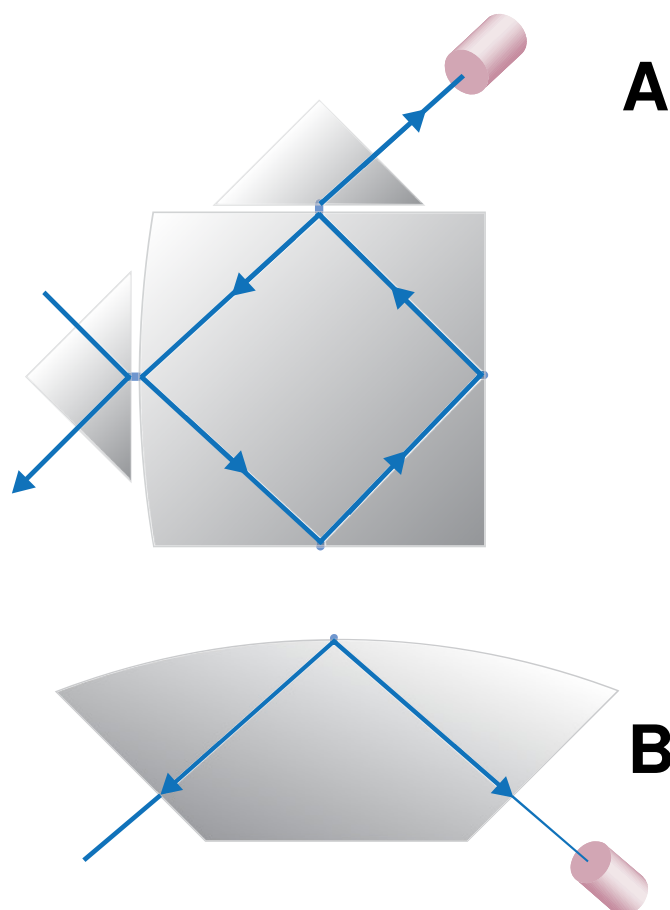
Figure 1.11: A) Schematic representation of a polygonal monolithic resonator. B) An experimental setup using a folded cavity configuration within a monolithic resonator.

1.7.6 Fibre Loops

Fibre optics are widely used for sensing applications and can also be implemented into the CRDS technique. It is possible to use fibre optic CRDS (F-CRDS) not only for pressure sensing[72-73] but also for molecular detection as shown by Brown and Kozin where the end of an optical fibre was fused to a splice connector.[8] If the matching fluid in the splice connector was replaced with a sample solution, it was possible to measure absorbance values. It was found that the ring-down time depended on the length of the fibre loop, however, if the loop is too short (*i.e.* < 3 m),

individual passes cannot be separated in time. Optical absorption spectra for different dyes were measured using this configuration. As an example, the detection limit for 1,18-diethyl-4,48-dicarbocyanine iodide was 2×10^{-15} mol. A more rigorous discussion can be found in a subsequent paper by the same authors.[74] By drilling a channel through the optical fibre, F-CRDS can be used as an on-line detector for electrophoresis.[75] The first report on an evanescent wave based optical sensor using fibre loops was presented in 2002 by von Lerber and Sigrist.[76] Part of the optical fibre was edged with buffered hydrofluoric acid in order to generate an evanescent field in this region. It was calculated that the sensitivity was 77 ppm for these induced losses. The measurements, however, are slightly complicated by that fact that one has to compensate for losses induced by bending the optical fibre. Optical fibre sensing can also be coupled with continuous wave CRDS.[77] In this case, a biconic taper is formed in a section of the optical fibre (spliced between the input and output coupler) which serves as a low loss sensing element. The same group also showed, that it is possible to adsorb microorganisms (here cells with an average size of 10 μm) and detect them due to induced scattering in the evanescent wave on a polypeptide coated on the biconical taper.[78]

1.8 Broadband Cavity Enhanced Absorption Spectroscopy

EW-CRDS is limited to the use of a single wavelength, since the decay time of light within the cavity also depends on the wavelength of the

radiation and it is very difficult to pulse broadband radiation, such as light from light emitting diodes (LEDs) or supercontinuum sources. However, there is considerable interest in obtaining time-resolved spectral information. Chapter 7 will deal with a new concept in order to measure an interfacial absorbance spectrum at a surface using cavity enhanced absorption spectroscopy (CEAS). In this, the radiation is not pulsed or modulated but irradiated continuously into the optical cavity. The amplified light in the cavity is measured with and without an absorber present on the silica surface.

1.9 Applications of EW-CRDS

The high spectral sensitivity of EW-CRDS, the good temporal resolution and, most importantly, the surface-confined sensitivity make EW-CRDS an excellent tool to study reaction kinetics on surfaces. However, there are limitations on which surfaces can be studied. The most obvious condition is the difference in the refractive indices of the two media, since the light beam has to be total internally reflected at the interface. Also, the medium in which the laser pulse travels should be relatively transparent to prevent losses due to scattering. The most studied interfaces are consequently silica/air and silica/liquid. However, it is possible to modify the silica surface, for example, with polymers in order to widen the range of possible substrates. We shall see later that it is also possible to generate stable optical cavities with a water/air interface.

1.9.1 Gas/Solid Interface

Pipino *et al*. were the first to probe surface processes with EW-CRDS. TIR inside a fused-silica Pellin-Broca prism, placed inside the optical cavity, generated the evanescent field. Unlike previous attempts using a polygonal ring cavity,[48] this cavity consisted of two high-reflective mirrors and the Pellin-Broca prism, leading to two intra-cavity TIR event per round trip. At constant temperature the equilibrium of solid I_2 on the surface and I_2 vapour was investigated by monitoring the absorbance of I_2 at 625 nm and 660 nm at the surface. Several cycles of adsorption and desorption of I_2 onto silica could be observed. Also, the I_2 adsorption seemed to follow a Langmuir-type isotherm and sub-monolayer sensitivity was readily achieved.[65]

Another concept of the monolithic resonator was reported by Pipino in 1999.[69] In this application, the optical resonator was square shaped, but the concept of both the in and out coupling of the laser beam via photon tunnelling using rectangular prism was as described above. As reported for the folded cavity arrangement with a Pellin-Broca prism, the adsorption of I_2 onto silica was studied. In this cavity, both *p* and *s* polarisations have a high finesse, which allowed polarisation-dependent studies of I_2 adsorption and the molecular orientation of I_2 molecules on the silica surface. It was observed that the *s*-polarised mode led to a significantly larger change in the ring-down time compared to the *p*-polarised mode, suggesting that I_2 molecules were preferentially oriented parallel to the surface.

To develop these studies, the same group used a folded cavity arrangement, with a monolithic cavity comprising a monolithic solid on which the planar sides were coated with an ultrahigh-reflective dielectric coating. The TIR took place at the concave face of the resonator. The use of dielectric coating enabled measurements over wavelengths ranging from 480 nm to 540 nm. In this setup, the intrinsic loss is essentially independent of polarisation. Measurements of the polarisation dependence of the absorbance confirmed that the molecules lay flat on the surface.

1.9.2 Solid/Liquid Interface

Although a surface sensitive technique, EW-CRDS can easily detect fairly low concentrations of dyes and light absorbing molecules in the bulk. This is evident in proof-of-principle experiments employing a thin-layer cell.[63] By introducing a Pt macroelectrode close to the evanescent wave, it is possible to change solution properties such as pH and redox species concentrations locally and monitor either surface concentrations and/or surface reactions spectroscopically. In this particular experiment,[63] ferricyanide, $[Fe(CN)_6]^{3-}$, was electrochemically generated from ferrocyanide $[Fe(CN)_6]^{4-}$. The oxidised species possesses a much higher absorbance at the chosen wavelength (417 nm) and the surface concentration of the electrogenerated species therefore could easily be measured within the evanescent field as shown in Figure 1.12A. After a short lag time due to the transport-limited reaction, the ferricyanide was detected in real time at the interface. Although the sensitivity towards the bulk is somewhat limited in EW-CRDS, this effect is still very important,

especially because this background signal will also contribute to any investigations of surface reactions and has to be accounted for when deducing real surface absorbance values, as described below. In this particular example, it was demonstrated that this spectroelectrochemical technique allowed electrochemical data to be obtained simultaneously with the spectroscopic data.

Figure 1.12B shows the ferricyanide concentration at the prism/electrolyte interface as a function of time together with the current signal of the oxidation and reduction at the macroelectrode. At the onset of the oxidation peak of this cyclic voltammogram and after a certain lag time due to diffusion from the electrode to the silica/aqueous interface, the absorbance – and hence the ferricyanide concentration – increases and reaches maximum value, which corresponds to the bulk concentration (when all ferrocyanide has been converted). The absorbance decreases again, when the applied potential is reversed.
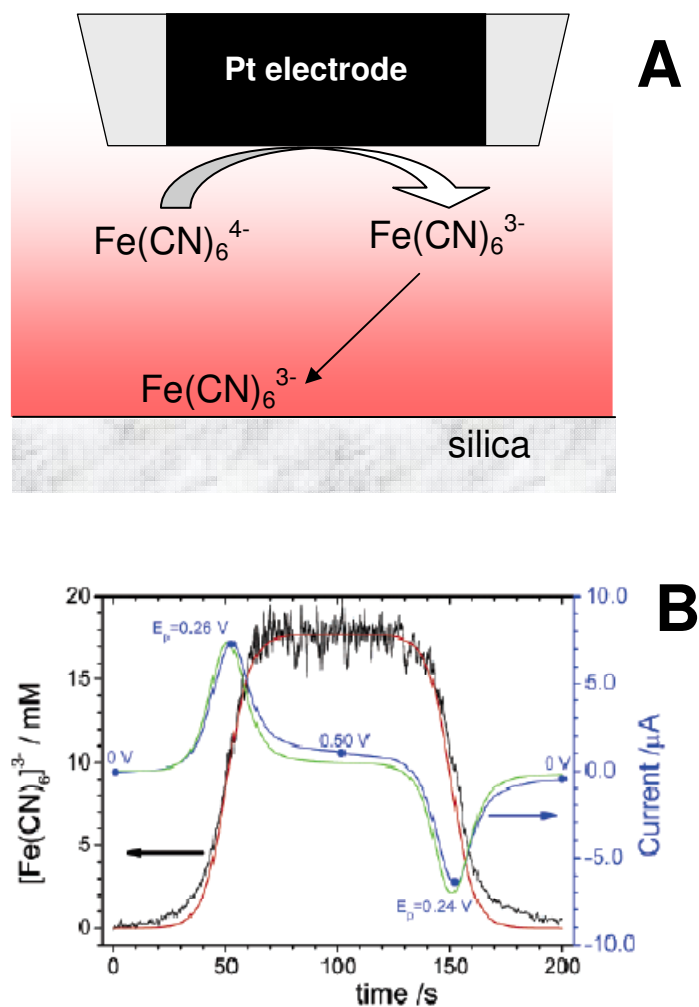
Figure 1.12: A) Schematic of the thin layer cell configuration. B) Ferricyanide concentration recorded in the region of the evanescent field as a function of time during a CV (5 mV s^{-1}) for an electrode-surface distance of 25 ± 1 µm. The corresponding red and green lines show simulations based on finite element modelling. (Taken from Ref[63])

Shaw *et al*. studied the interaction of the chromophore Crystal Violet onto a charged silica surface as a function of the solution pH.[49] The cavity employed in these experiments was also in a folded arrangement (two high-reflective mirrors and a Dove prism). The solutions were passed over the surface using a flow cell, which was a convenient way to replace the solution above the evanescent field. Since the evanescent field

34

penetrates somewhat into the bulk solution, the absorbance of the chromophore in bulk had to be measured. This was accomplished by passivating the silica surface in order to prevent direct adsorption onto the surface. The interfacial optical absorbance for all later measurements could then be obtained by subtracting the bulk absorbance value.

The concept of modifying the silica surface was followed up by Powell et al.[79] In this case the silica prism was modified with a PLL and PGA bilayer in order to obtain a negatively charged surface. After the adsorption of the redox mediator Ruthenium bipyridine ($Ru(bpy)_3^{2+}$), the pH around the region of the evanescent field could be changed using a macroelectrode close to the point of TIR as described above. By stepping the electrode potential to very positive values, H^+ ions were generated to protonate the PGA layer, leading to the release of $Ru(bpy)_3^{2+}$ from the PLL/PGA bilayer. Because the electrochemical generation of H^+ was so well defined, it was possible to follow the titration of the PGA film, by simply changing the potential step time or the electrode/prism separation and thus generate different pH values in the thin-layer cell.

There has also been some effort to describe the adsorption of biologically important molecules on surfaces. Everest et al. investigated the polarisation-dependent adsorption of Hemoglobin on silica employing a Dove prism.[80] Since the beam enters and exits at a right angle to the prism surfaces, it was possible to measure very slight changes in the molecular orientation. The dichroic ratio, which is defined as

$$\rho = \frac{A_{\text{TE}}}{A_{\text{TM}}} = \frac{\left|E_y\right|^2}{\left|E_x\right|^2 + 2\left|E_z\right|^2 \cot^2\langle\theta\rangle} \tag{1.16}$$

where A_{TE} and A_{TM} are the absorbance of transverse-electric and transverse-magnetic polarised light, respectively, $\langle\theta\rangle$ is the average angle of the transition dipole moment measured off the surface normal, and $\left|E_y\right|^2$ is the ith component of the electric field intensity in the evanescent wave could be used calculate the average tilt angle of the dipole moment. Using this equation it was found that the tilt angle changed from $54.81° \pm 0.06°$ to $57.913° \pm 0.002°$ over the course of the experiment. In the same paper, rate constants for adsorption, desorption and irreversible adsorption were calculated numerically using a diffusion/reaction model.

Fan *et al.* investigated the adsorption properties of neutral *trans*-4-[4-(dibutylamino)styril]-1-(3-sulfopropyl) pyridinium (DP) and charged *trans*-4-[4-(dibutylamino)styril]-1-methylpyridinium iodide (DMP$^+$I$^-$) at the silica/acetonitrile interface and successfully applied EW-CRDS in a different silica/solvent system.[81] By letting other neutral molecules such as triethylamine compete with the silanol binding sites, the nature of the binding of DP and DMP$^+$ was determined. It was found that the DP is bound to the SiOH groups via hydrogen bonds in contrast to DMP$^+$ which was adsorbed electrostatically. Because the adsorption followed a simple Langmuiran binding model, thermodynamic properties, such as free energy of adsorption were calculated readily.

EW-CRDS is also a very powerful tool to investigate adsorption and aggregation kinetics on surfaces. The group of Shaw measured the

binding kinetics of own-synthesised Au nanoparticles on the silica/water interface using continuous wave diode lasers at 635 nm and 830 nm.[82] Two batches of citrate stabilised nanoparticles were synthesised, leading to colloids with mean diameters of either 15 nm or 45 nm. These particles seemed to adsorb onto the silica surface despite being negatively charged and their extinction coefficients were obtained. The smaller particles were found to form multilayers on the surface. The binding kinetics of the gold particles at sub-monolayer coverages was found to depend on the surface coverage. Additionally, both types of nanoparticles packed into multilayers and the aggregation appeared to be size and ligand-dependent. In other experiments, the same group investigated the kinetics of the formation of a self-assembled monolayer (SAM) of thioctic acid (ToA) on the same type of gold nanoparticles. It was found that the kinetics were highly dependent on the pH from which the SAM was deposited. SAM deposition from acid conditions produced high-density neutral SAM (protonated COOH groups), whilst SAM deposited from basic conditions yielded in low-density charged SAMs (deprotonated COOH groups). The monolayer formation transients were fitted successfully to a kinetic model in which the sticking probability of the thioctic acid depended on the lateral interactions between the charged and neutral thiols. The nature of these interactions was electrostatic for the charged-deposited SAM because of the charged solvation shell and the ionic strength of the surrounding electrolyte, which resulted in a less dense SAM on the nanoparticle. It was also possible to change the interfacial refractive index on the Au nanoparticles simply by changing the bulk pH in solution. These changes

could be observed, because the main contribution to the Au nanoparticle extinction coefficient comes from the plasmon resonance, which is highly sensitive to changes in the refractive index.

In order to obtain more information about the binding properties of metal nanoparticles, our group investigated the adsorption of commercial available gold nanoparticles onto PLL modified silica.[83] The measurements were carried out in a folded cavity arrangement using a diode laser emitting light at 405 nm. The time-dependent adsorption kinetics of two different solutions of gold nanoparticles with average sizes of 5 nm and 20 nm were followed at different dilutions. It was found that none of the particles adsorbed onto the bare silica surface, but possessed a high affinity towards positively charged PLL-modified silica which can be explained by electrostatic interaction between the PLL and the negatively charged citrate shell of the gold nanoparticles. The adsorption kinetics of the 5 nm Au particles could be explained by a diffusion-limited irreversible adsorption model, as developed by Adamczyk.[84] When the negatively charged Au particles neutralise the charge density of PLL on the surface, any further adsorption is inhibited and the maximal coverage is reached.

The adsorption kinetics of the 20 nm Au particles were considerably different. After an initial adsorption behaviour similar to the 5 nm particles, the absorbance transients reached a plateau surface coverage after *ca.* 10 min. However, the absorbance subsequently increased linearly with time indicating structures comprising many hundreds of nanoparticles. TM-AFM confirms the formation of aggregates

at this stage. Figure 1.13 and Figure 1.14 show the absorbance transients for the 5 nm and 20 nm Au particles.
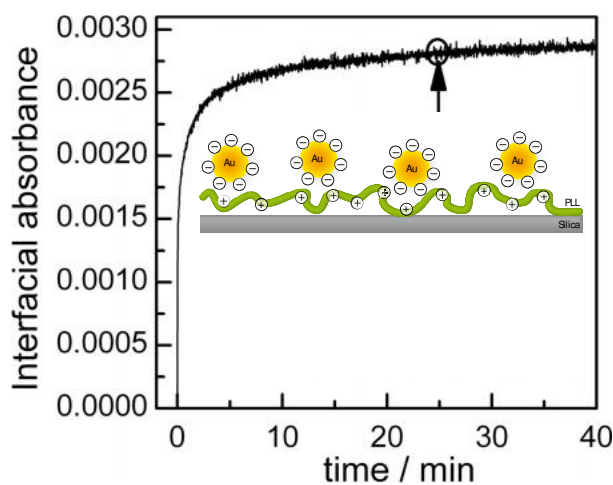
Figure 1.13: Absorbance transients for the adsorption of 5 nm Au nanoparticles onto a PLL-modified silica surface. After 10 min, the maximal coverage has been achieved. TM AFM (after 25 min) shows no evidence of particle aggregation (Taken from Ref.[83])
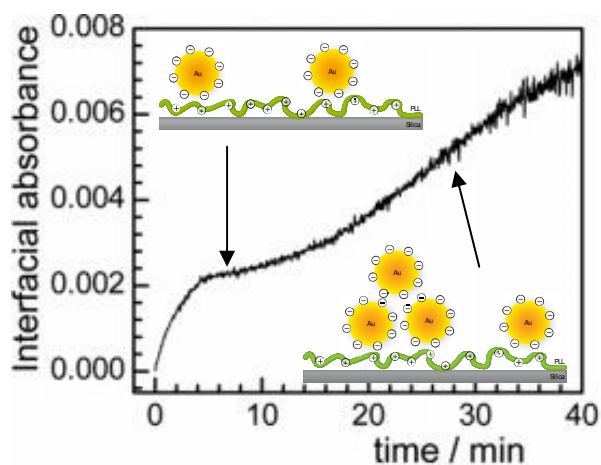
Figure 1.14: Absorbance transient for the adsorption of 20 nm Au nanoparticles onto a PLL-modified silica surface (Taken from Ref.[83]).

As shown in Figure 1.15, it was also possible to monitor the formation of multilayer structures of alternating layers of (positively charged) PLL and (negatively charged) Au nanoparticles.
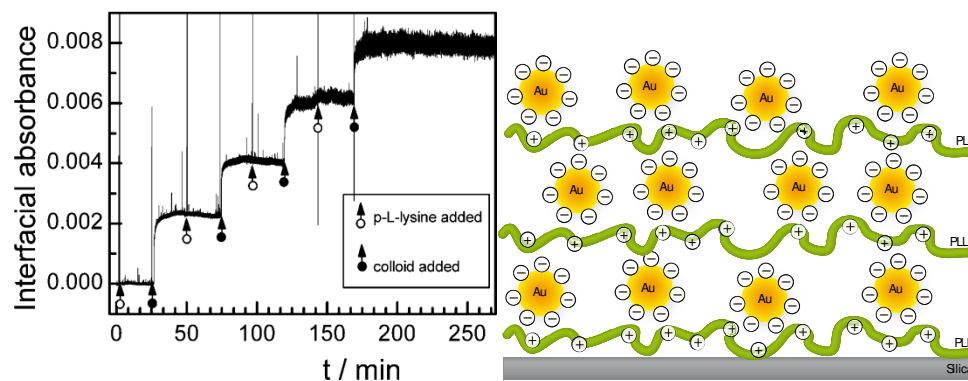
Figure 1.15: Interfacial absorbance as a function of time for several Au nanoparticle adsorption steps. The colloids and the PLL were added sequentially, as indicated, to form multilayer structures (Taken from Ref.[83]).

The study of thin films in an optical cavity setup was demonstrated by Richard Engeln *et al.* in 1999.[12] The cavity was formed between two plano-concave mirrors. Absorbance measurements of thin films were obtained by introducing an optically transparent ZnSe window within the linear cavity. It was demonstrated that the absorbance spectrum of a thin film of C_{60} (20 – 30 nm) deposited on the ZnSe window could be recorded. The mirrors were high reflective between 7.9 μm and 8.9 μm. The centre of the observed peak was at 8.46 μm and corresponds to one of the four F_{1u} IR fundamental absorptions of C_{60}.

The molecular orientation of a thin film of methylene blue at the air/fused-silica interface was investigated by Zare *et al.* in 2005.[53] Methylene blue possesses a dipole moment along its main molecular axis. The average orientation angle of a self-assembled monolayer of Methylene Blue (evaporated on the surface from methanol) can be described by an expression including the amplitude of the electric field of the evanescent wave and absorbance measured using *s* and *p* polarised light. Figure 1.16A

shows schematically the arrangement of a Methylene Blue molecule on the prism surface. Using a standard ring-cavity setup with a triangular prism, which enabled polarisation-dependent measurements, it was shown that – at low coverages – the molecules lie flat on the surface and that by increasing the surface concentration, the molecules become vertically oriented. For example, at a fractional surface coverage of 0.02, the average orientation angle with respect to the z axis (perpendicular to the surface), was 83°. At much higher surface coverages, the average orientation angle approached 70°. This trend is exemplified in Figure 1.16B.
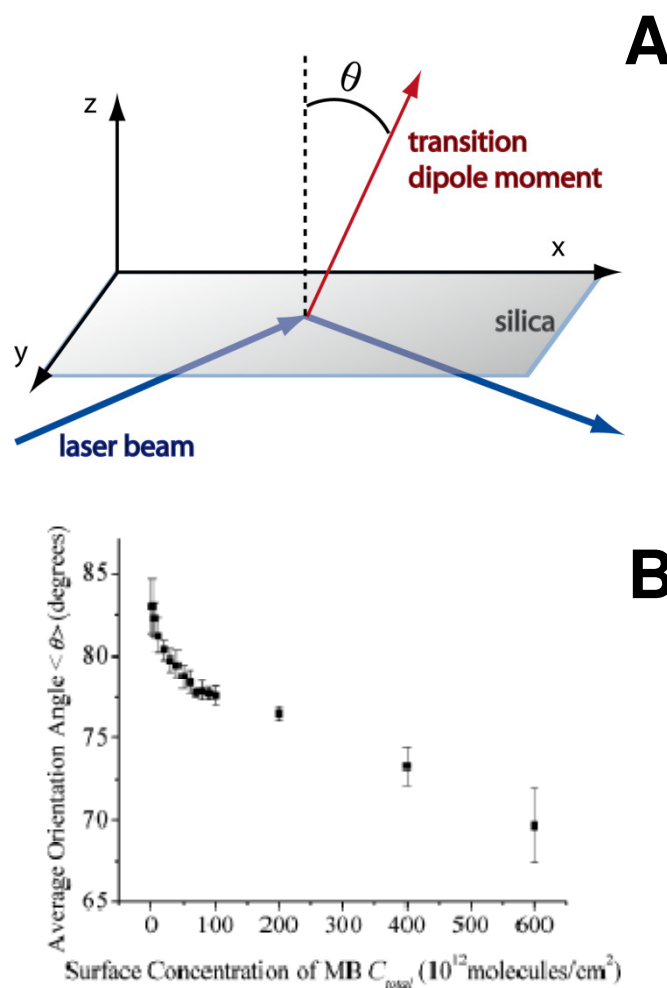
Figure 1.16: A) Molecular orientation of Methylene Blue at the prism surface. B) The average orientation angle as a function of Methylene Blue surface concentration. At low concentrations, all molecules lie flat on the surface (Taken from Ref.[53]).

The same group employed their version of EW-CRDS to another system to show the feasibility of EW-CRDS to monitor solvent ingress at the polymer/fused silica interface using water and methanol.[54] In these experiments, a pre-synthesised polymer film, poly(dimethylsiloxane) (PDMS) was attached to the prism surface. The thickness of this film was several hundreds of micrometers, exceeding by far the penetration depth of the evanescent field. It was found that the uptake of methanol was initially slower compared to water, but after an initial period of a few minutes, the methanol diffuses faster into the polymer film. The source of the EW-CRDS losses was found to be scattering effects throughout the PDMS film resulting from the uptake of the solvents. Complementary SPR studies strongly suggested that methanol caused the polymer to swell, forming pockets of bulk methanol in the region of the evanescent field. On the other hand, water seemed to form a thin film and did not cause as much scattering. In both cases, it was possible to calculate diffusion coefficients for the two solvents.[54]

1.9.3 Liquid/Air Interface

Initial studies by Neil and Mackenzie have shown the possibility of carrying out EW-CRDS experiments at the liquid/air interface. In this particular experiment, the light beam was aligned through the sub-phase of a Langmuir trough in a folded cavity arrangement, where one of the mirrors was incorporated into the trough and the other cavity mirror was manipulated externally as shown in Figure 1.17. After a small amount of a

dye was dropped onto the subphase, the barriers were closed and the EW-CRDS signal was monitored simultaneously.
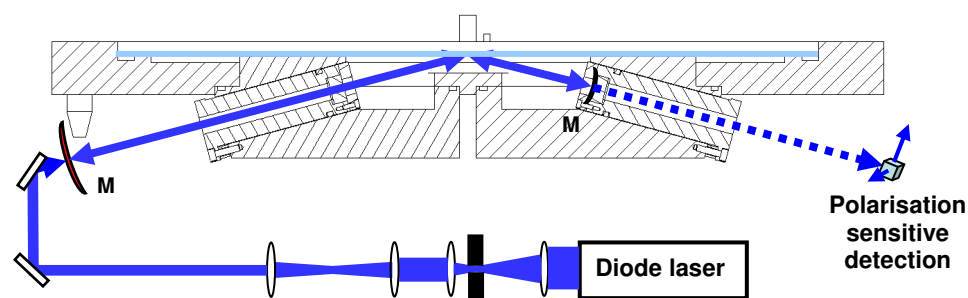
Figure 1.17: Schematic of an EW-CRDS setup to investigate liquid/air and liquid/liquid interfaces.

1.10 Atomic Force Microscopy

Atomic force microscopy[85-86] (AFM) provides an accurate description of surface topography, typically by monitoring the Van der Waals interaction between a sharp tip and a sample.[87] Other forces such as chemical bonding,[88] capillary,[89] electrostatic,[87,90] magnetic[91-92] and solvation[87-88] forces can be encountered by the tip. AFM is not limited to measurements in air but can also be implemented *in situ*,[87,93-94] which is especially important for investigating biologically relevant systems.[95-100] The tip is located at the free end of a cantilever that is 100 to 200 μm long. Forces between the tip and the sample surface cause the cantilever to bend or deflect. While scanning the tip over the sample, the cantilever deflection will be detected by a position sensitive photodetector. This is done by focusing a laser beam onto the mirror like back of the cantilever.

43

In the contact mode, the force between the tip and the sample is repulsive. In this configuration, the AFM tip makes soft "physical contact" with the sample. The repulsive force bends the cantilever, inducing a change in the position of the reflected laser. As shown in Figure 1.18, the force interactions are strongly dependent on the distance which allows a very high spatial resolution. After the tip approaches the surface (1) and jumps into contact (2), it senses an attractive force (3). If the tip is pushed further into the surface, the force between the tip and the substrate is repulsive (4). If the tip is pulled away (5), the force is attractive again (largely due to adhesion) until the tip looses contact with the surface (6).
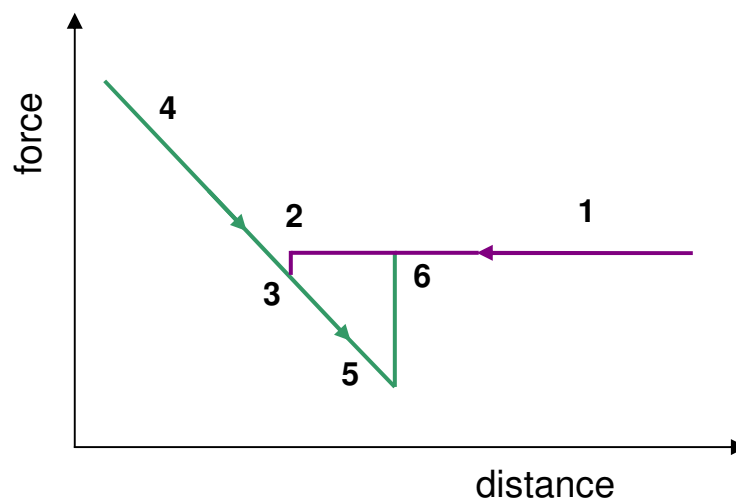
Figure 1.18: Schematic of an AFM approach curve.

In acoustic AFM[101-103] (tapping-mode AFM[TM]) the tip of a stiff cantilever vibrates near its resonant frequency and the amplitude is dampened when the tip encounters the surface.
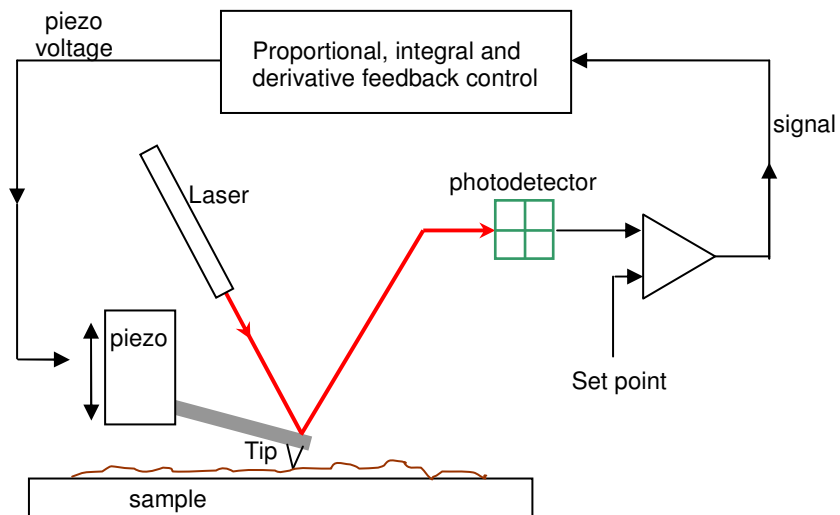
Figure 1.19: Schematic setup of the AFM experiments.

A schematic representation of the AFM setup is displayed in Figure 1.19. The oscillating tip is moved towards the surface until it begins to detect the repulsive force from the surface. Changes in the topography affect the amplitude of the oscillation which is corrected by the feedback system in order to keep the amplitude constant (set point) which is a more gentle way to obtain a topographic image in comparison to contact-mode AFM. The lateral resolution in acoustic AFM is lower than for contact AFM, but allows topographic imaging of features which are weakly adsorbed on their substrates.

The oscillation amplitude is reduced due to an energy loss caused by contact of the tip with the substrate. During the experiment, the cantilever vibration is maintained constant by the feedback loop. When the tip scans over a surface feature, the cantilever has less freedom to oscillate and the amplitude of the oscillation decreases which leads to a change of the deflection of the laser. The feedback loop adjusts via the expansion of

the piezo element to maintain a constant amplitude (restore the set point position).

An important issue is the sharpness of the tip. If the end of the tip is approximated by a spherical apex, the topographic features or the sizes similar or smaller than the apex curvature will be convoluted with the shape of the tip.[104] Spherical or hemispherical features will therefore appear laterally distorted but with an accurate height estimation.

1.11 Electrochemical Techniques

Potential step chronoamperometry and cyclic voltammetry (CV) are basic electrochemical methods, often involving a 3 electrode configuration with macroscopic working, counter and reference electrodes.[105] A potentiostat has control of the voltage across the working electrode-counter electrode pair, and it adjusts this voltage to maintain the potential difference between the working and reference electrode[105]. Additionally, it ensures that no current flows through the reference electrode. The potential of the working electrode is forced to adhere to a known programme with respect to the reference electrode. In the case of potential step chronoamperometry, the electrode potential, $E(t)$, is stepped at $t = 0$

$$E(t) = E_1 \text{ if } t < 0 \qquad\qquad (1.17a)$$

$$E(t) = E_2 \text{ if } t > 0 \qquad\qquad (1.19b)$$

where E_1 is the initial electrode potential and E_2 is the step potential. CV will be performed if the potential is swept linearly with time at a scan rate, v, and if the direction of the scan is switched at the time $t = \lambda$.

$$E(t) = E_{\text{start}} - vt \quad \text{if } 0 < t < \lambda \tag{1.18a}$$

$$E(t) = E_{\text{start}} - 2v\lambda + vt \quad \text{if } t > \lambda \tag{1.20b}$$

where E_{start} is the initial electrode potential at which the cycling is started. In both cases, current *vs.* time (voltage) curves will be recorded. For an electrochemically reversible system (diffusion-controlled) assuming semi-infinite linear diffusion, the peak current density, j_p, in a CV experiment at 25°C can be described with[105]

$$j_p = \left(2.69 \times 10^5\right) n^{3/2} D_O^{1/2} C_O^* v^{1/2} \tag{1.19}$$

where n is the amount of electrons involved in the redox process, D_o is the diffusion coefficient of the oxidised species in $\text{cm}^2\ \text{s}^{-1}$, C_O^* is the bulk concentration of the oxidised species in mol cm^{-3} and v is the scan rate in V s^{-1}. In this ideal situation, the peak potential is independent of the scan rate and j_p is proportional to $v^{1/2}$.

1.12 Nanostructured Surfaces

Nanostructured surfaces are of huge interest not only because of the possibility of increasing the surface to volume ratio, but also because of different size effects originating for example from different sized nanoparticles.[106-108]

The collective excitation of electrons in the metal by incident light, known as plasmon resonance, is an important property of metal nanoparticles.[109-111] Light of frequency below the plasmon frequency is reflected, because the electrons in the metal screen the electric field of the light. Light of frequency above the plasma frequency is transmitted,

because the electrons cannot respond fast enough to screen it. In 1857, Faraday discovered that colloidal gold clusters in aqueous phase transmit red light due to this effect.[112] Years later, this effect was then discussed by Mie using the interaction of the conduction band electrons with an electromagnetic field.[113] These metal nanoparticles possess unique shape and size dependent properties[108,114] compared to their corresponding bulk material and it is therefore of great interest to synthesise them in a well-defined manner.

The method introduced by Turkevich for the synthesis of gold particles is still used to synthesise colloidal citrate stabilised metal nanoparticles.[115] In most cases, electrostatic stabilisation is realised when a protective coating on the surface of the nanoparticles is formed. Strong quantum size effects are observed with particles in the size range of clusters (several atoms), since the energy levels have not formed energy bands yet. Because the physical properties of nanosized materials are dependent on the size, it is important to synthesise nanoparticles with very narrow size distribution. There are several ways to determine the size. In this work, acoustic AFM is used.

1.13 Aim of the thesis

This chapter has primarily given an overview about the different types of CRDS and EW-CRDS techniques, with a principal focus on adsorption experiments, both in the gas phase and the condensed phase. The aims of this project were to investigate quantitatively the formation of several

nanostructured surfaces using EW-CRDS and also to probe the solid/liquid interface locally (and dynamically) by employing electrochemical and flow techniques in a thin layer cell arrangement. The objectives can be roughly summarised in 4 points:

(a) The development of a novel instrument coupling EW-CRDS with a variety of electrochemical and flow techniques. This is described in chapter 3, which includes all information about the EW-CRDS setup including alignment procedures.

(b) To test the capabilities of the new instrument (detection limits and sensitivity, spectral, temporal and spatial resolution), in condensed phase systems, through model experiments utilising EW-CRDS as a new type of spectroscopic probe of solution species in electrochemical processes at solid/liquid interfaces.

(c) Specifically to demonstrate the capabilities of the EW-CRDS technique. Points (b) and (c) are essentially discussed in the research chapters 4 – 6. This involved studies of Ag nanoparticle deposition and electrochemical dissolution (chapter 4) and the study of aniline polymerisation kinetics on silica (chapter 5). Additionally, the adsorption and the redox switching of cytochrome *c* on silica was investigated, employing a different light source (chapter 6).

(d) Extend the approaches in order to obtain time-resolved spectral information. This involved the use of a supercontinuum source and

the experimental setup was changed in order to carry out cavity

enhanced absorption experiments (chapter 7).

1.14 References

(1)   O'Keefe, A.; Deacon, D. A. G. *Review of Scientific Instruments* **1988**, *59*, 2544.

(2)   Jongma, R. T.; Boogaarts, M. G. H.; Holleman, I.; Meijer, G. *Review of Scientific Instruments* **1995**, *66*, 2821.

(3)   Scherer, J. J.; Paul, J. B.; Okeefe, A.; Saykally, R. J. *Chemical Reviews* **1997**, *97*, 25.

(4)   Wheeler, M. D.; Newman, S. M.; Orr-Ewing, A. J.; Ashfold, M. N. R. *Journal of the Chemical Society-Faraday Transactions* **1998**, *94*, 337.

(5)   Berden, G.; Peeters, R.; Meijer, G. *International Reviews in Physical Chemistry* **2000**, *19*, 565.

(6)   *Cavity-Ringdown Spectroscopy*
        An Ultrotrace-Absorption Measurement Technique; 1 ed.; Busch, K. W.; Busch, M. A., Eds.; American Chemical Society, Washington, DC, 1999.

(7)   Shaw, A. M.; Zare, R. N.; Bennett, C. V.; Kolner, B. H. *Chemphyschem* **2001**, *2*, 118.

(8)   Brown, R. S.; Kozin, I.; Tong, Z.; Oleschuk, R. D.; Loock, H. P. *Journal of Chemical Physics* **2002**, *117*, 10444.

(9)   Atkinson, D. B. *Analyst* **2003**, *128*, 117.

(10)   Zalicki, P.; Zare, R. N. *Journal of Chemical Physics* **1995**, *102*, 2708.

(11)   Salvato, G.; Ponterio, R. C.; Aliotta, F. *Review of Scientific Instruments* **2006**, *77*.

(12)   Engeln, R.; von Helden, G.; van Roij, A. J. A.; Meijer, G. *Journal of Chemical Physics* **1999**, *110*, 2732.

(13)   Pipino, A. C. R.; Woodward, J. T.; Meuse, C. W.; Silin, V. *Journal of Chemical Physics* **2004**, *120*, 1585.

(14)   Wilson, J.; Hawkes, J. F. B. *Optoelectronics An introduction*; Prentice-Hall: Englewood Cliffs, N.J., 1988.

(15)   Pipino, A. C. R.; Silin, V. *Chemical Physics Letters* **2005**, *404*, 361.

(16)   Xu, S. C.; Sha, G. H.; Xie, J. C. *Review of Scientific Instruments* **2002**, *73*, 255.

(17)   Muir, R. N.; Alexander, A. J. *Physical Chemistry Chemical Physics* **2003**, *5*, 1279.

(18)   Alexander, A. J. *Chemical Physics Letters* **2004**, *393*, 138.

(19)   Alexander, A. J. *Analytical Chemistry* **2006**, *78*, 5597.

(20)   Hallock, A. J.; Berman, E. S. F.; Zare, R. N. *Analytical Chemistry* **2002**, *74*, 1741.

(21)   Hallock, A. J.; Berman, E. S. F.; Zare, R. N. *Journal of the American Chemical Society* **2003**, *125*, 1158.

(22)   van der Sneppen, L.; Ariese, F.; Gooijer, C.; Ubachs, W. *Annual Review of Analytical Chemistry* **2009**, *2*, 13.

(23)   deFornel, F. *Evanescent Waves*; Springer, 2001.

(24)   Milosevic, M. *Applied Spectroscopy Reviews* **2004**, *39*, 365.

(25)   Wahling, G.; Raether, H.; Mobius, D. *Thin Solid Films* **1979**, *58*, 391.

(26)   Homola, J.; Yee, S. S.; Gauglitz, G. *Sensors and Actuators B-Chemical* **1999**, *54*, 3.

(27)   Kretschmann E., R. H. *Z. Naturforsch.* **1968**, *23A*, 2135.

(28)   Otto, A. *Z. Physik* **1968**, *216*, 398.

(29)   Janata, J.; Josowicz, M.; Devaney, D. M. *Analytical Chemistry* **1994**, *66*, R207.

(30)   Wink, T.; vanZuilen, S. J.; Bult, A.; vanBennekom, W. P. *Analyst* **1997**, *122*, R43.

(31)   Homola, J. *Analytical and Bioanalytical Chemistry* **2003**, *377*, 528.

(32)   Mulchan, N. M.; Rodriguez, M.; O'Shea, K.; Darici, Y. *Sensors and Actuators B: Chemical* **2003**, *88*, 132.

(33)   Marx, K. A. *Biomacromolecules* **2003**, *4*, 1099.

(34)   Swann, M. J.; Peel, L. L.; Carrington, S.; Freeman, N. J. *Analytical Biochemistry* **2004**, *329*, 190.

(35)   Lu, J. R.; Swann, M. J.; Peel, L. L.; Freeman, N. J. *Langmuir* **2004**, *20*, 1827.

(36)   Freeman, N. J.; Peel, L. L.; Swann, M. J.; Cross, G. H.; Reeves, A.; Brand, S.; Lu, J. R. *Journal of Physics-Condensed Matter* **2004**, *16*, S2493.

(37)   Sonesson, A. W.; Callisen, T. H.; Brismar, H.; Elofsson, U. M. *Colloids and Surfaces B-Biointerfaces* **2008**, *61*, 208.

(38)   Berney, H. B.; Oliver, K. *Biosensors & Bioelectronics* **2005**, *21*, 618.

(39)   Sonesson, A. W.; Callisen, T. H.; Brismar, H.; Elofsson, U. M. *Colloids and Surfaces B: Biointerfaces* **2007**, *54*, 236.

(40)   Gottesfeld, S. *Electroanalytical Chemistry* **1989**, *15*, 143.

(41)   Theeten, J. B.; Aspnes, D. E. *Annual Review of Materials Science* **1981**, *11*, 97.

(42)   Tiberg, F.; Jonsson, B.; Tang, J.; Lindman, B. *Langmuir* **1994**, *10*, 2294.

(43)   Tiberg, F.; Landgren, M. *Langmuir* **1993**, *9*, 927.

(44)   Brinck, J.; Jonsson, B.; Tiberg, F. *Langmuir* **1998**, *14*, 5863.

(45)   Welin, S.; Elwing, H.; Arwin, H.; Lundstrom, I.; Wikstrom, M. *Analytica Chimica Acta* **1984**, *163*, 263.

(46)   Dijt, J. C.; Stuart, M. A. C.; Fleer, G. J. *Advances in Colloid and Interface Science* **1994**, *50*, 79.

(47)   Kleijn, M.; Cohen Stuart, M.; de Wit, A. *Colloids and Surfaces A: Physicochemical and Engineering Aspects* **1996**, *110*, 213.

(48)   Pipino, A. C. R.; Hudgens, J. W.; Huie, R. E. *Review of Scientific Instruments* **1997**, *68*, 2978.

(49)   Shaw, A. M.; Hannon, T. E.; Li, F. P.; Zare, R. N. *Journal of Physical Chemistry B* **2003**, *107*, 7070.

(50)   Fan, H. F.; Li, F. P.; Zare, R. N.; Lin, K. C. *Analytical Chemistry* **2007**, *79*, 3654.

(51)   O'Reilly, J. P.; Butts, C. P.; I'Anson, I. A.; Shaw, A. M. *Journal of the American Chemical Society* **2005**, *127*, 1632.

(52)   Fisk, J. D.; Batten, R.; Jones, G.; O'Reilly, J. P.; Shaw, A. M. *Journal of Physical Chemistry B* **2005**, *109*, 14475.

(53)   Li, F. P.; Zare, R. N. *Journal of Physical Chemistry B* **2005**, *109*, 3330.

(54)   Hannon, T. E.; Chah, S. W.; Zare, R. N. *Journal of Physical Chemistry B* **2005**, *109*, 7435.

(55)   Fan, H. F.; Li, F.; Zare, R. N.; Lin, K. C. *Analytical Chemistry* **2007**.

(56)   Decher, G. *Science* **1997**, *277*, 1232.

(57)   Decher, G.; Hong, J. D.; Schmitt, J. *Thin Solid Films* **1992**, *210*, 831.

(58)   Decher, G.; Hong, J. D. *Berichte Der Bunsen-Gesellschaft-Physical Chemistry Chemical Physics* **1991**, *95*, 1430.

(59)   Hoffmannova, H.; Fermin, D.; Krtil, P. *Journal of Electroanalytical Chemistry* **2004**, *562*, 261.

(60)   Cheng, Y. F.; Corn, R. M. *Journal of Physical Chemistry B* **1999**, *103*, 8726.

(61)   Frey, B. L.; Jordan, C. E.; Kornguth, S.; Corn, R. M. *Analytical Chemistry* **1995**, *67*, 4452.

(62)   Romanini, D.; Kachanov, A. A.; Stoeckel, F. *Chemical Physics Letters* **1997**, *270*, 538.

(63)   Mazurenka, M.; Wilkins, L.; Macpherson, J. V.; Unwin, P. R.; Mackenzie, S. R. *Analytical Chemistry* **2006**, *78*, 6833.

(64)   Kuhnemann, F.; Muller, F.; von Basum, C.; Halmer, D.; Popp, A.; Schiller, S.; Hering, P.; Murtz, M. In *Conference on Nonlinear Fequency Generation and Conversion*; Schepler, K. L., Lowenthal, D. D., Eds. San Jose, CA, 2004, p 117.

(65)   Pipino, A. C. R.; Hudgens, J. W.; Huie, R. E. *Chemical Physics Letters* **1997**, *280*, 104.

(66)   Pipino, A. C. R. *Applied Optics* **2000**, *39*, 1449.

(67)   Aarts, I. M. P.; Pipino, A. C. R.; Hoefnagels, J. P. M.; Kessels, W. M. M.; van de Sanden, M. C. M. *Physical Review Letters* **2005**, *95*.

(68)   Schnippering, M.; Unwin, P. R.; Hult, J.; Laurila, T.; Kaminski, C. F.; Langridge, J. M.; Jones, R. L.; Mazurenka, M.; Mackenzie, S. R. *Electrochemistry Communications* **2008**, *10*, 1827.

(69)   Pipino, A. C. R. *Physical Review Letters* **1999**, *83*, 3093.

(70)   Pipino, A. C. R.; Hoefnagels, J. P. M.; Watanabe, N. *Journal of Chemical Physics* **2004**, *120*, 2879.

(71)   Aarts, I. M. P.; Pipino, A. C. R.; de Sanden, M.; Kessels, W. M. M. *Applied Physics Letters* **2007**, *90*.

(72)   Wang, C. J.; Scherrer, S. T. *Applied Optics* **2004**, *43*, 6458.

(73)   Wang, C. J.; Scherrer, S. T. *Optics Letters* **2004**, *29*, 352.

(74)   Tong, Z. G.; Jakubinek, M.; Wright, A.; Gillies, A.; Loock, H. P. *Review of Scientific Instruments* **2003**, *74*, 4818.

(75)   Li, R. K.; Loock, H. P.; Oleschuk, R. D. *Analytical Chemistry* **2006**, *78*, 5685.

(76)   von Lerber, T.; Sigrist, M. W. *Applied Optics* **2002**, *41*, 3567.

(77)   Tarsa, P. B.; Rabinowitz, P.; Lehmann, K. K. *Chemical Physics Letters* **2004**, *383*, 297.

(78)   Tarsa, P. B.; Wist, A. D.; Rabinowitz, P.; Lehmann, K. K. *Applied Physics Letters* **2004**, *85*, 4523.

(79)   Powell, H. V.; Schnippering, M.; Mazurenka, M.; Macpherson, J. V.; Mackenzie, S. R.; Unwin, P. R. *Langmuir* **2009**, *25*, 248.

(80)   Everest, M. A.; Black, V. M.; Haehlen, A. S.; Haveman, G. A.; Kliewer, C. J.; Neill, H. A. *Journal of Physical Chemistry B* **2006**, *110*, 19461.

(81)   Fan, H. F.; Hung, C. Y.; Lin, K. C. *Analytical Chemistry* **2006**, *78*, 3583.

(82)   Fisk, J. D.; Rooth, M.; Shaw, A. M. *Journal of Physical Chemistry C* **2007**, *111*, 2588.

(83)   Mazurenka, M.; Hamilton, S. M.; Unwin, P. R.; Mackenzie, S. R. *Journal of Physical Chemistry C* **2008**, *112*, 6462.

(84)   Adamczyk, Z. *Journal of Colloid and Interface Science* **2000**, *229*, 477.

(85)   Louder, D. R.; Parkinson, B. A. *Analytical Chemistry* **1995**, *67*, A297.

(86)   Quate, C. F. *Surface Science* **1994**, *299*, 980.

(87)   Butt, H. J. *Biophysical Journal* **1991**, *60*, 1438.

(88)   Noy, A.; Vezenov, D. V.; Lieber, C. M. *Annual Review of Materials Science* **1997**, *27*, 381.

(89)   Vinogradova, O. I.; Yakubov, G. E.; Butt, H. J. *Journal of Chemical Physics* **2001**, *114*, 8124.

(90)   Ducker, W. A.; Senden, T. J.; Pashley, R. M. *Nature* **1991**, *353*, 239.

(91)   Grutter, P.; Meyer, E.; Heinzelmann, H.; Rosenthaler, L.; Hidber, H. R.; Guntherodt, H. J. *Journal of Applied Physics* **1988**, *63*, 2947.

(92)   Grutter, P.; Meyer, E.; Heinzelmann, H.; Rosenthaler, L.; Hidber, H. R.; Guntherodt, H. J. *Journal of Vacuum Science & Technology a-Vacuum Surfaces and Films* **1988**, *6*, 279.

(93)   Arai, T.; Fujihira, M. *Journal of Electroanalytical Chemistry* **1994**, *374*, 269.

(94)   Senden, T. J.; Drummond, C. J.; Kekicheff, P. *Langmuir* **1994**, *10*, 358.

(95)   Gould, S. A. C.; Drake, B.; Prater, C. B.; Weisenhorn, A. L.; Manne, S.; Hansma, H. G.; Hansma, P. K.; Massie, J.; Longmire, M.; Elings, V.; Northern, B. D.; Mukergee, B.; Peterson, C. M.; Stoeckenius, W.; Albrecht, T. R.; Quate, C. F. In *4th International Conf on Scanning Tunneling Microscopy/Spectroscopy* Oarai, Japan, 1989, p 369.

(96)   Hansma, H. G.; Hoh, J. H. *Annual Review of Biophysics and Biomolecular Structure* **1994**, *23*, 115.

(97)   Hansma, H. G.; Kim, K. J.; Laney, D. E.; Garcia, R. A.; Argaman, M.; Allen, M. J.; Parsons, S. M. *Journal of Structural Biology* **1997**, *119*, 99.

(98)   Shao, Z. F.; Mou, J.; Czajkowsky, D. M.; Yang, J.; Yuan, J. Y. *Advances in Physics* **1996**, *45*, 1.

(99)   Vansteenkiste, S. O.; Davies, M. C.; Roberts, C. J.; Tendler, S. J. B. *Progress in Surface Science* **1998**, *57*, 95.

(100)   Weisenhorn, A. L.; Drake, B.; Prater, C. B.; Gould, S. A. C.; Hansma, P. K.; Ohnesorge, F.; Egger, M.; Heyn, S. P.; Gaub, H. E. *Biophysical Journal* **1990**, *58*, 1251.

(101) Hansma, P. K.; Cleveland, J. P.; Radmacher, M.; Walters, D. A.; Hillner, P. E.; Bezanilla, M.; Fritz, M.; Vie, D.; Hansma, H. G.; Prater, C. B.; Massie, J.; Fukunaga, L.; Gurley, J.; Elings, V. *Applied Physics Letters* **1994**, *64*, 1738.

(102) Putman, C. A. J.; Vanderwerf, K. O.; Degrooth, B. G.; Vanhulst, N. F.; Greve, J. *Applied Physics Letters* **1994**, *64*, 2454.

(103) Zhong, Q.; Inniss, D.; Kjoller, K.; Elings, V. B. *Surface Science* **1993**, *290*, L688.

(104) Wilson, N. R.; Macpherson, J. V. *Nature Nanotechnology* **2009**, *4*, 483.

(105) Bard, A. J.; Faulkner, L. R. *Electrochemical Methods. Fundamentals and Applications*; 2. ed.; John Wiley & Sons, Inc., 2001.

(106) El-Sayed, M. A. *Accounts of Chemical Research* **2001**, *34*, 257.

(107) Klimov, V. I.; Mikhailovsky, A. A.; Xu, S.; Malko, A.; Hollingsworth, J. A.; Leatherdale, C. A.; Eisler, H. J.; Bawendi, M. G. *Science* **2000**, *290*, 314.

(108) Link, S.; El-Sayed, M. A. *International Reviews in Physical Chemistry* **2000**, *19*, 409.

(109) Hao, E.; Schatz, G. C. *Journal of Chemical Physics* **2004**, *120*, 357.

(110) Kelly, K. L.; Coronado, E.; Zhao, L. L.; Schatz, G. C. *Journal of Physical Chemistry B* **2003**, *107*, 668.

(111) Rechberger, W.; Hohenau, A.; Leitner, A.; Krenn, J. R.; Lamprecht, B.; Aussenegg, F. R. *Optics Communications* **2003**, *220*, 137.

(112) Faraday, M. *Transactions of the Faraday Society* **1857**, 145.

(113) Mie, G. *Annalen der Physik* **1908**, 25.

(114) Taneja, P.; Ayyub, P.; Chandra, R. *Physical Review B* **2002**, *65*.

(115) Turkevich, J. *Discussions of the Faraday Society* **1951**, 11.

2 Experimental

This chapter describes the chemicals used in this project, as well as some of the experimental techniques. However, most of the experimental details are given in the relevant research chapters, since they provide a better context alongside the experimental techniques. EW-CRDS and electrochemistry is described in detail in Chapter 3.

2.1 Chemicals

All solutions were prepared using Milli-Q water (Millipore Corp., resistivity > 18 MΩ cm). The compounds were weighted on a four figure analytical balance (Sartorius A2008 and Adam AAA 100LE). Table 2.1 gives details about grades and suppliers for all chemicals used in this project.

Table 2.1: Grades and suppliers of chemicals used in this project.

Chemical	Supplier	Grade
Methanol	Acros	99.9 %
Poly-L-lysine hydrobromide	Sigma-Aldrich	N/A
Sodium citrate tribasic dihydrate	Sigma-Aldrich	> 99.0 %
Sodium borohydrate	Sigma-Aldrich	99 %
Silver nitrate	Sigma-Aldrich	> 99 %
Potassium hexachloroiridate(III)	Sigma-Aldrich	99.99 %
Potassium hexachloroiridate(IV)	Sigma-Aldrich	99.99 %
Potassium nitrate	Sigma-Aldrich	> 99.0 %
Aniline hydrochloride	Sigma-Aldrich	> 99.0 %
Potassium persulfate	Sigma-Aldrich	99.99 %
Hydrochloric acid 36 %	Fisher Scientific	Analytical reagent grade
Horse-heart Cytochrome c	Sigma-Aldrich	99 %
Potassium chloride	Fisher Scientific	Laboratory reagent grade
Sodium dithionite	Sigma-Aldrich	> 99 %
Ethylenediaminetetraacetic acid iron(III) hydrate sodium salt	Sigma-Aldrich	96 %

2.2 TM-AFM Instrumentation

A Digital Instruments multimode AFM with a Nanoscope IIIa controller (Veeco, U.S.A.) was employed for all TM-AFM measurements. The cantilevers were also purchased from Veeco (RFESP standard silicon tips).

Commercially available SPIP^{TM} software was used for statistical grain analysis in order to obtain the size and the size distribution of the Ag nanoparticles and polyaniline nanoparticles.

2.3 Electrochemical measurements

CVs were recorded using a CH Instruments potentiostat (model CHI730 A). Experiments were carried out using a standard three-electrode configuration consisting of a saturated calomel reference electrode (SCE, BAS Inc. Japan), a platinum wire counter electrode and either a Pt 2 mm diameter macroelectrode or an indium doped tin oxide (ITO) slide (resistance 4 – 8 Ω, Delta Tech. Ltd.). Solutions were degassed with N_2 for 15 min prior to each experiment.

3 The EW-CRDS setup

This chapter covers the description of all electronic and optical components used in the EW-CRDS setup, as well as some remarks about the custom written software programs. Essentially, one setup was built similar to an existing instrument employing a narrow bandwidth laser at 417 nm.[1] Different lasers were employed as light sources, however, most of the experiments were carried out using a diode laser emitting at 405 nm. The setup comprises of the laser, several optical components such as lenses, mirrors to lead the beam into the cavity, high reflective cavity mirrors, a prism and a photomultiplier tube (PMT) to record the EW-CRDS signal. All components were mounted on an optical table (Thorlabs), although it was found that it was not necessary to float the table. Electronic components were used to modulate the laser (TTL modulation), display the modulation and ring-down signals (oscilloscope) and record the data (data acquisition (DAQ) card). In several experiments, a 2 mm diameter Pt working electrode controlled by a potentiostat was employed to probe the silica / water interface in a thin layer cell arrangement.

3.1 Light Source

For most EW-CRDS experiments described in the following chapters, a blue diode laser (Power Technology Inc.) was used as the light source. The unit emitted light at 405 nm and had a maximum output power of 60 mW. The bandwidth of the laser was about 1 nm.

In a different setup, a red diode laser (Power Technology Inc.) emitting light at 658 nm was used. The maximum output power of this laser was 70 mW, and the bandwidth was also 1 nm. Both lasers are classed as 3B lasers. The lasers are operated in continuous wave (CW) mode, have a beam divergence of less than 0.5 mrad and can be modulated.

All lasers were powered by a Laser Diode Control Unit (LDCU). This device ensured a maximal input voltage of 5 V. Additionally, the unit was controlled by a laser safety interlock system.

The lasers were modulated using TTL modulation with a 10 MHz pulse generator (Thurlby Thandar Instruments, TGP110). TTL modulation requires an input voltage on the BNC connector of the laser. In order to yield 100 % output power, the control voltage needed to be 0 V. For 0 % output power, the voltage was set to 5 V.

More detail about the supercontinuum source used for the BBCEAS experiments (Chapter 7) can be found in section 7.1.1.

3.2 Oscilloscope

An oscilloscope (Tektronix TDS2022B) was used to display the TTL modulation signal and the PMT response, in order to facilitate the alignment process. The oscilloscope had two input channels which could be used to display time-dependent voltage signals. In principle, the oscilloscope could also have been used as a data acquisition device, but for our purpose it was only employed to display the PMT and the modulation signal. The oscilloscope was mainly used to ensure optimal alignment of the optical components and maximise the ring-down time.

3.3 Optics

Most optics were purchased from Thorlabs or Newport unless otherwise stated. The optical components were stored in their original packaging when not in use.

3.3.1 Cleaning Procedure

All optics used for spectroscopic experiments had to be cleaned regularly. The components were wiped with a drop of spectroscopic grade methanol (Sigma-Aldrich) using lens cleaning tissue. The optical element was placed on a flat surface with a lens cleaning tissue underneath it. Then loose dust particles were removed with compressed air and a sheet of lens cleaning tissue was placed onto the optic. A drop of methanol was applied on top of

the optic and the tissue was pulled away. Usually, this process was repeated several times.

3.3.2 Turning Mirrors

Two mirrors were used to couple light into the optical cavity. The mirrors were purchased from either Newport (for the 405 nm setup) or Thorlabs (for the 658 nm setup). In the former case, the mirrors were coated with a MgF dielectric coating. In the latter case, the mirrors were coated with a protected silver layer.

3.3.3 Cavity Mirrors

All cavity mirrors were purchased from Los Gatos Research (USA) and had a radius of curvature of 1 m. The reflectivity was chosen to match the wavelength of the laser. For the 405 nm laser setup, the maximal reflection wavelength of the cavity mirrors was 405 nm, whereas for the 658 nm laser setup, the centre wavelength was 635 nm. The mirrors were placed in Gimbal mounts to ensure that the position of the mirrors remained stationary and that rotation was only possible when adjusting the mirrors. Figure 3.1 shows a graph from the manufacturer displaying the optical transmission of the 405 nm mirrors as a function of wavelength.[2] As shown in the figure, the coating of the mirrors was optimised to possess the highest reflectivity at 405 nm.

It was very important to clean the cavity mirrors prior to each experiment using the cleaning procedure mentioned above.
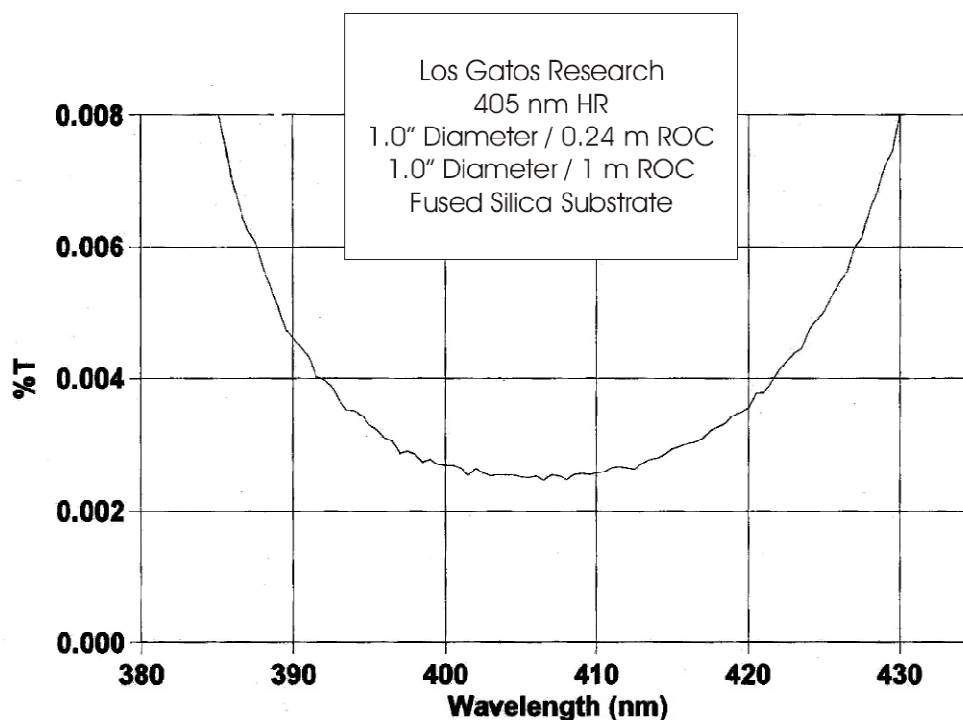
Figure 3.1: Mirror transmission for the Los Gatos Research 405 nm cavity mirrors as a function of wavelength. The coating was optimised for high reflectivity at 405 nm with a transmission of less than 0.003 %. (taken from Ref.[2])

3.3.4 Prism

The prism is the most important optical component in the EW-CRDS setup. The prisms used for the EW-CRDS experiments were rectangular shaped, made from UV grade fused silica and had an antireflective coating on each of the short sides. The hypotenuse side was uncoated and superpolished down to a roughness of $\lambda/20$ (measured at 633 nm). Figure 3.2 shows schematically the geometry of the prism. For the broadband experiments described in chapter 7, a different shaped prism was employed (see section 7.1.1).

In addition to the cleaning procedure mentioned, the prisms were cleaned in an oxygen plasma in order to remove any organic remains from previous experiments such as polymers and organic molecules. The prisms were ashed between 5 min and 20 min in a Emitech K1050X plasma asher at a pressure of around 0.6 mbar at 100 W. The prisms were inserted into a custom made PTFE holder, which only exposed the hypotenuse side of the prism, in order to protect the antireflective coating on the short sides from the oxygen plasma.
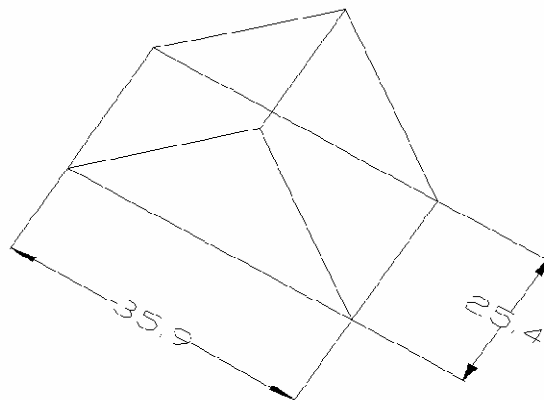
Figure 3.2: Schematic representation of the right angle prism used for most experiments. The dimensions are displayed in mm.

Table 3.1 summarises the technical details of the two types of prisms used.

Table 3.1: Parameters for the right angle prism provided by the manufacturers

Company	Laser Components	CVI	CVI
Reflectivity and Wavelength range	405 – 417 nm	< 0.5 % at 355 – 532 nm	< 0.5 % at 424 – 675 nm
Length	1.0'' (±0.1mm)	1.0'' (±0.1mm)	1.0'' (±0.1mm)
Angle of incidence for AR coating	35º ± 3º	0º	0º
Surface roughness at 633 nm	λ/20	λ/10	λ/10

After the cleaning procedure, the prism was then inserted into a custom made aluminium holder manufactured by the departmental mechanical workshop which was mounted on a breadboard. The holder had two holes where the laser beam entered and exited the prism. Figure 3.3 shows a photograph of the prism in its prism holder. As shown in the picture, the prism holder also comprised of two screws on the top which could be used to push down a cell in order to carry out experiments in the condensed (liquid) phase.
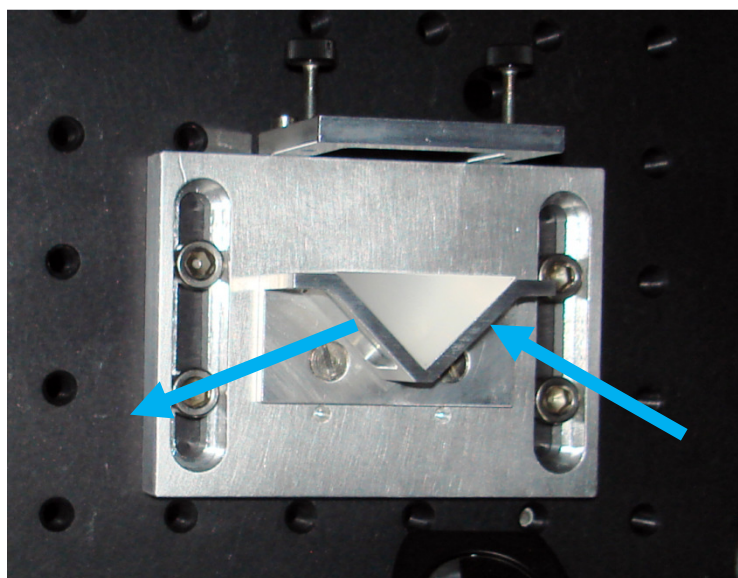
Figure 3.3: Photograph of the prism holder and prism mounted on the blackboard.

3.3.5 Cells

Circular cells made from polytetrafluoroethylene (PTFE), open at the top and bottom ends were used in most of the experiments. The volume of the cells was approximately 3 mL and covered an area on the prism of 1.7 cm^2. The bottom side had a small indentation in which an O-ring (James Walker) was fitted. An aluminium slide with a cell-sized hole was used to push the cell down onto the prism in the prism holder by the two screws mounted on the holder.

3.4 Photomultiplier tubes

PMTs were used to measure the light intensity leaking out of the optical cavity. PMTs are based on the photoelectric effect: when a photon enters a metal surface (the photocathode), it can be absorbed and give up its energy to an electron. If the transferred energy is higher than the surface potential barrier, the electron can escape. In a PMT, the photoelectrons are accelerated in an electric field towards electrodes (or dynodes). The series of dynodes are maintained at increasing potentials with respect to the cathode. When the photoelectrons hit the dynodes, several secondary electrons are emitted which are accelerated towards the next dynode and hence amplify the resulting detection current. The current amplification factor between the cathode and the anode is given by

$$G = \delta^N \tag{3.1}$$

where δ is the average secondary electron yield and N the number of dynodes. Typical voltages used for PMTs are 200 – 1000 V and considerable amplification is possible (for example if $\delta = 5$ and $N = 9$, we obtain a gain of 2 x 10^6). The transit time between the electrodes within the PMT limits the response time which is usually less than 30 ns.

Care has to be taken to not saturate the PMT. Generally, if the incoming light beam possesses a relatively high power, the applied voltage between the anode and the cathode within the PMT has to be decreased.

3.5 Alignment procedure

3.5.1 Safety Considerations

Although the lasers used are only classed 3B, it was crucial that watches, bracelets, rings and other reflective jewellery were removed before setting up or changing the experimental setup. Laser safety eyewear was also worn. The diode laser was run at low power for the whole alignment procedure, except when aligning the electrode above the evanescent field.

3.5.2 Alignment

The experimental setup for the ring cavity is displayed in figure 3.4. As mentioned above, the laser was run at low power for the initial part of the alignment process. Once the front cavity mirror (M1) was inserted, the power was increased to facilitate the alignment process of the optical cavity.
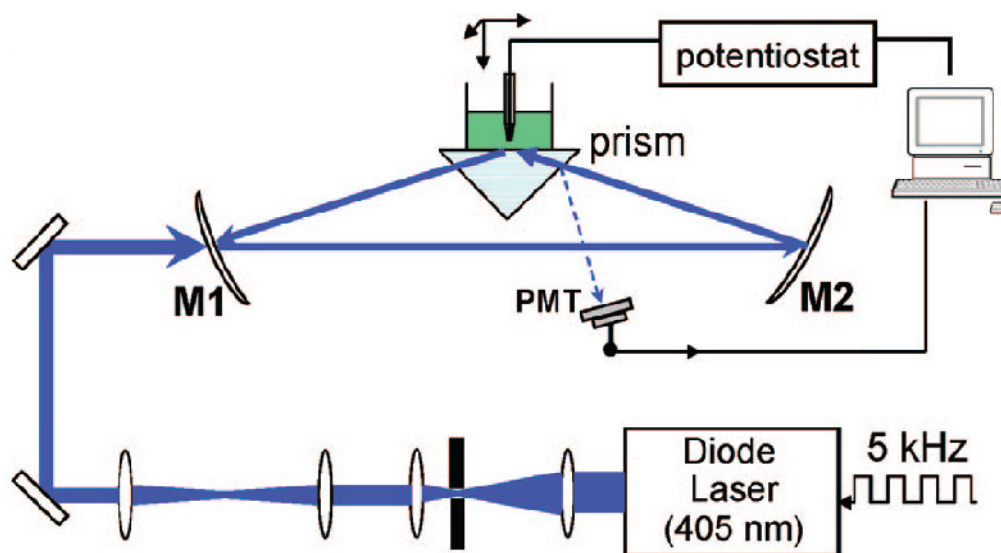
Figure 3.4: Schematic representation of the alignment of the 405 nm ring cavity.

First, the laser light from the diode laser was led into a telescope tube consisting of two lenses with two different focus lengths (35 mm and 75 mm) in order to decrease the footprint of the beam as shown in figure 3.5.
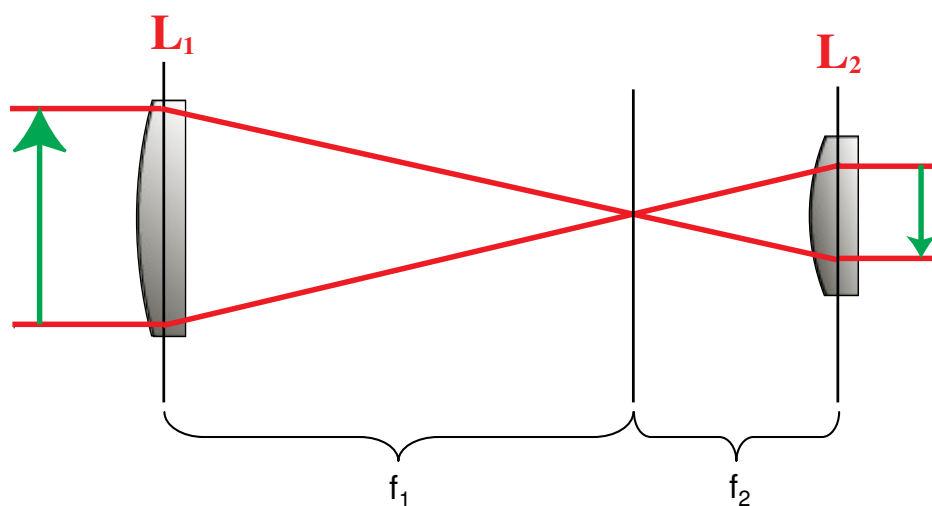
Figure 3.5: Schematic representation of the telescope used in the experimental EW-CRDS setup. The first lens, where the laser beam enters the telescope (L_1) had a focal length (f_1) of 75 mm, whilst the second lens (L_2) had a focal length (f_2) of 35 mm.

The beam was then led via the two turning mirrors into the optical cavity and aligned through two custom-made pinholes (hole diameter: 1 mm) which were placed into the gimbal mounts for the cavity mirrors. Although it was found that the cavity alignment was fairly stable for a few weeks without alignment, regular realignment of the cavity is recommended to ensure that reproducible data is obtained and that the reference ring-down time is optimal.

The mirror holders, as well as the holder for the prism, were attached to a breadboard. The direction of the laser beam was changed by tweaking the turning mirrors until the beam was well aligned through the two pinholes. Then, the pinhole at the position of mirror 2 (shown in Figure 3.4) was replaced with one of the cavity mirrors. The laser beam now entered the prism (at an angle smaller than the critical angle of 42.92°) and was total internally reflected at the hypotenuse side. The beam was aligned in such a way, that the point of TIR is in the middle of the hypotenuse side. At this stage of the alignment procedure, other components such as macroelectrodes or capillaries could be aligned over the evanescent field by micropositioners.

The micropositioners used consisted of a set of three orthogonally mounted linear stages equipped with differential micrometers. The micrometers were adjustable by hand. The micropositioner for the z (vertical) direction was set to zero and the electrode or capillary was then inserted into the holder and moved towards the prism surface (slightly away of the evanescent field to prevent damage to the silica surface) and

69

tightened. The electrode or capillary was then moved away again from the surface by the micropositioner and aligned over the evanescent field.

Part of the beam was reflected at the rectangular side of the prism and this reflected beam was used to measure the light intensity in the optical cavity and was therefore fed via a turning mirror into the PMT. The intensity of the modulated laser pulse could thus be displayed on the oscilloscope. The prism holder then had to be aligned in such a way that the beam, after leaving the prism again, hit the pinhole of the first cavity mirror mount. Finally, this pinhole was replaced by a cavity mirror. The position where the laser beam hit the photodetector within the tube was optimised by correcting the turning mirror until the signal on the oscilloscope was maximised.

The steps of aligning the evanescent field on the prism, and the turning of the prism holder, may have to be repeated several times until the evanescent field was exactly in the centre of the prism and the exiting laser beam hit the pinhole in the first cavity mirror (M1) holder. Then, the cavity mirror could be inserted into its holder and, at this point, several round trips of the light (at least 3) should be seen on the second mirror. By changing the position of the first cavity mirror, it was possible to overlay the round trip spots. If the laser was modulated, a ring-down decay could now be observed on the oscilloscope. In order to optimise the position of a macroelectrode over the evanescent field, the electrode was positioned using the x, y micropositioners at a very close distance (few tens of μm) over the evanescent field while simultaneously monitoring the change in the ring-down time as observed on the oscilloscope.

As already highlighted in the introduction, the ring-down time depends on the reflectivity of the mirrors and losses of the prism (due to scattering and quality of the antireflective coating). It was found, that prisms from CVI led to higher ring-down times (up to 700 ns) than Laser Component prism, where the maximum ring-down time was usually around 350 ns. This can be attributed, most likely, to the different antireflective coatings. Once the optical cavity was aligned, the ring-down time could usually be increased by slightly tweaking mirror 1. Mirror 2 should not be changed, because that affected the position of the evanescent field. Figure 3.6 shows typical traces of the modulation signal and the corresponding ring-down decay as seen on the scope. The upper curve (orange) corresponds to channel 1 of the oscilloscope and displays the modulation of the diode laser (controlled by the TTL modulation generator). Channel 2 corresponds to the EW-CRDS signal from the PMT.
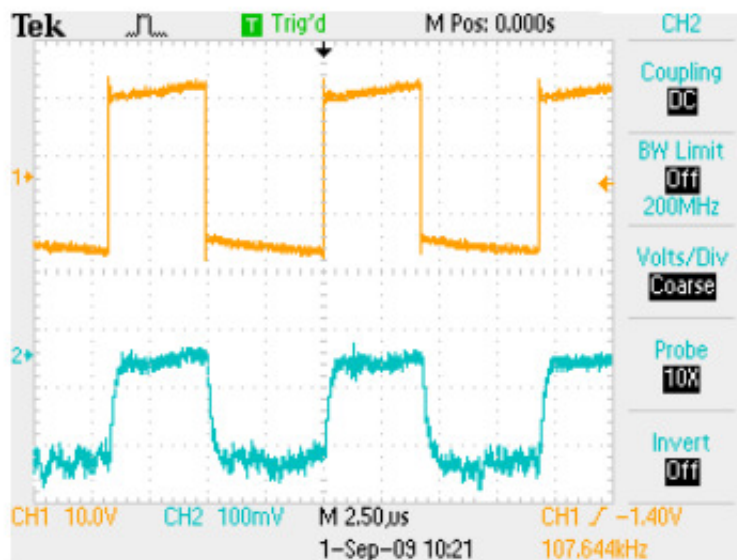
Figure 3.6: Screenshot of the oscilloscope. Channel 1 (orange) displays the modulation signal from the TTL modulation generator. Channel 2 corresponds to the PMT signal.

3.6 Electrochemistry setup

Figure 3.7 shows schematically the electrochemical part of the experimental setup. A home-built potentiostat was used for all electrochemical measurements described in this thesis. Working, reference and counter electrodes could be connected directly to the potentiostat via BNC connectors. The applied voltage between working and reference electrode was controlled externally by a DAQ card (National Instruments, PCIe-6221). The current flowing between working and counter electrodes was transformed into a voltage signal by the potentiostat via variable resistances (switchable between 1 kΩ and 10 MΩ) and recorded with the DAQ card. An interface box was used to connect the BNC output (applied voltage) and BNC input (measured current / voltage) signals with the DAQ card. In order to ensure, that the electrodes were always at open circuit potential when not in use, a switch was built in between the applied voltage from the computer and external voltage input of the potentiostat.
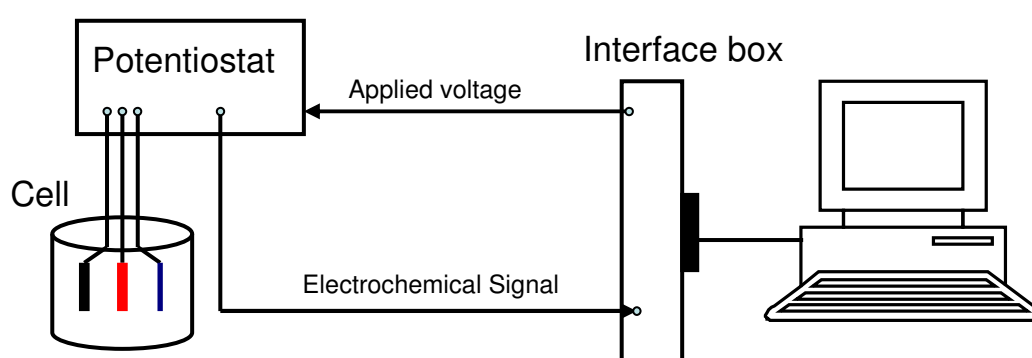
Figure 3.7: Schematic representation of the electrochemical part of the experimental setup. Both the applied voltage and the measured electrochemical signal are transferred to the computer via the interface box.

3.7 Data Acquisition

Two DAQ cards (Gage Applied Technologies, CS12400 and National Instruments, PCI-5124) were employed to transfer the EW-CRDS signal and the electrochemistry data to the computer. Custom written LabVIEW software (see below) was used to ensure data synchronisation.

3.7.1 EW-CRDS Signal Acquisition

The 12 bit DAQ cards for EW-CRDS data acquisition needed to operate at high speed. The sampling rate was 400 MS s^{-1} for the Gage card and 200 MS s^{-1} for the National Instrument card, respectively. High speed data acquisition was necessary because a whole set of data points (*i.e.* a ring-down trace) has to be transferred at a relatively high repetition rate. The modulation of the laser was chosen to be on a timescale of 50 μs, and a large fraction (but not all) of the ring-down traces were transferred to the card giving a repetition rate of *ca*. 2.4 kHz on average, which was limited by the DAQ card. The traces were stored in the buffer of the card, averaged, and then transferred to the computer. The data processing and conversion of the ring-down traces to ring-down times (via Fast Fourrier Transformation, see below) was then carried out by the LabVIEW program.

3.7.2 Electrochemistry Data Acquisition

The program to control the acquisition was combined with the EW-CRDS program to ensure optimal synchronisation. More about the software used can be found in the sections below.

3.8 Software

All software was written in National Instruments LabVIEW (versions 7.1/8.0/8.2). LabVIEW is based on modules which are called virtual instruments (VIs). VIs consist of a front panel, which is designed in a way to mirror a real front panel of an instrument (*i.e.* with switches, controls, graphs etc.) where the user interacts with the instrument, and a back panel, where the code of the program can be written and/or modified. Figure 3.8 shows a screenshot of the front panel of the program used for EW-CRDS and CV data acquisition.
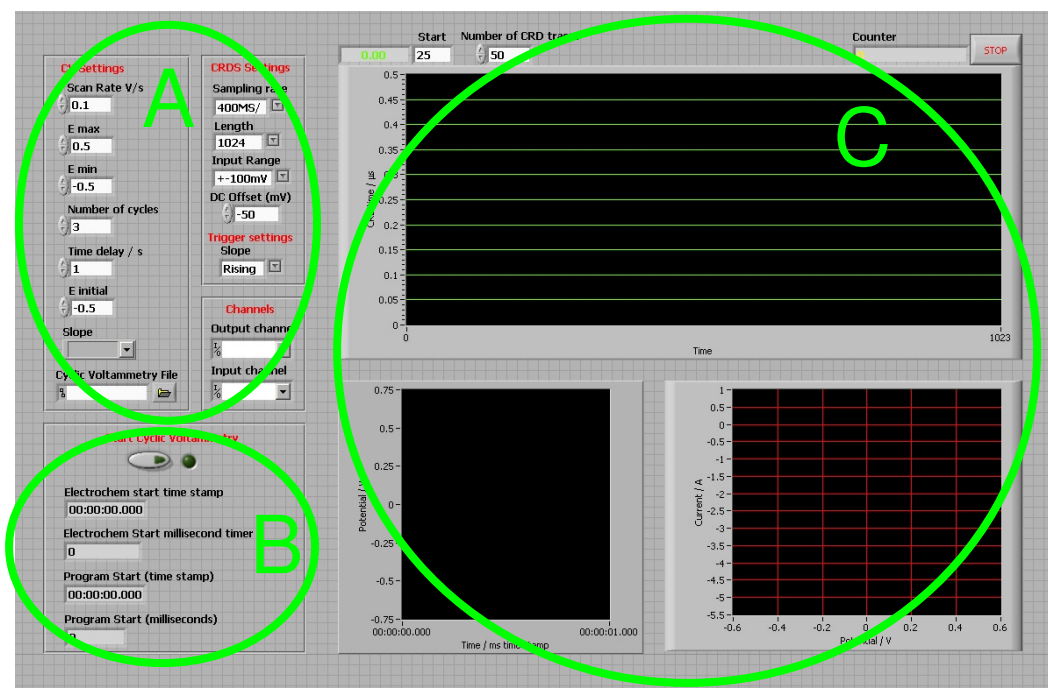
Figure 3.8: Screenshot of the front panel of the LabVIEW program used for EW-CRDS and CV experiments. A) Settings for the EW-CRDS and CV experiments, B) Start switch for performing an electrochemical experiment (CV) and time stamps for data synchronisation, C) Plots for data display, top: ring-down time as a function of time, bottom left: applied potential for CV experiments, bottom right: CV response.

The code is based on graphical programming rather than on command lines. Most DAQ cards can be accessed using this software and companies often provide basic LabVIEW VIs for data procession.

3.8.1 EW-CRDS LabVIEW program

The EW-CRDS program was responsible for time-resolved acquisition and averaging (usually 50 or 100 times) of the ring-down traces from the DAQ card and extraction of the corresponding ring-down time. Figure 3.9 shows a single ring-down trace as measured by the PMT and read by the program.

It can be seen, that the ring-down trace can be fitted easily to a single exponential fitting function.
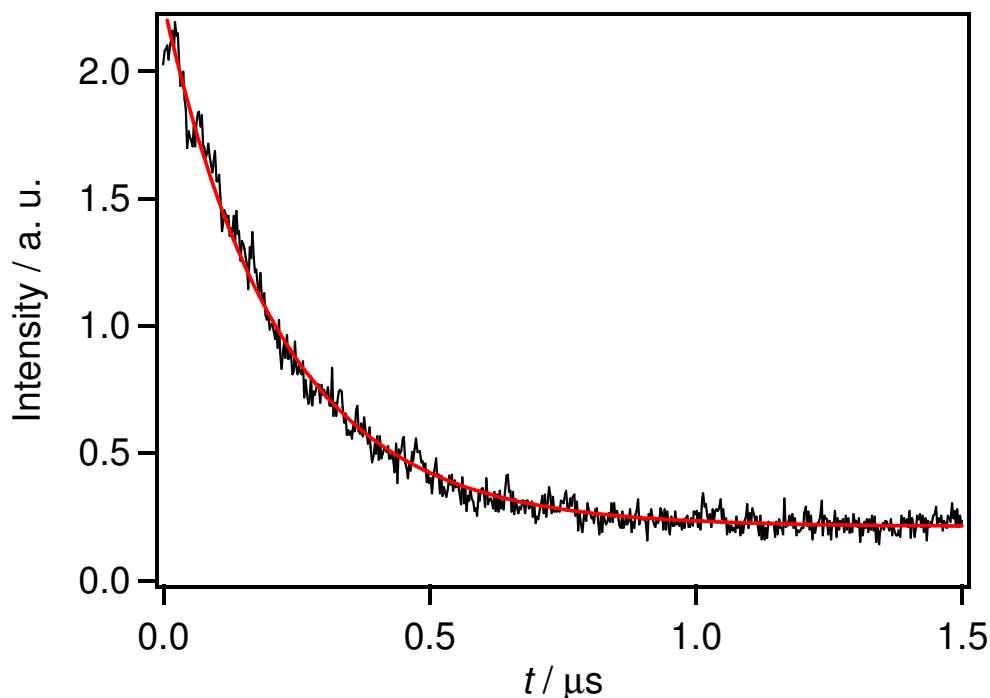
Figure 3.9: Experimental single ring-down trace for an empty ring cavity as read by the EW-CRDS program. The red line corresponds to a single-exponential fit. Usually multiple ring-down traces will be averaged and the ring-down time will be calculated using the FFT method. The corresponding decay (ring-down time) in this example was 220 ns.

The core feature of the EW-CRDS program is the Fast Fourier Transform (FFT) analysis sub VI which converted the measured ring-down traces from the DAQ card into their characteristic decay times (ring-down time).[3] Figure 3.10 shows the program code for the FFT sub VI. The exponential decay curves (with amplitude A, offset B and decay constant τ) are converted according to the equation

$$F(\omega) = J(Ae^{-\tau t} + B) \tag{3.2}$$

where J is the Fourier transform operator. At every non-zero frequency ω, the ratio of the real and imaginary components of $F(\omega)$ is $-\tau/\omega$ and therefore independent of the amplitude and offset. The amplitude and the baseline can then be calculated using the previously obtained τ.

$$A = \frac{(\omega^2 + \tau^2)}{\tau} \frac{Re[F(\omega)]\Delta t}{1 - e^{\tau t_m}} \tag{3.3}$$

$$B = \frac{F(0)}{N - (A_0/\tau t_m)}(1 - e^{-\tau t_m}) \tag{3.4}$$

where t_m is the time of the last observation in the ring-down decay which was analysed, N is the number of data points in the Fourier transform and $\Delta t = t_m/N$. With this method it is therefore possible to analyse the ring-down traces without having to extract the baseline offset. Additionally, this method is also very fast, because every transient can be analysed immediately and no iterative steps are necessary.[3] It is important to note, that this analysis is only possible with single-exponential decay curves.

The exponential decay curves and the sampling frequency are fed into the programme. After the conversion into ring-down times, the data is fed back into the EW-CRDS VI and averaged.
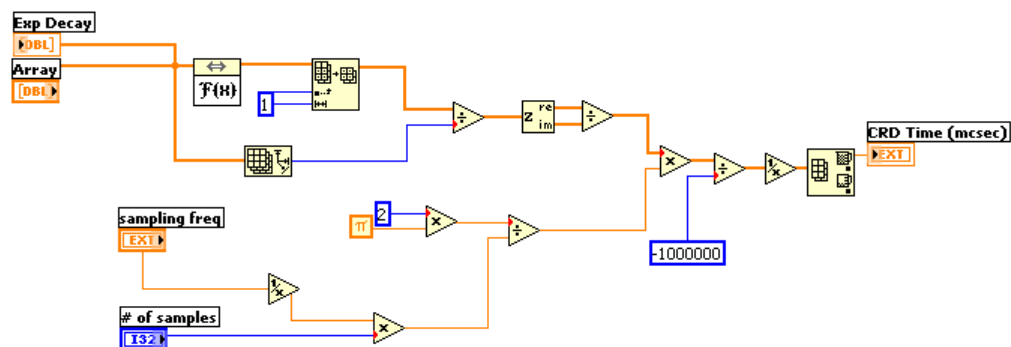
Figure 3.10: Screenshot of the sub VI responsible for converting the ring-down traces into ring-down times.

3.8.2 Electrochemistry LabVIEW program

The LabVIEW VI for the electrochemical measurements was designed to be executed whilst the EW-CRDS program was running simultaneously. When the electrochemistry button (see figure 3.8B) was pushed, a separate loop within the EW-CRDS program started. The program generated a triangular wave form using the chosen start and end potential and the scan rate. A separate sub-VI called Analog I/O defined the input and output channels on the PCIe card and converted the digital waveform signal to an analogue voltage. Simultaneously, the input voltage from the current measurement was converted into a digital signal to be read by the electrochemistry VI. The generated triangular wave and the measured current/voltage was then displayed and saved by the computer. Figure 3.11 shows the program code for the electrochemistry section of the program. Another program was designed to perform chronoamperometric step experiments which was very similar to the program described above but

instead of a triangular waveform, voltage steps were generated, where the step duration and step potential could be chosen on the front panel.
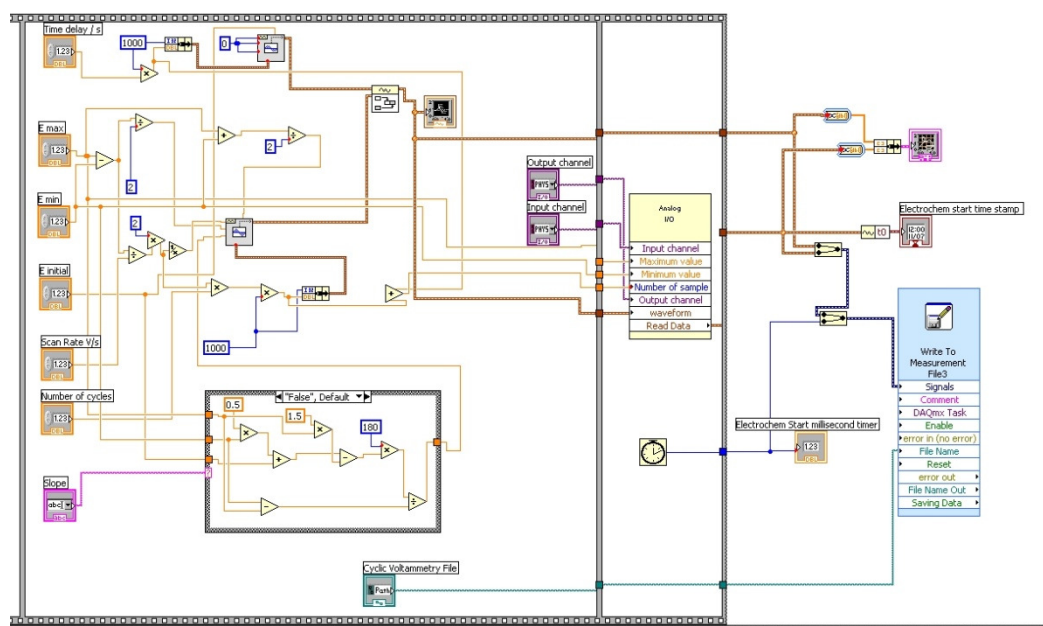
Figure 3.11: Screen shot of the program code of the electrochemistry VI.

In all electrochemistry VIs, the program recorded the timestamp when the main program, as well as the electrochemistry loop, was executed. By comparing the two time stamps, it was possible to synchronise the data and define exactly at which time the electrochemical experiment was started.

3.9 References

(1)   Mazurenka, M.; Wilkins, L.; Macpherson, J. V.; Unwin, P. R.; Mackenzie, S. R. *Analytical Chemistry* **2006**, *78*, 6833-6839.

(2)   Los   Gatos   Research   Inc   *accessed   on   09.11.2009* **http://www.lgrinc.com/documents/405-HR.pdf**.

(3)   Mazurenka, M.; Wada, R.; Shillings, A. J. L.; Butler, T. J. A.; Beames, J. M.; Orr-Ewing, A. J. *Applied Physics B-Lasers and Optics* **2005**, *81*, 135-141.

4 Surface Assembly and Redox Dissolution of Silver Nanoparticles

The adsorption kinetics of Ag nanoparticles on a silica surface modified with PLL have been measured *in situ* by following the interfacial optical absorbance at 405 nm using EW-CRDS. Sensitivity towards nanoparticle detection is enhanced due to the plasmon resonance of the Ag nanoparticles. The redox-dissolution kinetics of the immobilised nanoparticles have been investigated using two distinct approaches. First, $IrCl_6^{2-}$ was generated electrochemically from $IrCl_6^{3-}$ by a chronoamperometric potential step in a thin layer cell configuration formed between the silica surface and a Pt macroelectrode. The oxidative dissolution kinetics were obtained by monitoring the EW-CRDS signal as the nanoparticles dissolved. The reaction kinetics were extracted using complementary finite element modelling of diffusional and reaction processes. The second method of dissolution investigated involved the injection of $IrCl_6^{2-}$ (aq) directly at the surface by means of a microcapillary located close to the evanescent field.

4.1 Introduction

Immobilised arrays of metal nanoparticles continue to attract considerable attention for electronic and sensing applications,[1-3] including biosensing and the study of protein interactions.[4-8] In the latter context, Ag nanoparticles have proven useful for staining applications, which enables the visualization of proteins and DNA, and as an integral component of antibacterial coatings. Ag nanoparticles can be functionalised with oligonucleotides for DNA sensing applications[9] or act as bridge materials for electron transfer reaction from proteins to electrodes.[10] It has also been shown that Ag nanoparticles can be used as substrates for surface-enhanced Raman scattering (SERS).[11-13]

For these applications, and others, understanding reactions at the nanoscale, especially electron transfer at nanostructures and metal nanoparticles, is very important. The oxidative etching kinetics of metal surfaces were probed in earlier scanning electrochemical microscopy (SECM) work by us[14] using tris(2,2'-bipyridyl)ruthenium(III) and Br_2 as electrogenerated oxidants. Only a few studies have investigated the dissolution of nanoparticles, either in solution by varying the pH[15-17] and through O_2 purging,[18] or embedded in a glass matrix. In the latter case, the particles were dissolved using heat,[19] ultrafast laser pulses[20] or intense electric fields.[21, 22] In all these examples, analysis was performed either *ex-situ* or in bulk using conventional UV-vis spectroscopy. To date there have been no time-resolved studies of the dissolution kinetics of metal

nanoparticles on insulating surfaces. In order to monitor and rationalise these processes, rather sensitive analytical techniques are needed.

The redox mediator $[IrCl_6]^{3-/4-}$ has been employed in several previous studies to dissolve Ag nanoparticles. For example, it has been applied to protein detection using SECM (generation of $IrCl_6^{2-}$ from $IrCl_6^{3-}$ at an ultramicroelectrode) after Ag staining[23] and for Ag enhanced fingerprint determination.[24] The formation of electrochemically-generated Ag nanoparticles has been investigated by Rodriguez-Sanchez *et al.*[25] In all these studies, the Ag nanoparticle dissolution/growth was either detected indirectly using surface sensitive techniques such as scanning electron microscopy and X-ray scattering or time-resolved by bulk UV-vis spectroscopy. It has not been possible to combine both approaches.

The kinetics of the redox dissolution of Ag colloidal particles were also obtained by combining EW-CRDS with electrochemistry. The nanoparticles were dissolved using the redox compound $IrCl_6^{2-}$ which was electrochemically generated from the reduced (non-reactive) form, $IrCl_6^{3-}$, at a strategically located electrode just above the silica surface. $IrCl_6^{2-}$ oxidises Ag^0 to Ag^+ causing dissolution of the nanoparticles. Studies were carried out for various concentrations of $IrCl_6^{3-}$ and different electrogeneration times, using a potential step method. The experimental data, in the form of interfacial absorbance-time plots, were used to calculate the rate constant of the dissolution process after solution of the underlying mass transport problem.

A second method of Ag colloid dissolution was also tested, in which a simple micropipette was used to dispense the reagent ($IrCl_6^{2-}$ solution) directly in the region of the immobilised nanoparticles. The dissolution process was followed as a function of $IrCl_6^{2-}$ concentration and flow rate. These initial studies provide a platform for the further use of this technique.

4.2 Theory

In order to extract kinetic parameters from the experimental observations, we fitted the data obtained to a simple model, encapsulating the diffusion of the electrogenerated species and the kinetics of dissolution. The model was developed for the electrochemical arrangement shown in Figure 4.3 (see below) and described below. A 2 mm diameter disc electrode was positioned 180 μm ± 20 μm above a prism surface bearing the Ag nanoparticles and was used to generate the oxidant, $IrCl_6^{2-}$, from $IrCl_6^{3-}$, local to the surface. Experiments showed that the Ag nanoparticles on the surface were highly dispersed, but as the interparticle spacing was much smaller than the electrode–prism separation, d, it is reasonable to treat the reactive prism surface as uniform (for the purpose of modelling) and diffusion between the electrode and prism as planar. The model considers the diffusion of the mediator within the thin layer cell coupled to the dissolution of the Ag layer at the prism boundary and calculates the absorbance of the Ag layer with time, as described later.

4.2.1 The Diffusional problem

The diffusion of species i, with concentration $c_i(z,t)$, in a one dimensional domain is given by

$$\frac{\partial c_i(z,t)}{\partial t} - D_i \frac{\partial^2 c_i(z,t)}{\partial z^2} = 0 \tag{4.1}$$

for $z \in [0,d]$ where d is the distance between the prism and the electrode, and D_i is the diffusion coefficient of species i ($IrCl_6^{3-}$ or $IrCl_6^{2-}$). The boundary conditions for the reduced, $IrCl_6^{3-}$, and oxidised, $IrCl_6^{2-}$, forms of the mediator, denoted $c_R(z,t)$ and $c_O(z,t)$ respectively, in this case are given by

$$c_R(0,t) = 0$$
$$D_O \frac{\partial c_O}{\partial z}(0,t) = -D_R \frac{\partial c_R}{\partial z}(0,t) \tag{4.2}$$
$$-D_O \frac{\partial c_O}{\partial z}(d,t) = D_R \frac{\partial c_R}{\partial z}(d,t) = k_{app} c_O \theta$$

for $0 < t \leq t_{step}$, where t_{step} is the potential step time (the duration of the electrogeneration period) and

$$c_O(0,t) = 0$$
$$D_O \frac{\partial c_O}{\partial z}(0,t) = -D_R \frac{\partial c_R}{\partial z}(0,t) \tag{4.3}$$
$$-D_O \frac{\partial c_O}{\partial z}(d,t) = D_R \frac{\partial c_R}{\partial z}(d,t) = k_{app} c_O \theta$$

for $t_{step} < t$. Here k_{app} is the Ag dissolution rate constant and θ is the effective fractional surface coverage of Ag atoms on the prism. Our focus is on initial rate measurements which allow us to neglect the small build up

of Ag^+ that will occur in the thin layer cell during the dissolution process. Additionally, because the change in particle size during dissolution is small, the rate constant was assumed to be independent of the nanoparticle size. These boundary conditions were coupled to an ordinary differential equation describing the dissolution of Ag at the prism surface

$$N\frac{d\theta}{dt} = -k_{app}c_O(d,t)\theta \qquad (4.4)$$

where N is the initial Ag atom surface concentration on the prism. The model assumes that the nanoparticle distribution on the surface is equivalent to the same amount of Ag adsorbed atomically to the surface. N was computed assuming face-centred cubic (fcc) packing for the Ag atoms in the nanoparticle using the concentration of nanoparticles per unit area, N_{NP}:

$$N = \frac{\pi}{6}\frac{\rho(2a)^3 N_A}{M}N_{NP} \qquad (4.5)$$

where ρ is the density of Ag (10.5 g cm^{-3}), a the average radius of Ag nanoparticles obtained by TM-AFM measurements, N_A is Avogadro's constant and M the molecular weight of Ag (107.87 g mol^{-1}).

Due to mass conservation of the redox couple within the thin layer cell and the equality of the diffusion coefficients of the oxidised and reduced forms of the mediator, the concentrations at any point are related by

$$c_R + c_O = c_R* \qquad (4.6)$$

where $c_R{}^*$ is the original bulk concentration of $IrCl_6{}^{3-}$. Thus, it is only necessary to solve the diffusion equation numerically for either c_O or c_R and θ.

4.2.2 Modelling changes in interfacial absorbance

To compute the interfacial absorbance with time the average nanoparticle size obtained by TM-AFM measurements was considered. The initial Ag nanoparticle surface concentration is known from TM-AFM measurements and the change in nanoparticle size with time was computed from the flux at the interface (eqs. 4.3 and 4.4) assuming fcc packing of the atoms within the nanoparticles. The size-dependence of the absorbance was obtained from the experimental data of Cottancin *et al.*[26] which gives the absorption coefficient for nanoparticles of diameters in the range of 1.5 nm to 6.7 nm (4 nanoparticle sizes), for which there is a linear relationship of the absorption coefficient and nanoparticle diameter. As shown later, the extinction coefficient, ε_m, of Ag nanoparticles can be derived using this UV-vis data, TM-AFM and EW-CRDS measurements. With knowledge of the extinction coefficient and the data of Cottancin *et al.*, the size-dependent absorbance $A(a)$ can be estimated.

With A established, the best fit to the data was found by varying k_{app}, or equivalently the dissolution rate constant per nanoparticle, k, which is defined as:

$$k = k_{app} / F \tag{4.7}$$

where Θ is the fractional coverage computed using the initial nanoparticle size and concentration, assuming that the mediator sees only the top hemisphere of the particle

$$\Theta = \frac{\pi(2a)^2}{2} N_{NP} N_A \tag{4.8}$$

4.3 Experimental Section

4.3.1 Synthesis of Ag nanoparticles and sample preparation

Citrate-stabilised Ag nanoparticles were prepared following established methods using sodium borohydrate as the reducing agent and citrate ions as the stabilising agent.[27] The size and the size distribution is highly dependent on the concentration of those compounds. The overall reaction of the Ag nanoparticle synthesis is depicted in Scheme 4.1.
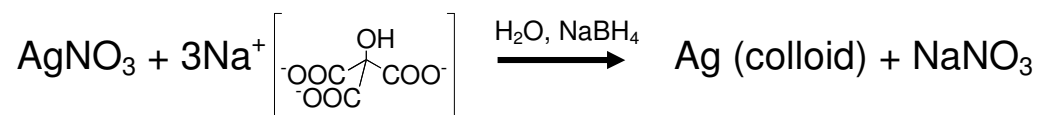
Scheme 4.1: Chemical reaction of the formation of Ag nanoparticles.

In order to obtain colloids with a narrow size distribution, it was crucial to rinse all glassware with copious amounts of purified water from a Millipore Milli-Q system (resistivity > 18 MΩ cm) prior to sample preparation. 0.6 cm^3 of 0.1 M sodium borohydride was added to 20 cm^3 of a solution containing equal concentrations (0.25 mM) of sodium citrate and Ag nitrate under strong stirring. The reaction was complete after two hours at room temperature. The stabilisation of the silver particles in solution

arises from coulombic repulsions induced by the ionised citrate species at the particle surface. However, it was found that the nanoparticles tended to aggregate over time (longer than 2 – 3 weeks).

The coverage and size distribution of nanoparticles achieved with deposition from quiescent solution onto PLL-functionalised silica surfaces was investigated by TM-AFM of PLL-coated quartz slides. The chemical structure of PLL is depicted in Figure 4.1.
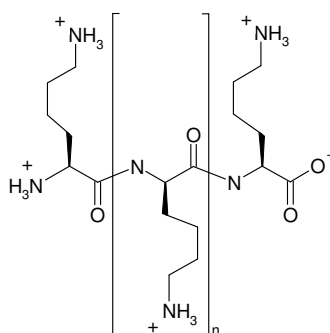
Figure 4.1: Chemical structure of poly-L-lysine at pH 7

Quartz slides were ashed in oxygen plasma for 1 min at 100 W (Emitech, K1050X) and wiped with methanol. PLL films were deposited from 1 mg cm^{-3} stock solution of the polyelectrolyte at pH 7. The quartz slides were then rinsed with ultrapure water and dried in an air flow. Ag nanoparticles were electrostatically adsorbed by exposing a PLL-modified quartz slide in a Ag nanoparticle solution for a defined time. For all TM-AFM measurements a Digital Instruments multimode AFM with a Nanoscope IIIa controller (Veeco, U.S.A.) was employed. Commercially available SPIP^{TM} software was used for statistical grain analysis in order to obtain the size and the size distribution of the Ag nanoparticles.

4.3.2 Ag nanoparticle adsorption

0.2 cm^3 of PLL (1 mg cm^{-3} in ultra pure water) was contacted for 20 min with clean fused silica prisms, leading to PLL deposition by drop coating. After deposition, the prism was rinsed with ultrapure water and dried in a flow of air. The adsorption behaviour of Ag nanoparticles, at different dilutions, on PLL-modified fused silica prisms was followed by EW-CRDS in a similar way to that described previously for other metal nanoparticles.[28] In brief, 0.2 cm^3 of Ag colloid solution was injected into the cell above the substrate and the EW-CRDS response for the adsorption process was monitored continuously. Where the modified substrate was used for subsequent dissolution studies, adsorption was stopped after a defined time (typically 2 min) by removing the remaining colloidal solution and rinsing 5 times with 1.5 cm^3 ultrapure water. By this stage, a disperse film of nanoparticles had been deposited for which the surface coverage was known. The same procedure was followed prior to all dissolution experiments. After each experiment, the prism surface was wiped several times with methanol and ashed for 1 min in an oxygen plasma at 100 W. Ashing for such short times did not affect the properties of the prism and the initial ring-down time was always re-established.

4.3.3 Chronoamperometric EW-CRDS

The oxidation and reduction potentials for $IrCl_6^{2-/3-}$ were chosen after SECM measurements involving a 25 μm diameter Pt ultramicroelectrode (UME) with an RG value (ratio of the diameter of the tip to the diameter of

the electrode itself) of 6. These experiments were carried out by Dr. Meiqin Zhang (University of Warwick) and showed that the optimal chronoamperometry experiment should be carried out with a potential step from -0.1 V to +0.4 V *vs*. Pt quasi-reference electrode. Figure 4.2 shows a CV of a 1 mM $IrCl_6^{3-}$ solution in 0.1 M KNO_3.
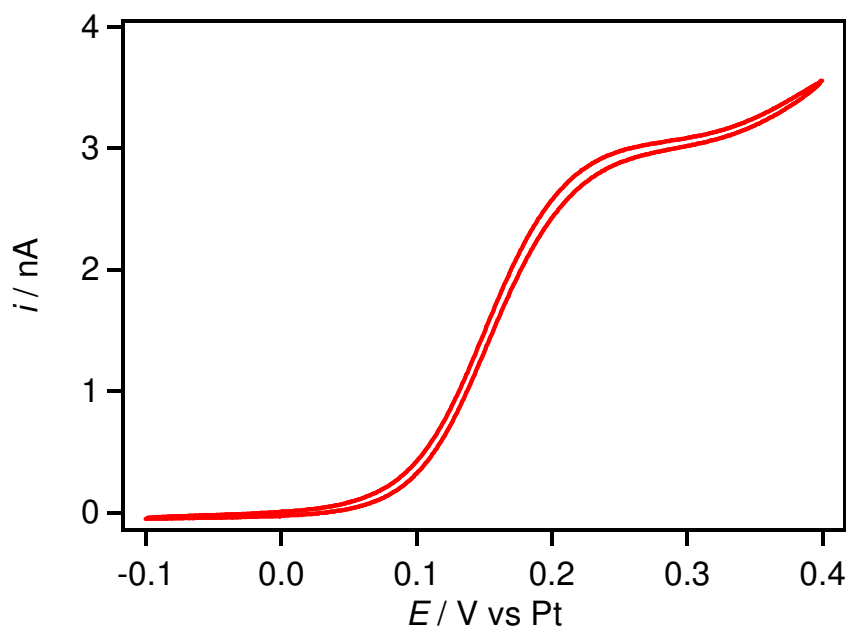
Figure 4.2: CV of a 1 mM $IrCl_6^{3-}$ solution in 0.1 M KNO_3 using a 25 µm diameter Pt UME. The scan rate was 20 mV s^{-1}.

As displayed in Figure 4.3a, the working electrode (2.0-mm-diameter circular platinum electrode with an overall diameter, including insulation, of 6.35 mm) was placed over the region of the prism co-incident with the evanescent field using a 3-axis micropositioner in such a way as to create a thin-layer electrochemical cell. The distance between the working electrode and the prism surface was chosen to be 200 µm − well outside the evanescent field − and the electrode itself did not affect the EW-CRDS signal. Two Pt wires acted as counter and quasi-reference electrodes,

respectively, with all potentials applied with respect to the latter. Measurements were made with a homebuilt potentiostat controlled by a National Instruments card (NI PCI-6221) for potential control and data acquisition. The dissolution of the nanoparticles was induced by oxidizing 1 mM or 0.1 mM $IrCl_6^{3-}$ in 0.1 M KNO_3 supporting electrolyte. The potential was stepped from -0.1 V to +0.4 V for a defined time during which the oxidation of $IrCl_6^{3-}$ to $IrCl_6^{2-}$ was diffusion-controlled. The potential was then returned to -0.1 V where $IrCl_6^{2-}$ was reduced back to $IrCl_6^{3-}$.
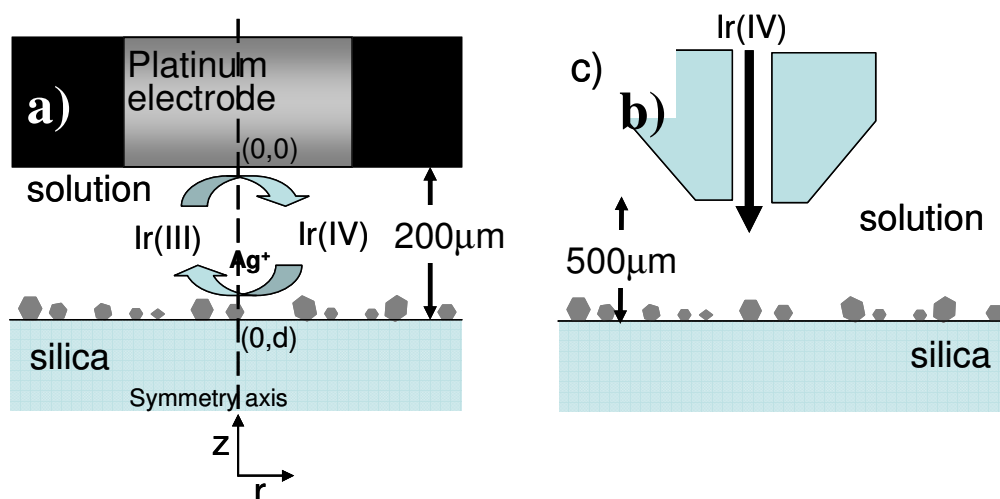
Figure 4.3: a) $IrCl_6^{2-}$ is electrogenerated from $IrCl_6^{3-}$ in an axisymmetric thin layer electrochemical cell, whilst in b) $IrCl_6^{2-}$ solution is injected in close proximity to the surface *via* a 300 µm internal diameter micropipette.

4.3.4 Flow EW-CRDS

Micropipettes with a typical internal diameter of 300 µm were produced by pulling a 2-mm-o.d. borosilicate glass capillary (Harvard Apparatus, UK) using a PB7 Narishighe micropipette puller and cutting the tapered end

with a sharp scalpel. The resulting nozzle was polished using a home-built polishing wheel with a 0.1-µm diamond polishing pad (Buehler, USA). Figure 4.4 shows an optical micrograph of the top of a typical nozzle.
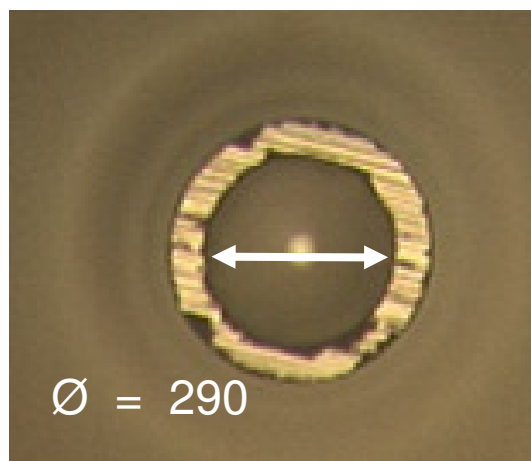
Figure 4.4: Optical micrograph of a typical borosilicate glass capillary (end on view).

The micropipette was placed over the region of the evanescent field using a 3-axis micropositioner at a distance of *ca.* 500 µm from the prism surface (Figure 4.3b). Flow of the solution of K_2IrCl_6 at concentrations between 1 µM and 5 µM at a constant rate was achieved with a syringe pump (KDS100, KD Scientific) equipped with a 10 cm^3 glass syringe (Hamilton). The system delivered flow rates in the range of 0.22 – 35.1 µL s^{-1}. Typical flow rates used were between 1.7 and 33.3 µL s^{-1}. All solutions were freshly prepared immediately prior to experiments.

4.4 Results and discussion

4.4.1 TM-AFM

Figure 4.5 shows a typical 1 μm x 1 μm TM-AFM height image of Ag nanoparticles on a PLL modified fused silica slide following adsorption from stock solution. A clear submonolayer coverage of Ag nanoparticles is evident, from which the size, the size distribution and the coverage of the nanoparticles can be estimated. The average size of the Ag nanoparticles was found to be 7.6 (± 2.6) nm and in this case the coverage was 60 ± 17 nanoparticles per μm^{-2}. As shown below, there was excellent agreement between surface coverages measured by TM-AFM and EW-CRDS.
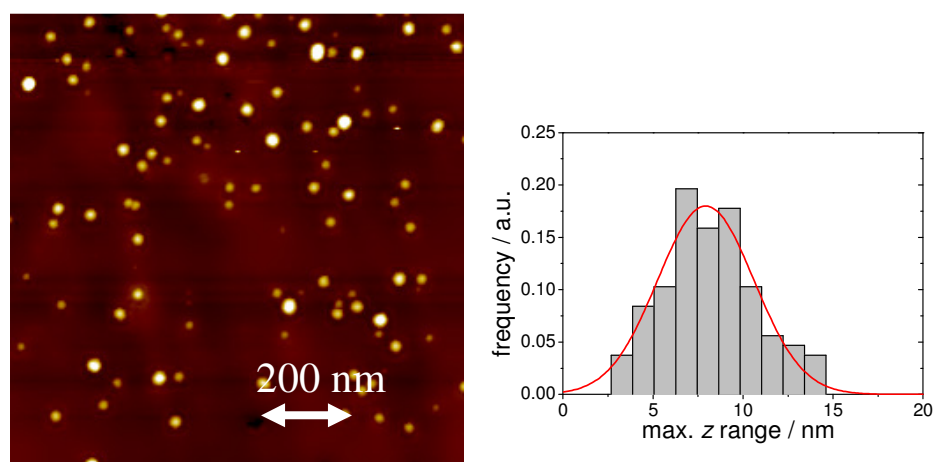
Figure 4.5: Top: Representative 1 μm x 1 μm tapping mode AFM image of Ag nanoparticles on PLL modified quartz following adsorption for 2 min. Bottom: Statistical analysis of particle size from which a mean particle size of 7.6 (± 2.6) nm was obtained from several images.

4.4.2 Ag nanoparticle adsorption

The concentration of Ag nanoparticles in solution obtained from the synthesis can be estimated assuming that all Ag^+ ions present in the solution reacted to Ag^0. Using eq. 4.6, the nanoparticle concentration is given by[29]

$$c_{NP} = \frac{c_{Ag^+}}{\sum f_i \frac{N_A}{M} \rho V_{NP}} \qquad (4.9)$$

where c_{Ag+} is the initial concentration of Ag^+ (0.25 mM), f_i is the frequency of nanoparticles with radius, a_i, as obtained by TM-AFM and V_{NP} is the volume of nanoparticles with radius a_i. The distribution is normalised so that it satisfies

$$\sum_{i=1}^{L} f_i = 1 \qquad (4.10)$$

In this work, the resulting concentration was calculated to be 11.3 nmol dm^{-3}. With this information, the extinction coefficient of the Ag nanoparticle solution can be calculated by plotting the relative peak absorbance of different dilutions from UV-vis spectroscopy as a function of concentration (see Figure 4.6). As shown in the inset of Figure 4.6, the relative absorption values show a good linear dependence on the concentration. The calculated molar extinction coefficient for Ag nanoparticles was $\varepsilon_m = 2.88 \times 10^{11}$ cm^2 mol^{-1}, which is in good agreement with previous reports.[29] UV-vis spectroscopy is also a convenient way to monitor the growth and determine the quality of the nanoparticles. The

spectrum of a dilute Ag nanoparticle solution shows a well-defined absorption peak at around 400 nm which corresponds to the localised surface plasmon resonance band of silver. These measurements can also be carried out to monitor the growth of the nanoparticles over time. The spectra were recorded between 230 nm to 800 nm with a resolution of 1 nm. The fact that the plasmon peak is relatively narrow suggests a constant size with a fairly narrow size distribution.
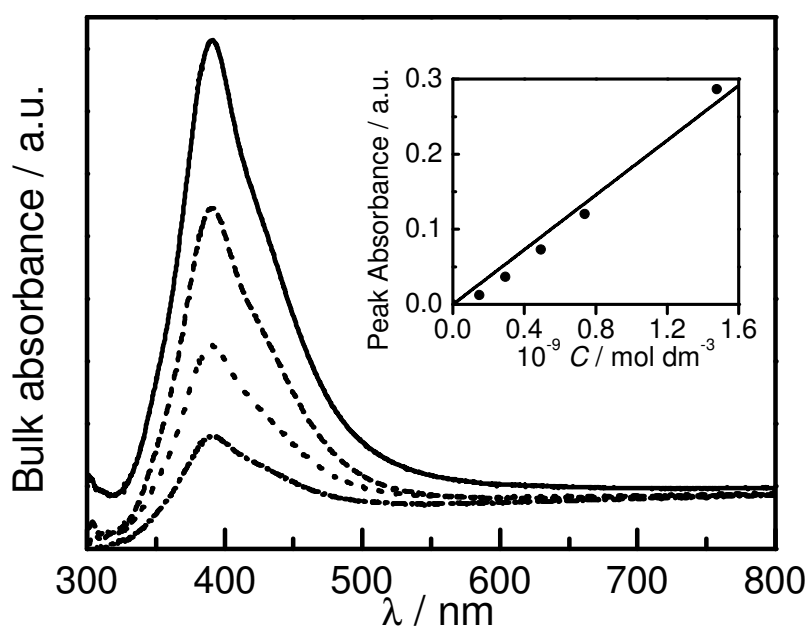
Figure 4.6: Bulk UV-visible absorbance spectra for different dilutions of Ag nanoparticles in water. The large band at 400 nm corresponds to the localised surface plasmon resonance band of Ag. Inset: Peak absorbance *versus* colloid concentration.

The time-dependent surface concentration resulting from adsorption studies could be calculated using absorbance values measured from the EW-CRDS data, $A(t)$, and the extinction coefficient:

$$N_{\text{NP}}(t) = \frac{A(t)}{\varepsilon_m}.$$ (4.11)

This equation is valid only if there is negligible absorbance from the bulk solution within the evanescent field. Our simulations support this assumption: even assuming a 500 μm effective thickness, simulations show that the bulk absorbance never exceeds 3% of the interfacial absorbance for any of the results reported here.

For a typical absorbance value of 0.002 (at 405 nm), the corresponding calculated surface coverage was 42 μm^{-2} which is similar to the value of 60 ± 17 nanoparticles per μm^2 obtained by TM-AFM measurements for Ag nanoparticle adsorption from the stock solution. This represents an effective surface coverage of *ca.* 0.2 %.

Figure 4.7 shows the time-dependence of the interfacial absorbance as Ag nanoparticles adsorb irreversibly on the PLL-modified fused silica. As the figure shows, the experimental absorbance data fit satisfactorily to a simple square root dependence ($t^{1/2}$) which is expected for diffusion-controlled adsorption.[30] Since the adsorption process is completely diffusion-controlled, the diffusion coefficient of Ag nanoparticles, D_{NP}, can be calculated[31] using

$$A(t) = 2\varepsilon c_{NP}\pi^{-1/2}D_{NP}^{1/2}t^{1/2} \tag{4.12}$$

where $A(t)$ represents the time-dependent optical absorption, which relates to the amount adsorbed on the surface. The diffusion coefficient was calculated to be (1.92 ± 0.22) x 10^{-6} cm^2 s^{-1} using all the sets of data in Figure 4.7.
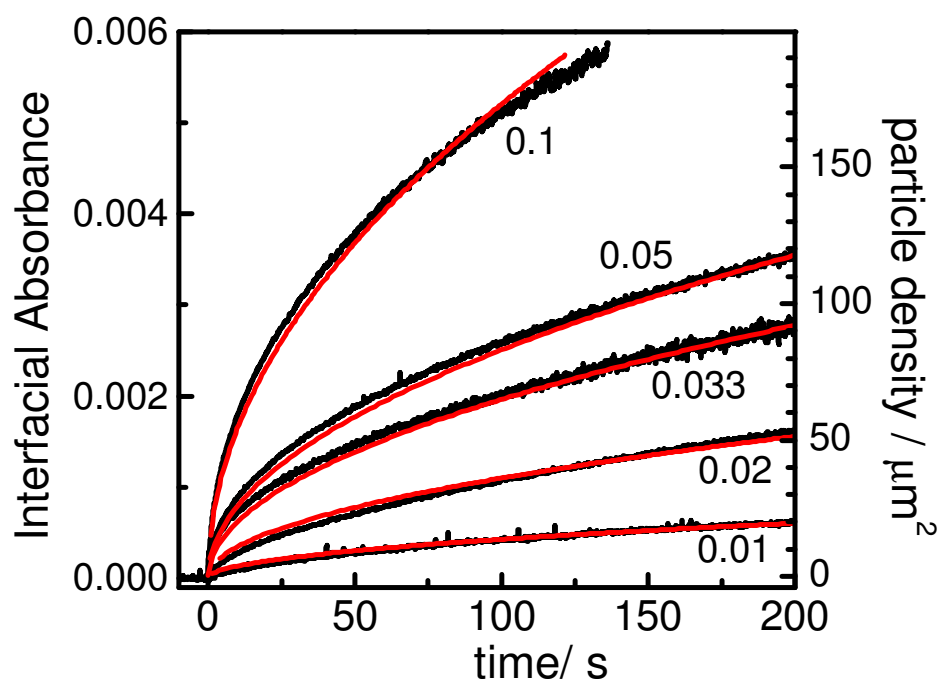
Figure 4.7: Interfacial absorbance transients for the adsorption of several dilutions of nanoparticles on PLL modified fused silica. The dilutions are: 1:10, 1:20, 1:30, 1:50 and 1:100. The red lines denote fits assuming diffusion-controlled ($\propto t^{1/2}$) adsorption kinetics.

The fact that the adsorption of nanoparticles can be followed from a solution that contains such a low concentration of Ag nanoparticles is testament to the sensitivity of EW-CRDS, coupled with the strength of the localised surface plasmon peak of Ag nanoparticles, which enables the detection of very low coverages of nanoparticles. As shown in Figure 4.7, a dilution of the stock solution of 1:100 (i.e. 0.18 nmol dm^{-3}) gives rise to an absorbance value of 0.00045 after 120 s, which corresponds to only 18 particles per μm^2. For the dissolution experiments which follow, surfaces were prepared from either the 1:20 or the 1:100 dilutions. The adsorption was typically stopped after *ca.* 120 s. The corresponding

absorbance value of the transient at this time was used to determine the surface coverage of Ag nanoparticles.

4.4.3 Electrochemical dissolution

The electrochemical dissolution of Ag nanoparticles can be summarised by the following redox reaction:

$$IrCl_6^{2-} + Ag(0) \rightarrow IrCl_6^{3-} + Ag(I) \tag{4.13}$$

In these experiments, $IrCl_6^{2-}$ was electrogenerated from $IrCl_6^{3-}$ at an electrode situated *ca.* 200 µm above the prism surface. The electrogeneration process occurred for a defined time before the potential of the working electrode was switched back to a value which reduced $IrCl_6^{2-}$ to $IrCl_6^{3-}$. The current-time behaviour is shown in figure 4.8.
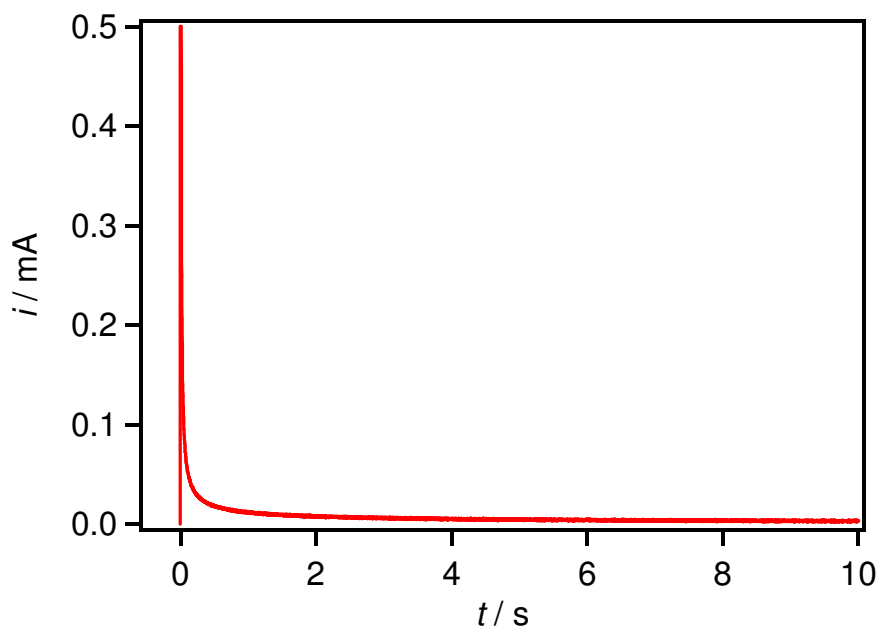
Figure 4.8: Current – time transient for a 10 s potential step experiment in a thin layer cell experiment for the oxidation of 0.1 mM $IrCl_6^{3-}$ to $IrCl_6^{2-}$ in 0.1 M KNO_3 using a 2 mm diameter Pt disc electrode. The potential was stepped from -0.1 V to +0.4 V *vs.* Pt.

Figure 4.9a and b show typical experimental EW-CRDS transients for the electrochemical dissolution process for two different step times of 5 s (a) and 10 s (b), together with simulated transients using the model outlined earlier. The dissolution rate constant per nanoparticle, k, was calculated to be 2.7 x 10^{-3} cm s^{-1} for the 5 s step and 2.8 x 10^{-3} cm s^{-1} for the 10 s step.
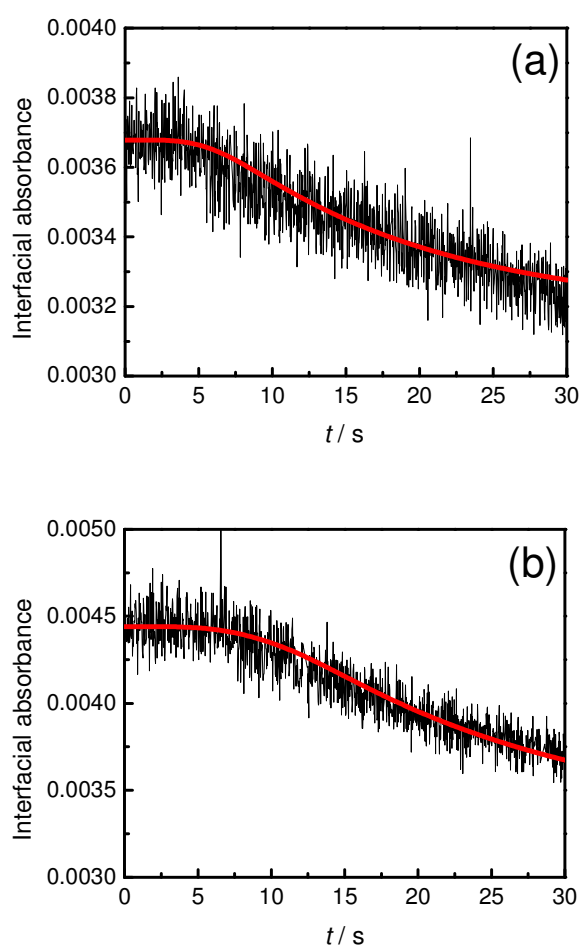
Figure 4.9: Interfacial absorbance transients for the electrochemical dissolution of Ag nanoparticles using 1 mM $IrCl_6^{3-}$ oxidised for 2 s (a) and 10 s (b) at the electrode. The red lines indicate fits obtained using the model described in the text from which rate constants for the dissolution of 2.7 x 10^{-3} cm s^{-1} for the 5 s potential step and 2.8 x 10^{-3} cm s^{-1} for the 10 s potential step were extracted.

After an initial delay period of a few seconds, during which $IrCl_6^{2-}$ diffuses from the electrode towards the prism, the interfacial absorbance slowly decreases with time. This can be attributed to the dissolution of Ag nanoparticles within the evanescent field. Since the plasmon resonance of the Ag nanoparticles is the main contribution to the extinction at 405 nm, the decrease in the absorbance due to the dissolution process will be determined by the number of particles within the evanescent field as well as their size.
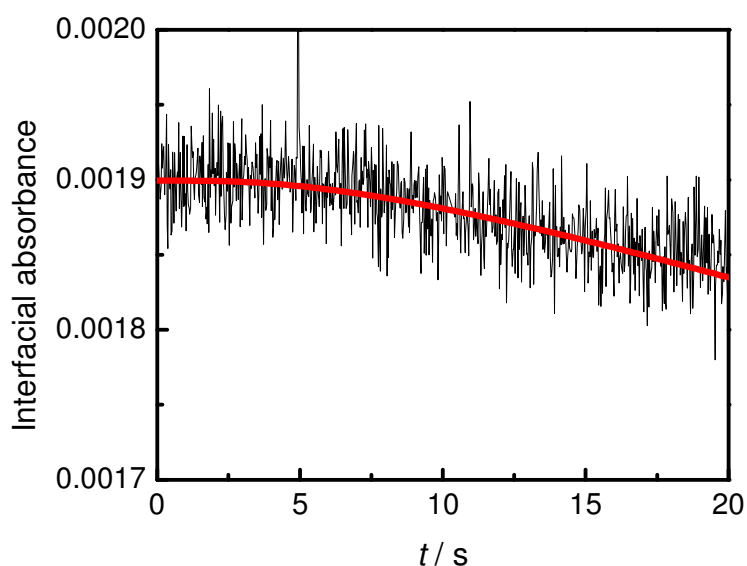
Figure 4.10: Interfacial absorbance transient for the electrochemical dissolution of Ag nanoparticles using 0.1 mM $IrCl_6^{3-}$ oxidised for 600 s. The red line indicates a fit obtained using the model described in the text from which a dissolution rate constant of 2.8 x 10^{-3} cm s^{-1} was extracted.

Figure 4.10 shows the absorbance transient for a potential step time of 600 s but at a lower $IrCl_6^{3-}$ concentration of 0.1 mM. The absorbance decreases much more gradually for this low concentration which can be

explained by the fact that the dissolution process is limited with the amount of $IrCl_6^{2-}$ present in the thin layer cell. The rate constant, k, for this transient was determined to be 2.8×10^{-3} cm s^{-1}, which is in very good agreement with the rate constants obtained above. The mean rate constant for the dissolution per nanoparticle from several runs was calculated to be $(2.5 \pm 0.6) \times 10^{-3}$ cm s^{-1}.

If the potential step experiments are repeated, it was found that the drop in the absorbance occurred further. Figure 4.11 shows the EW-CRDS response of 4 subsequent potential step experiments for a $IrCl_6^{3-}$ concentrations of 1 mM. After each experiment, the electrode was raised from the surface, in order to let the surface concentration and the concentration in the thin layer cell be restored to the initial bulk value. The first 3 (a to c) involved a potential step experiments with a step time of 10 s, while the step time in the last experiment (d) was 20 s.

It is clear from figure 4.11 that one single potential step experiment is not sufficient to dissolve all Ag nanoparticles on the surface. This is reasonable, if one takes into account the small volume of the thin layer cell between the electrode and the prism surface which corresponds to 6.3×10^{-3} cm^3 (by taking into account the outer diameter of the Pt electrode). Using a 1 mM solution of $IrCl_6^{3-}$, only 6.3 nmol of $IrCl_6^{3-}$ are present in the thin layer cell. All of the $IrCl_6^{3-}$ within the thin layer cell will be converted and therefore only a certain amount of Ag can be dissolved. After the 4th step, the absorbance tends towards 0, indicating that at this point all Ag nanoparticles have been removed from the surface.
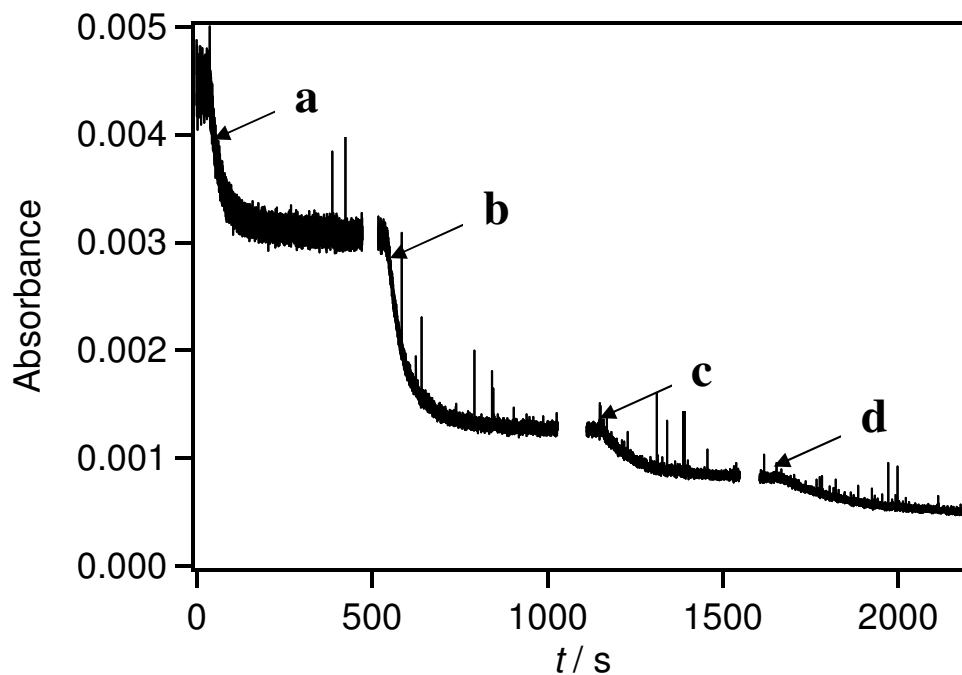
Figure 4.11: EW-CRDS absorbance transients for 4 sequenced potential step experiments (The $IrCl_6^{3-}$ concentration was 1 mM). The potential step time was a) 10 s, b) 10 s, c) 10 s, d) 20 s.

At this stage, it is necessary to provide a quantitative analysis of EW-CRDS. As described in Chapter 3, the acquisition frequency (which is limited by the DAQ card is *ca*. 2.4 kHz which corresponds to a data point separation of 0.4 ms. The data points are then averaged 100 times on the DAQ card before transfer to the computer (time resolution after averaging is 20 ms). The limiting sensitivity of the EW-CRDS instrument can be defined as the minimal possible absorption coefficient that can be detected, α_{min} which is the case, when $\tau \rightarrow \tau_0$ This can be described by

$$\alpha_{min} = \frac{1}{c_L \tau_0} \frac{\Delta \tau}{\tau_0} \qquad (4.14)$$

where $\Delta \tau$ is the minimum detectable change (standard deviation) in the ring-down time. The sensitivity can be improved by minimising the relative

103

error of the rind-down time measurements (ration $\Delta\tau$ to τ_0). This can be achieved by averaging the experimental data but this way, some temporal resolution is lost. By calculating the standard deviation for different acquisition times, the minimum absorbance can be calculated using eq. 1.3. If we consider a measurement time period of 1 s, the standard deviation for the raw data leads to a minimum detectable absorbance of 3.1×10^{-6}. If the data is averaged further (10 times which corresponds to a time resolution of 200 ms) and interpolated to obtain the same amount of data points, the minimum detectable absorbance is 0.7×10^{-6}.

4.4.4 Convective Dissolution

An alternative strategy to investigate the dissolution behaviour of Ag nanoparticles was to introduce a micropipette close to the prism surface through which $IrCl_6^{2-}$ was directly injected onto the colloidal particles. Figure 4.12a shows the concentration dependence of the dissolution rate for a constant flow rate of 8.3 $\mu L\ s^{-1}$ in which all transients were normalised with respect to their initial absorbance:

$$A_{rel} = \frac{A_{exp}(t)}{A(t=0)} \tag{4.15}$$

where A_{exp} is the absorbance transient and A_{ini} the interfacial absorbance of Ag nanoparticles before dissolution begins. The sensitivity of this approach, with a constant supply of $IrCl_6^{2-}$ even at very low concentrations of $IrCl_6^{2-}$ is clear. Experiments at higher $IrCl_6^{2-}$ concentrations demonstrated complete dissolution of the nanoparticles.

Studies at different flow rates of $IrCl_6^{2-}$ solution were also carried out and the results are displayed in Figure 4.12b. Higher flow rates lead to faster dissolution, indicating at least partial control of the kinetics by mass transport of $IrCl_6^{2-}$ to the surface. For future studies, a finite element model, building on to earlier investigations[32] could be established in order to describe this type of hydrodynamic system more rigorously.
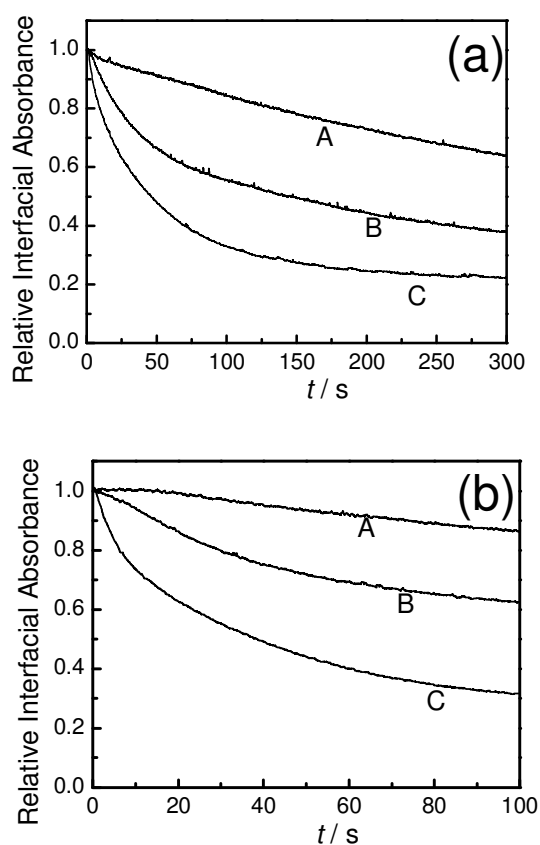
Figure 4.12: (a): Interfacial absorbance transients showing the dissolution of Ag nanoparticles using the micropipette setup with $IrCl_6^{2-}$ solution concentrations of A) 0.1 µM, B) 0.5 µM, C) 1 µM. A constant flow of $IrCl_6^{2-}$, 16.6 µL s^{-1}, was used for all measurements. (b): Dissolution of Ag nanoparticles using the micropipette setup with 1µM $IrCl_6^{2-}$ solution flow rates of A) 1.7 µL s^{-1}, B) 8.3 µL s^{-1}, C) 33.3 µL s^{-1}.

4.5 Conclusions

The time-dependent adsorption of Ag nanoparticles on PLL-modified silica and the corresponding surface coverage has been measured accurately using EW-CRDS. This technique has proven very useful as a detection tool for very low surface concentrations of Ag nanoparticles (typically 20-60 particles per μm^2). Additionally, EW-CRDS has been applied successfully to study the chemical kinetics of nanoparticle oxidative dissolution. This sensitive technique has been coupled with two complementary approaches to dissolve immobilised colloidal particles on functionalised surfaces: electrochemical dissolution via a redox mediator; and convective dissolution using a microcapillary setup to deliver the oxidant. The heterogeneous rate constant for dissolution was established as 2.8×10^{-3} cm s^{-1}. These measurements illustrate the ability of EW-CRDS to obtain kinetic information; especially on inert supporting surfaces such as silica or polymer-modified silica which are traditionally challenging to study. The combination of EW-CRDS with both chronoamperometric and flow methods shows that the dissolution process can be monitored even with very low fluxes and low concentrations of reagents, making both approaches excellent tools for potential sensing applications.

4.6 References

(1)   Bonnemann, H.; Richards, R. M. *Eur. J. Inorg. Chem.* **2001**, 2455-2480.

(2)   Gittins, D. I.; Bethell, D.; Schiffrin, D. J.; Nichols, R. J. *Nature* **2000**, *408*, 67-69.

(3)   Shipway, A. N.; Katz, E.; Willner, I. *ChemPhysChem* **2000**, *1*, 18-52.

(4)   Bauer, G.; Pittner, F.; Schalkhammer, T. *Mikrochim. Acta* **1999**, *131*, 107-114.

(5)   Habicht, W.; Behrens, S.; Wu, J.; Unger, E.; Dinjus, E. *Surf. Interface Anal.* **2004**, *36*, 720-723.

(6)   Kohut, A.; Voronov, A.; Peukert, W. *Part. Part. Syst. Char.* **2006**, *22*, 329-335.

(7)   Lu, H. C.; Yi, G. S.; Zhao, S. Y.; Chen, D. P.; Guo, L. H.; Cheng, J. *J. Mater. Chem.* **2004**, *14*, 1336-1341.

(8)   Maxwell, D. J.; Taylor, J. R.; Nie, S. M. *J. Am. Chem. Soc.* **2002**, *124*, 9606-9612.

(9)   Lee, J. S.; Lytton-Jean, A. K. R.; Hurst, S. J.; Mirkin, C. A. *Nano Lett.* **2007**, *7*, 2112-2115.

(10)   Liu, T.; Zhong, J.; Gan, X.; Fan, C. H.; Li, G. X.; Matsuda, N. *ChemPhysChem* **2003**, *4*, 1364-1366.

(11)   Chen, Y. C.; Young, R. J.; Macpherson, J. V.; Wilson, N. R. *J. Phys. Chem. C* **2007**, *111*, 16167-16173.

(12)   Li, X. L.; Xu, W. Q.; Zhang, J. H.; Jia, H. Y.; Yang, B.; Zhao, B.; Li, B. F.; Ozaki, Y. *Langmuir* **2004**, *20*, 1298-1304.

(13)   Doering, W. E.; Nie, S. M. *J. Phys. Chem. B* **2002**, *106*, 311-317.

(14)   Macpherson, J. V.; Slevin, C. J.; Unwin, P. R. *J. Chem. Soc., Faraday Trans.* **1996**, *92*, 3799-3805.

(15)   Meulenkamp, E. A. *J. Phys. Chem. B* **1998**, *102*, 7764-7769.

(16)   Rimer, J. D.; Trofymluk, O.; Navrotsky, A.; Lobo, R. F.; Vlachos, D. G. *Chem. Mater.* **2007**, *19*, 4189-4197.

(17)   Shi, H. Z.; Bi, H. J.; Yao, B. D.; Zhang, L. D. *Appl. Surf. Sci.* **2000**, *161*, 276-278.

(18)   Pal, T.; Sau, T. K.; Jana, N. R. *Langmuir* **1997**, *13*, 1481-1485.

(19)   Chen, S. H.; Akai, T.; Kadono, K.; Yazawa, T. *Appl. Phys. Lett.* **2001**, *79*, 3687-3689.

(20)   Jiang, X. W.; Qiu, J. R.; Zeng, H. D.; Zhu, C. S.; Hirao, K. *Chem. Phys. Lett.* **2004**, *391*, 91-94.

(21)   Carvalho, I. C. S.; Mezzapesa, F. P.; Kazansk, P. G.; DepariS, O.; Kawazu, M.; Sakaguchi, K. *Mater. Sci. Eng., C* **2007**, *27*, 1313-1316.

(22)   Podlipensky, A.; Abdolvand, A.; Seifert, G.; Graener, H.; Deparis, O.; Kazansky, P. G. *J. Phys. Chem. B* **2004**, *108*, 17699-17702.

(23)   Zhang, M. Q.; Wittstock, G.; Shao, Y. H.; Girault, H. H. *Anal. Chem.* **2007**, *79*, 4833-4839.

(24)   Zhang, M.; Becue, A.; Prudent, M.; Champod, C.; Girault, H. H. *Chem. Commun.* **2007**, 3948-3950.

(25)   Rodriguez-Sanchez, M. L.; Rodriguez, M. J.; Blanco, M. C.; Rivas, J.; Lopez-Quintela, M. A. *J. Phys. Chem. B* **2005**, *109*, 1183-1191.

(26)   Cottancin, E.; Celep, G.; Lerme, J.; Pellarin, M.; Huntzinger, J. R.; Vialle, J. L.; Broyer, M. *Theor. Chem. Acc.* **2006**, *116*, 514-523.

(27)   Schnippering, M.; Carrara, M.; Foelske, A.; Kotz, R.; Fermin, D. J. *Phys. Chem. Chem. Phys.* **2007**, *9*, 725-730.

(28)   Mazurenka, M.; Hamilton, S. M.; Unwin, P. R.; Mackenzie, S. R. *J. Phys. Chem. C* **2008**, *112*, 6462-6468.

(29)   Liu, X. O.; Atwater, M.; Wang, J. H.; Huo, Q. *Colloids Surf., B* **2007**, *58*, 3-7.

(30)   Crank, J. *The Mathematics of Diffusion*; Oxford University Press: Oxford, 1975.

(31)   Adamczyk, Z. *J. Colloid Interface Sci.* **2000**, *229*, 477-489.

(32)   Bitziou, E.; Rudd, N. C.; Edwards, M. A.; Unwin, P. R. *Anal. Chem.* **2006**, *78*, 1435-1443.

5 Real Time Monitoring of Polyaniline Nanoparticle Formation on Surfaces

This chapter describes the formation of polyaniline (PAni) nanoparticles on silica surfaces by monitoring the change in the optical absorbance using EW-CRDS. Aniline hydrochloride in aqueous solution at different concentrations was oxidatively polymerised using sodium persulfite. The process was found to involve the nucleation and growth of polymer nanoparticles, whose size and coverages were measured using TM-AFM. The formation of PAni was confirmed by replacing the silica surface with indium doped tin oxide (ITO) electrodes, and subsequently running CV experiments on the material deposited, which yielded the characteristic electrochemical response. The number of active groups (monomers) per polymer particle was estimated using the peak current of the CVs, with knowledge of the nanoparticle surface coverage from TM-AFM analysis. The quantity of material in each particle was consistent with TM-AFM height data, assuming hemispherical particle morphology. The polymerization process was found to be governed by surface-controlled kinetics, from a fixed number of particle sites of 35 ($\pm$ 5) μm^{-2}. The reaction was first-order in aniline, with a rate constant for monomer addition of 0.7 ($\pm$ 0.4) x 10^{-7} cm s^{-1} in the limit of large particle size. For

smaller nanoparticles, however, at the early stage of polymerization ($r < 2$ nm), the polymerization rate constant appeared to be size-dependent and to increase with decreasing nanoparticle radius (assuming a hemispherical geometry). This could also be due to a change in the morphology of the nanoparticles at the very shortest times, but may indicate size-dependent polymerization kinetics.

5.1 Introduction

PAni is among the most studied conducting polymers[1-3] and one of the oldest known synthetic organic polymers.[4] Numerous studies have been carried out to understand the fundamental properties of this polymer, such as its electronic[5] and spectroscopic[6-8] characteristics. PAni is of great interest for many technological applications, especially if synthesised in the form of thin films and nanofibres which can be used as electrochromic materials[9] or in LEDs,[10-12] biosensors,[13-15] chemical sensors,[16-21] battery electrodes[22, 23] and as supports for electrocatalysts.[24, 25] The different redox states of PAni[26] and their underlying chemical structures,[27] as well as synthesis strategies are summarised in a number of reviews.[2, 3, 28]

PAni is typically synthesised by one of two principal methods; either electrochemically via electrodeposition to generate thin films[29-31] and nanowires,[32] or by chemical oxidation.[33, 34] In the latter case, the polymer is prepared in solution and then filtered and dried as a powder. This can subsequently be deposited onto a substrate in various ways. PAni films and conductive polymer films, in general, can be produced by spin coating,[35] layer-by-layer assembly,[36] and the Langmuir-Blodgett[35, 37, 38] and

Langmuir-Schaefer techniques.[39, 40] It is also possible to synthesise nanocomposites of PAni such as PAni nanoparticles,[3] nanofibres,[41-44] nanotubes,[3, 45, 46] nanorods[47] and microspheres.[3, 48] Nanostructured PAni has a high surface to mass ratio, and potentially unique electrical properties, and is thus of interest for possible applications in fuel cells and sensors.

A particularly interesting method for preparing films of controllable thickness is the *in situ* adsorption polymerisation technique developed by MacDiarmid *et al.*[2] where a sample to be coated is immersed into the solution during the polymerisation process.[49-51] This method involves an induction period for the aniline oxidation, typically in the first few minutes, followed by an exothermic oxidative polymerisation process in which well defined polymer films can be produced.[50, 52] It has been reported that, under acidic conditions, this surface polymerisation occurs in the early stage of the reaction, whereby aniline cation radicals produced during the induction period are adsorbed on the glass surface.[50] PAni chains grow from these primary nucleation centres, even under conditions in which no bulk polymerisation occurs.

Sapurina *et al.* have investigated the adsorption polymerisation of aniline by monitoring the temperature change as a function of reaction time.[50] To confirm that the oxidative polymerisation of aniline preceded the bulk polymerisation, Fedorova *et al.* followed the polymerisation in the presence of silica gel which exhibits a high surface area.[53] It was found that polymerisation on silica gel was faster and occurred much earlier than the bulk polymerisation. The quartz crystal microbalance (QCM) technique has

also been used to follow the kinetics of PAni film formation on a gold substrate.[54] A rather long induction period was found at low concentrations and the polymerisation process appeared to have a first-order dependence on aniline concentration. This technique considerably improved the detection limit of PAni surface coverage in the induction period compared to conventional absorption spectroscopy, but is still somewhat limited if one seeks to follow the initial polymerisation at the very early stage and understand the nature of the reaction.

In this chapter, the dynamics of PAni formation at silica surfaces at an early stage of the polymerisation process is reported. By employing *in-situ* high repetition rate EW-CRDS and *ex-situ* tapping mode AFM (TM-AFM), we show for the first time that the adsorption polymerisation of PAni involves the formation and growth of PAni nanoparticles. This is an interesting observation because, as highlighted above, the formation of PAni nanostructures is of considerable interest and stopping the adsorption polymerisation process at an early stage allows a defined density of relatively monodisperse nanoparticles to be produced on a substrate. Furthermore, by developing a basic model for PAni nanoparticle growth, taking into account AFM and EW-CRDS data, it is possible to quantify the polymerisation kinetics.

5.2 Experimental Section

5.2.1 Tapping mode atomic force microscopy

The polymerisation of aniline was carried out on polished single crystal quartz slides (Hoffmann Materials U.S.A.), essentially analogous in terms of surface chemistry to the silica prisms used for EW-CRDS measurements. TM-AFM images were recorded as described in Chapter 2.

5.2.2 Electrochemical measurements

CVs were recorded using an electrochemical analyzer (CH Instruments, model CHI730 A). Experiments were carried out using a three-electrode configuration consisting of a saturated calomel reference electrode (SCE), a platinum wire counter electrode and a PAni modified indium doped tin oxide (ITO, resistance 4 – 8 Ω, Delta Tech. Ltd.) slide as working electrode. The ITO slides were prepared by sequential cleaning with acetone, ethanol and Milli-Q water in an ultrasonic bath before immersing them into a solution containing 0.2 M aniline hydrochloride and 0.06 M sodium persulfate. The slides were removed after a defined time (typically 6 min) and rinsed with Milli-Q water. The sample was then connected as the working electrode in an electrochemical cell containing 10 mL 0.1 M HCl. The potential range was chosen to be from -0.2 to 1.0 V vs. SCE and measurements were carried out at a range of scan rates (typically from 0.01 V s^{-1} to 0.2 V s^{-1}).

5.3 Results and discussion

5.3.1 TM-AFM

In order to obtain statistical data about the size and the coverage of PAni nanoparticles, TM-AFM measurements were carried out for different polymerisation times. SPIP software was used to obtain statistical information about the coverage, size and size distribution of the PAni nanoparticles. As an example, Figure 5.1A shows a 2 μm x 2 μm scan for PAni nanoparticle which were let to polymerise for 3 min from a 0.2 M aniline solution. It can be seen, that the nanoparticles formed are uniformly distributed and aggregation on the surface is negligible. The histogram (Figure 5.1B) shows a fairly narrow size distribution of the polymer nanoparticles. The deduced size of the nanoparticles was 5.6 (± 2.4) nm for this particular polymerisation time.
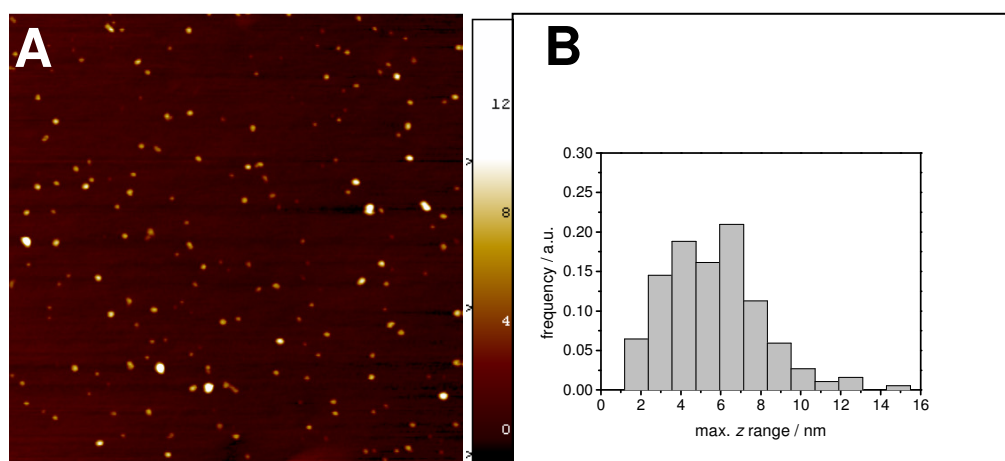
Figure 5.1: A) 2 μm x 2 μm *ex situ* TM-AFM image of PAni nanoparticles polymerised for 3 min from a 0.2 M monomer concentration on a quartz sample. The *z* range was 16.5 nm B) Statistical analysis of PAni nanoparticle size from which a mean particle size of 5.8 (± 1.3) nm was obtained.

Figure 5.2 shows the topographic (A), amplitude (B) and phase (C) image of a 1 µm x 1 µm TM-AFM scan as well a line scan image (D). The polymerisation time for these images was 5 min also using a monomer concentration of 0.2 M. It can be seen that the shape of the particles, although distorted by the AFM tip, can reasonably be approximated by a hemisphere.
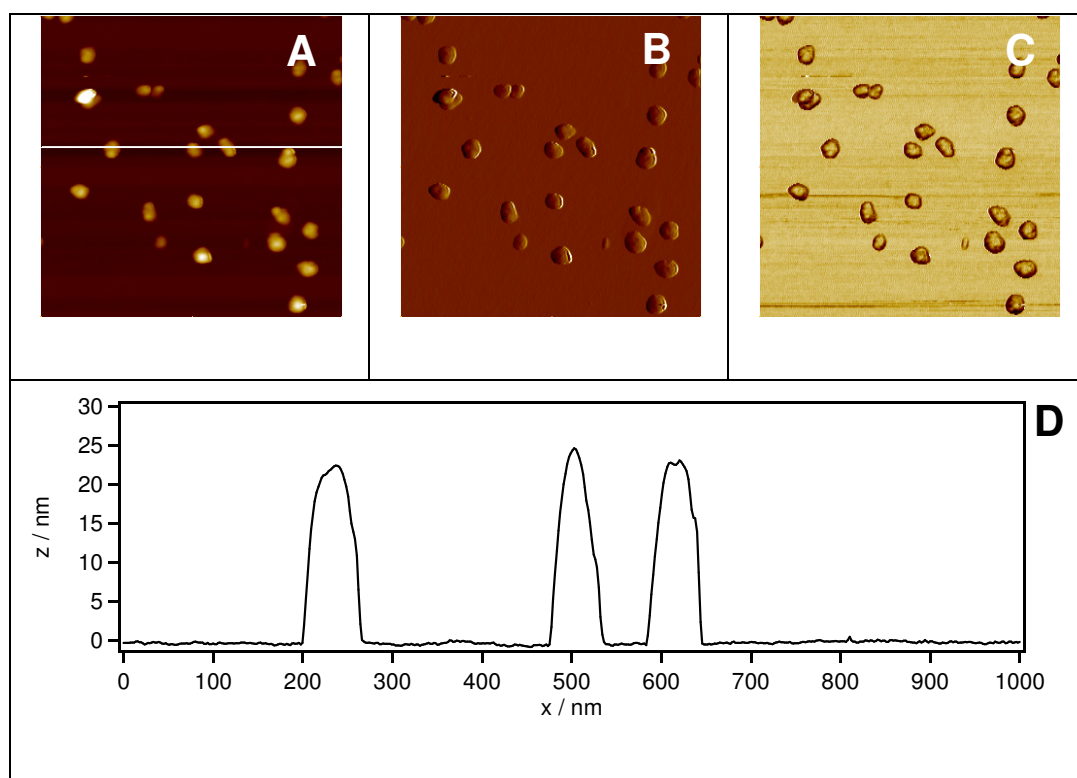
Figure 5.2: 1 µm x 1 µm *ex situ* TM-AFM (A), amplitude (B) and phase (C) image of PAni nanoparticles polymerised for 5 min from a 0.2 M monomer concentration on a quartz sample. The *z* range in A was 52 nm. The line scan in A is displayed in D.

Figure 5.3 shows several 1 µm x 1 µm TM-AFM images measured on quartz samples taken from the polymerisation reaction at 1 minute intervals over the time range of 2 minutes to 6 minutes. As the polymerisation

progresses, the polymer particles grow markedly in size with little evidence of additional nucleation.
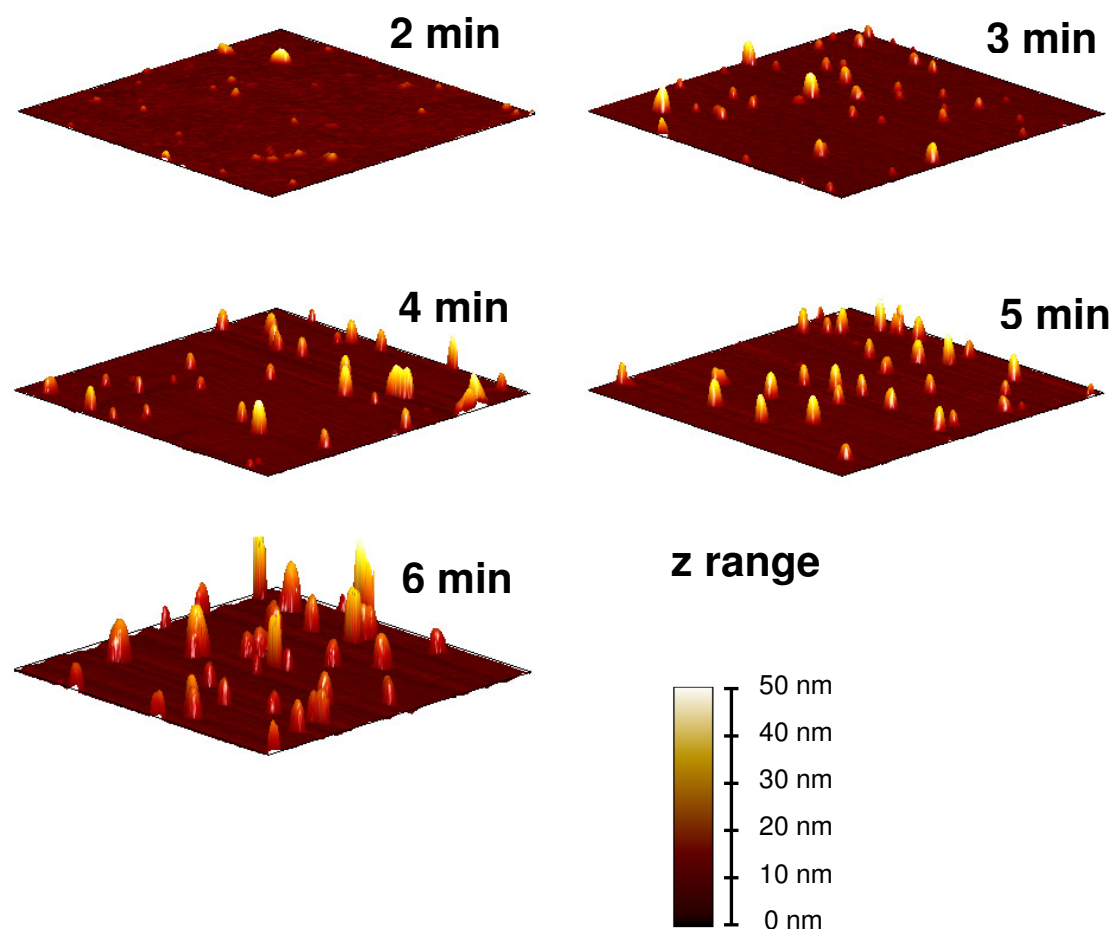
Figure 5.3: *Ex situ* TM-AFM images of PAni. The scan range of all images is 1 μm x 1 μm. The polymerisation process was stopped after different times ranging from 2 min to 6 min and several images were recorded. The aniline concentration was kept constant at 0.2 M.

The particle number density as a function of time (Figure 5.4) was obtained using commercially available software (SPIP^TM), and indicates that the number density of particles remains essentially constant at a value of

35 (± 5) μm^{-2}, from short times onwards. This suggests that nuclei are formed in an early period and that all subsequent growth occurs at these particles. The TM-AFM images were used to extract height information to permit estimates of the amount of aniline units in each particle (see below).
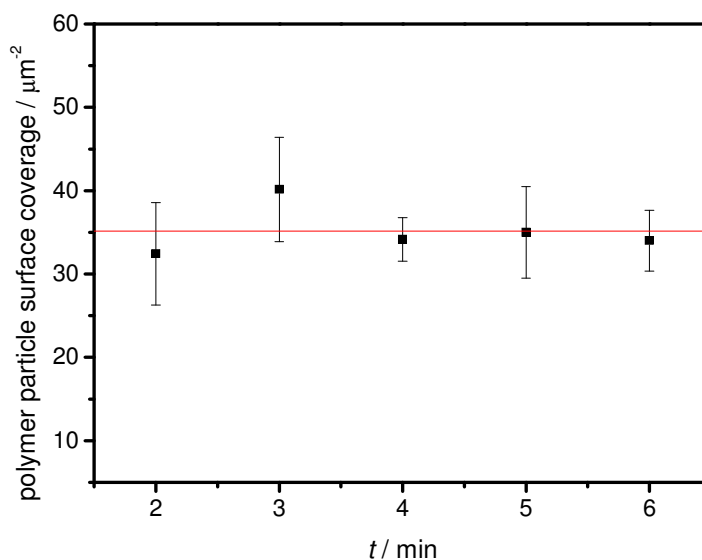
Figure 5.4: Polymer particle surface coverage as a function of the polymerisation time determined from TM-AFM.

5.3.2 Electrochemical Measurements

Figure 5.5a shows CVs recorded at different scan rates (from 0.01 to 0.2 V s^{-1}) between -0.2 V and 1.0 V vs. SCE for polymer deposited on an ITO surface after a polymerisation time of 6 minutes. There are 3 pronounced electrochemical redox pairs, corresponding to three redox states of PAni which have been described in numerous reports in the literature[55-57] and whose observation here confirm the presence of PAni on the immersed substrate after the oxidative polymerisation. The first set of redox peaks at

around 0.1 V is associated with the oxidation and reduction of the (conducting) leucoemeraldine and emeraldine states of PAni.[38] The redox pair in the middle, at 0.45 V, represents the redox reaction of overoxidation products while the third redox pair at 0.6 V corresponds to conversion of PAni from the emeraldine to the insulating pernigraniline form. The linear relation between the peak current for the anodic redox wave at 0.45 V vs. SCE, and the scan rate, shown in Figure 5.5b, is characteristic of an electroactive film rather than redox species in solution. The number of monomers (i.e. active groups), Γ^*, in mol cm^{-2}, can be estimated from[58]

$$\Gamma^* = \frac{4RTi_p}{n^2F^2\nu S} \qquad (5.1)$$

where R is the gas constant, T the temperature, i_p the peak current, n the number of electrons involved in the redox process, F the Faraday constant, ν the scan rate and S the electrode area. The number of active groups per particle can then be described by:

$$N_{\text{aniline}} = \Gamma^* N_A N_p^{-1} \qquad (5.2)$$

where N_A is Avogadro's constant and N_p is the number of particles per unit area of the substrate surface which was measured by TM-AFM. Given the (constant) coverage of 35 ($\pm$ 5) polymer particles per μm^{-2} (Figure 5.4), the number of aniline groups per polymer particle after 6 minutes was calculated to be 1.0 ($\pm$ 0.2) x 10^4. Assuming a hemispherical morphology and a typical PAni density, ρ, of 1.33 g cm^{-3},[59] this corresponds to particles of radius 8.2 ($\pm$ 0.6) nm which is in reasonable agreement with the

TM-AFM measurements at this time which gave values of radius of 8.7 (± 2.2) nm.
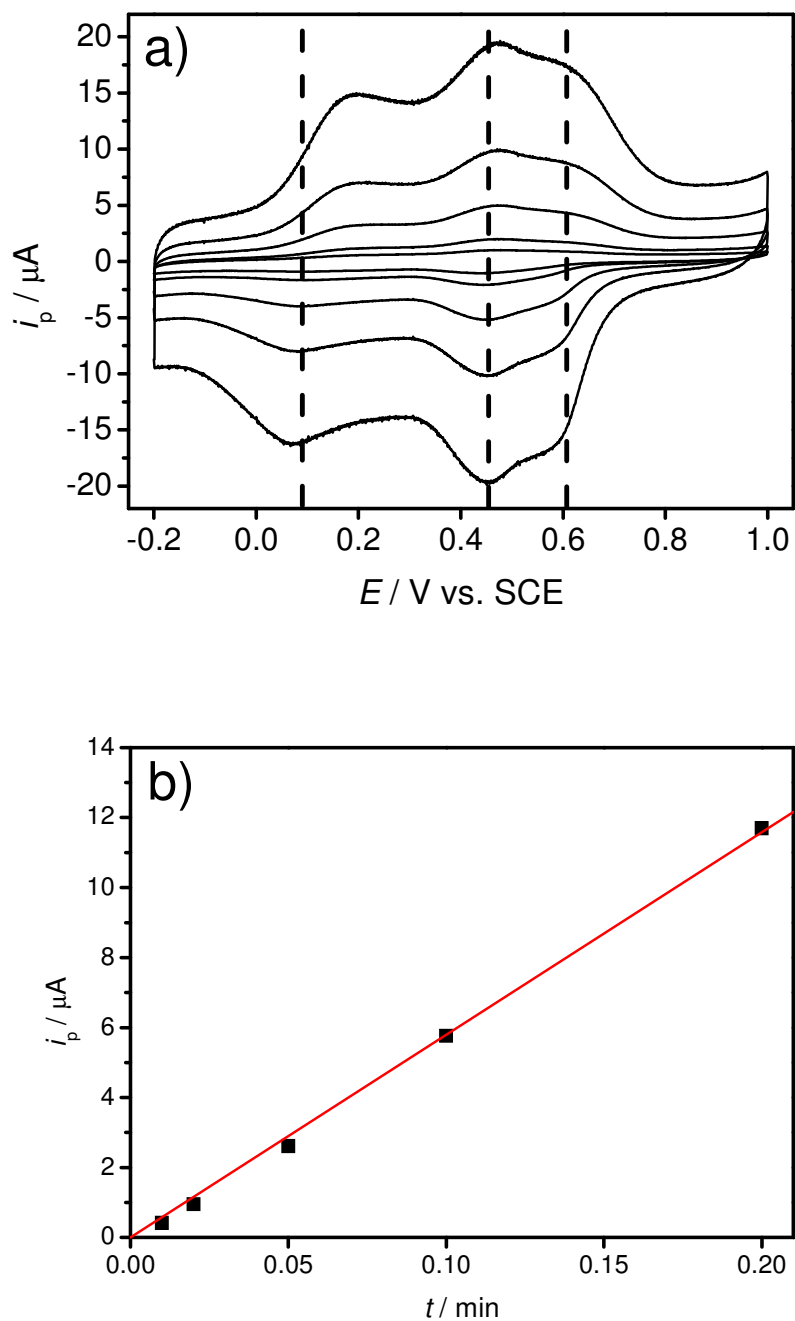
Figure 5.5: a) CVs of PAni polymerised for 6 min from a 0.2 M monomer solution onto an ITO electrode (unbiased during the polymerisation process). Voltammetric measurements

were carried out at scan rates ranging from 0.01 V s^{-1} to 0.2 V s^{-1}. b) The peak current (first anodic peak) *vs*. scan rate for the above CVs.

Since the size and the overall amount of PAni on the surface depend on the polymerisation time, the electrochemical response is higher for samples which were longer immersed in the polymerisation solution. Figure 5.6 shows a comparison between two slides on which PAni was deposited for 3 min and 5 min, respectively.
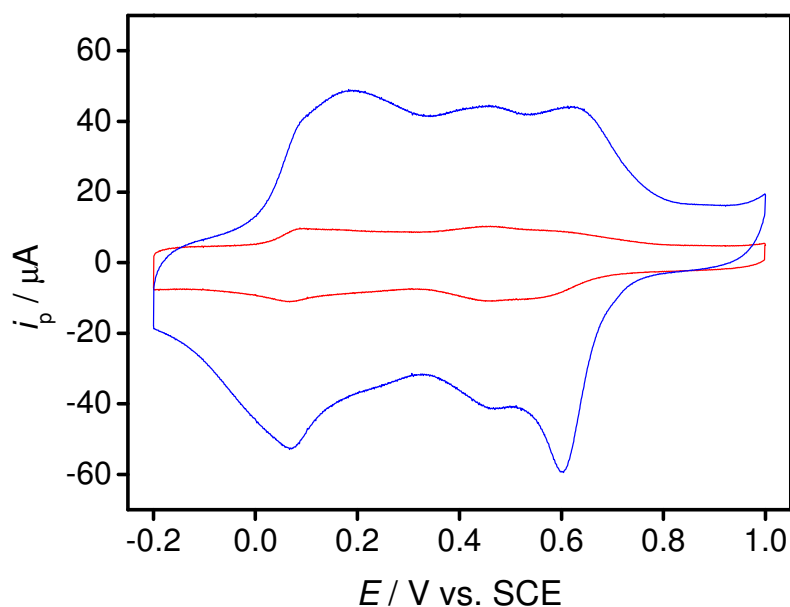
Figure 5.6: CVs of PAni polymerised for 3 min (red) and 5 min (blue) from a 0.2 M monomer solution onto an ITO electrode (unbiased during the polymerisation process). The scan rate was 0.2 V s^{-1} for both measurements.

5.3.3 UV-vis spectroscopy

In addition to the electrochemical measurements, UV-vis spectra were recorded to confirm the presence of PAni on the silica surface. Figure 5.7

shows a UV-vis spectrum of a quartz slide after it was immersed in a solution of 0.2 M aniline and 0.06 M sodium persulfate for 10 min. The spectrum shows a broad absorbance band 450 nm and 900 nm and is in very good agreement with previous measurements.[37]
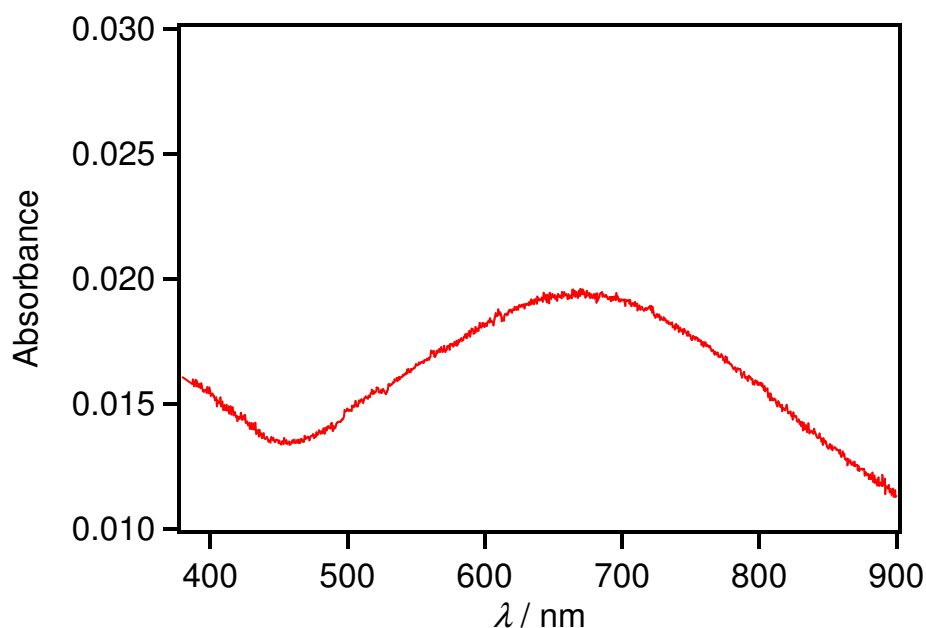
Figure 5.7: UV-vis spectrum of PAni nanoparticles on quartz after a polymerisation time of 10 min. The polymerisation was carried out using 0.2 M aniline and 0.06 M sodium persulfate.

5.3.4 EW-CRDS Measurements

Figure 5.8 shows a typical ring-down trace for the polymerisation of aniline using a monomer concentration of 0.2 M. At the beginning of the experiment, the cell was filled with water (A). The ring-down time was slightly shorter when the water was replaced by the aniline solution (B). After adding sodium persulfate, the polymerisation process started and PAni nanoparticles were formed on the surface, which led to a decrease in

121

the ring-down time. The polymerisation could be stopped again by replacing the aniline / sodium persulfate solution with water (D).
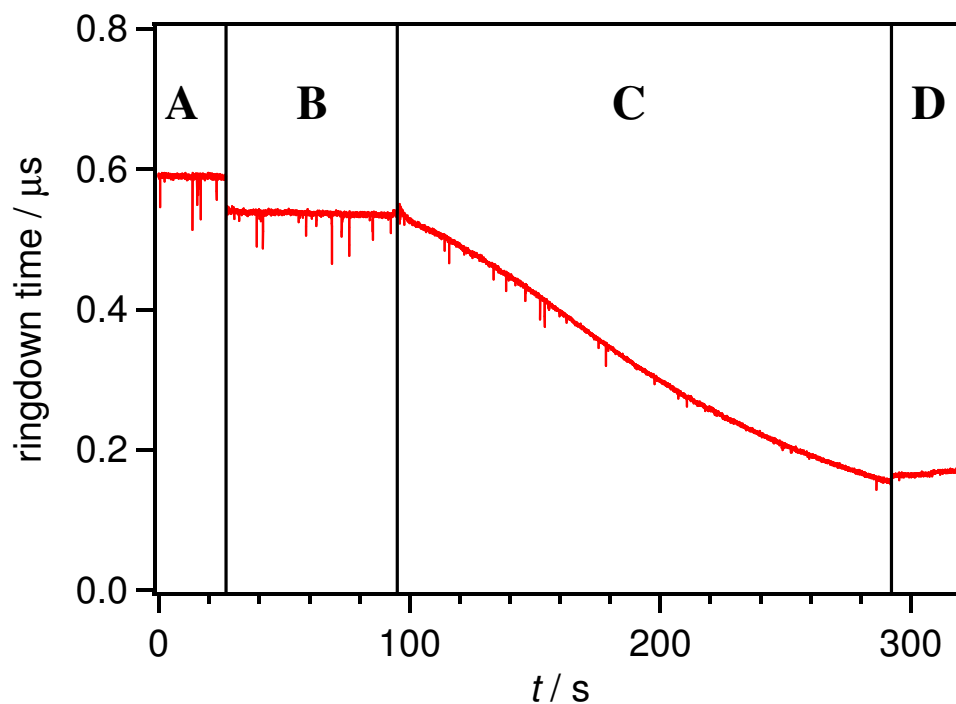
Figure 5.8: Experimental raw data for polymerisation of aniline using a 0.2 M monomer solution. The labelled sections represent different stages of the experiment. A) water only in cell, B) water was replaced by the monomer solution, C) sodium persulfate was added, starting the polymerisation, D) polymerisation process was stopped by replacing the solution with water.

Figure 5.9 shows typical interfacial absorbance transients derived from the EW-CRDS response for the *in situ* polymerisation of aniline for three different monomer concentrations.
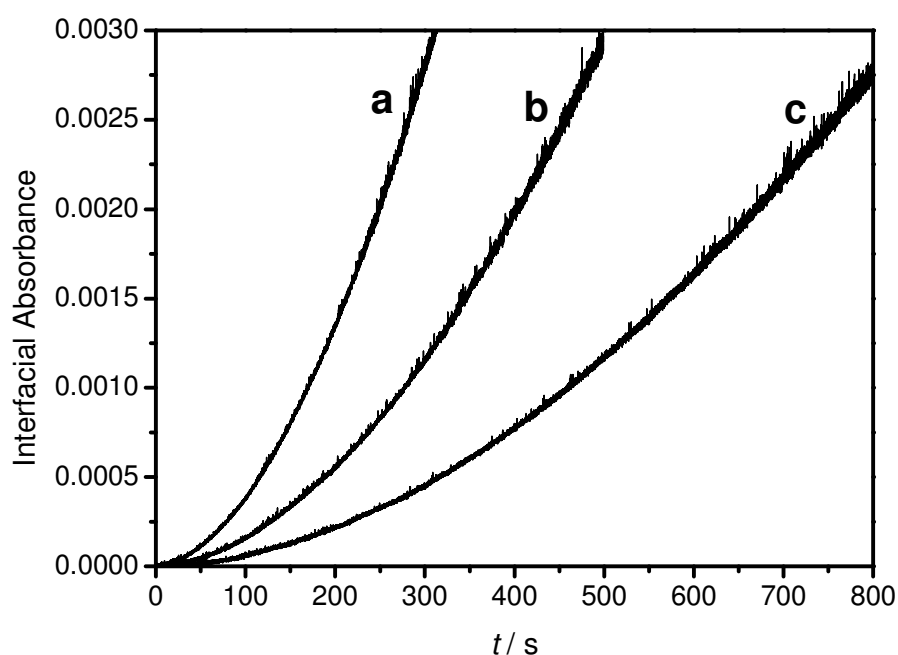
Figure 5.9: Absorbance transients measured by EW-CRDS for monomer concentrations of a) 0.2 M, b) 0.1 M and c) 0.05 M.

It can be seen that the absorbance traces are strongly dependent on the concentration of aniline and that the rate of change of absorbance increases with time for each concentration. The absorbance is due to the formation of PAni on the silica surface, as identified above by TM-AFM and electrochemistry. The overall reaction is depicted in scheme 5.1.[27]
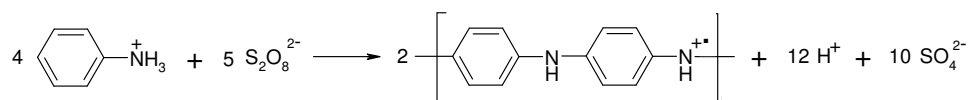
Scheme 5.1: Oxidative polymerisation of aniline.

In order to obtain an analytical solution for the polymerisation kinetics, we have to recognise that the process involves the growth of particles which we consider to be hemispherical, with a time-dependent surface area $\sigma(t)$. We assume a time-independent concentration of monomers in solution,

which is reasonable given the enormous excess of aniline used and the relatively slow kinetics of the polymerisation process. The change in the number of monomers per particle, N_{aniline}, with time can thus be written as:

$$\frac{dN_{\text{aniline}}(t)}{dt} = kcN_A \sigma(t) \tag{5.3}$$

where k is a heterogeneous polymerisation rate constant in cm s^{-1} and c the aniline concentration in mol cm^{-3}. The number of monomers per particle is

$$N_{\text{aniline}}(t) = \frac{\rho}{M_W} N_A V(t) \tag{5.4}$$

where M_W is the molar mass of aniline (g mol^{-1}) and $V(t)$ is the time-dependent volume of a polymer particle (cm^3). $V(t)$ can be converted to $\sigma(t)$ using $V(t) = \frac{1}{(18\pi)^{1/2}} \sigma(t)^{3/2}$, and so, from eq. 5.4, the number of monomers per particle is:

$$N_{\text{aniline}}(t) = \frac{\rho}{(18\pi)^{1/2} M_W} N_A \sigma(t)^{3/2} = \frac{1}{B} N_A \sigma(t)^{3/2} \tag{5.5}$$

where $B = (18\pi)^{1/2} M_W \rho^{-1}$. It is possible to reformulate eq. 5.3 using eq. 5.5 such that:

$$\frac{d\sigma(t)}{dt} = \frac{2}{3} Bkc\sigma(t)^{1/2} \tag{5.6}$$

The net absorbance measured by EW-CRDS can simply be described by:

$$Abs(t) = \varepsilon N_p N_{\text{aniline}}(t) N_A^{-1} \tag{5.7}$$

where ε is the extinction coefficient of PAni (at 405 nm) and N_p is the surface coverage of nanoparticles (cm^{-2}). εN_p can be determined at any time by a combination of EW-CRDS ($Abs(t)$) and TM-AFM and/or electrochemical measurements ($N_{aniline}(t)$). Additional TM-AFM measurement (data not shown) confirmed that N_p was independent of the monomer concentration over the range of aniline concentrations of interest. $N_{aniline}(t)$ is estimated from TM-AFM height measurements via

$$N_{aniline}(t) = \frac{2}{3}\pi \frac{\rho N_A}{M_W} r(t)^3 \qquad (5.8)$$

where $r(t)$ is the mean radius (height) of the hemispherical particles. The PAni nanoparticle radius can therefore be expressed in terms of the absorbance

$$r(t) = \left(\frac{3}{2} \frac{M_W}{\pi \rho \varepsilon N_p} \right)^{1/3} Abs(t)^{1/3} \qquad (5.9)$$

and the corresponding surface area is:

$$\sigma(t) = \left(\frac{B}{\varepsilon N_p} \right)^{2/3} Abs(t)^{2/3} \qquad (5.10)$$

Substituting eq. 5.10 into eq. 5.6 gives the polymerisation rate constant as a function of the absorbance measured by EW-CRDS, with all other parameters known.

$$k(t) = c^{-1} \left(B^2 \varepsilon N_p \right)^{-1/3} Abs(t)^{-2/3} \frac{d(Abs(t))}{dt} \qquad (5.11)$$

The absorbance transients can therefore be expressed in terms of a rate constant for polymerisation over the range of times of interest.

The polymerisation rate constant for a typical experiment with a monomer concentration of 0.1 M, extracted from absorbance data and plotted *vs*. the polymerisation time, is shown in figure 5.10a. It can be seen that at very early times ($t < 50$ s), the absorbance - and consequently the calculated rate constant - is small and the values are erratic. This is not unexpected as this is the nucleation stage where the initial particles are being formed and there will be a net build up in the number of particles to the fixed number seen at later times. Furthermore, the morphology of the PAni nanoparticles is likely to deviate significantly from the idealised hemispherical geometry of the model. These factors (especially the former) cause the rate constant extracted from the fixed nuclei model to initially be low. The peak in the rate constant value between $50 - 100$ s and the subsequent decrease with time suggests a size-dependent rate constant. However, there could be other effects contributing to this phenomenon such as desorption of oligomers from the surface or changes in the initial morphology of the PAni nanoparticles. On the other hand, since the extracted rate constant decreases by a factor of ca. 4 between $t = 1$ min and the long time asymptotic value of 1.1×10^{-7} cm s^{-1}, we consider it unlikely that a change in the geometry of the particles alone could account for the observed variation of k with time.
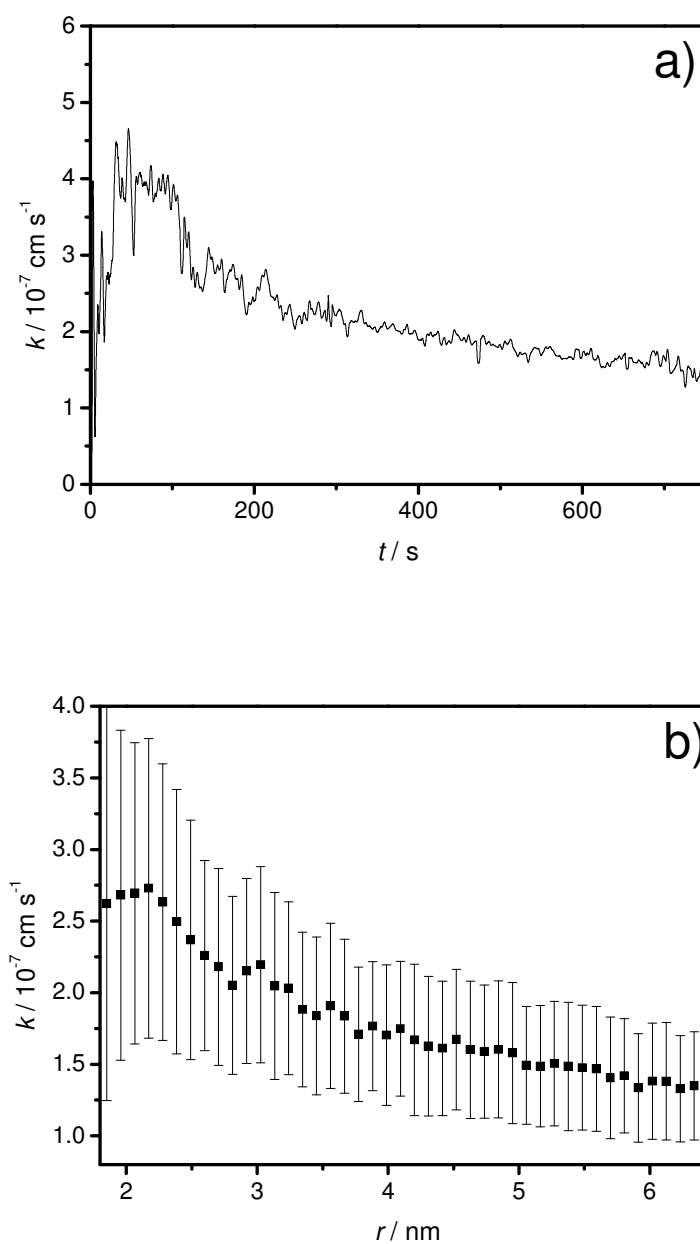
Figure 5.10: a) The polymerisation rate constant as a function of time for a typical EW-CRDS experiment using an aniline concentration of 0.1 M. The data were obtained from absorbance data that were converted to the polymerisation rate constant using eq. 5.11. b) The average polymerisation rate constant (from eq. 5.11) taken from 9 different experiments as a function of PAni nanoparticle radius (from eq. 5.9).

To explore further any potential size-dependence of the polymerisation rate constant, in Figure 5.10b we plot k (eq. 5.11) vs. r (eq. 5.9) from data representing the average of 9 individual EW-CRDS measurements. Clearly the rate constant decreases with increasing nanoparticle size (for $r > 2$ nm). The polymerisation rate constant for the larger particles ($r > 5$ nm) is 1.4 ($\pm$ 0.4) x 10^{-7} cm s^{-1} decreasing asymptotically to a value of 0.7 ($\pm$ 0.4) x 10^{-7} cm s^{-1}. For smaller particles ($r < 2$ nm), the rate constant is considerably larger, with values up to 2.7 ($\pm$ 1.1) x 10^{-7} cm s^{-1}.

We are not aware of any reports in the literature describing the elementary kinetics and rate constant for aniline addition, although size effects are prevalent in many areas of nanoscale chemistry.[60] There have, however, been some proposals to explain the kinetics of *in situ* polymerised PAni films. PAni film formation experimental data has been fitted to the Johnson-Mehl-Avrami (JMA) equation.[51] This process assumes three-dimensional growth of spheroids with no other nuclei being formed at the late stage of aniline polymerisation, both of which are consistent with our observations. Furthermore, the absorbance transients in Figure 5.9 resemble the experimental data obtained by Ayad *et al*., who followed the *in situ* film formation of PAni on gold with the QCM technique,[61] but who did not report rate. In a separate study Sapurina and Stejskal concluded that the rate of aniline oxidation remained constant, once the first PAni had been produced on the surface[3] which is again in agreement with our measurements. Moreover, they concluded that aniline polymerisation was heterogeneous, involving electron transfer to the

aniline monomer. Our results are, once again, consistent with this hypothesis and we have been able to demonstrate a simple model which takes this process into account. Our prediction of first order dependence on aniline for nanoparticle growth is further consistent with other studies,[54] although no rate constants were reported in those studies.

5.4 Conclusions

The early stage of the surface polymerisation of PAni on silica surfaces has been followed *in situ* by EW-CRDS, coupled with *ex-situ* TM-AFM measurements. Complementary voltammetry results have confirmed that the material produced is PAni. The process proceeds via the formation of hemispherical nanoparticles which grow with time, thus providing a means of forming arrays of PAni nanoparticles on surfaces. The EW-CRDS absorption transients were analyzed using a theoretical model developed to take account of all experimental observations. We find that the reaction is first-order in aniline (with 0.12 M sodium persulfate). The rate constant in the limit of large particle size is 0.7 ($\pm$ 0.4) x 10^{-7} cm s^{-1}. However, within the assumption of the model used, the polymerisation rate constant decreases monotonically with increasing particle size from a maximum value of *ca.* 2.7 ($\pm$ 1.1) x 10^{-7} cm s^{-1} for a particle of 2 nm radius. This could suggest size-dependent polymerisation kinetics, but could also be explained (at least partly) by a change in the particle morphology during growth or the adsorption of oligomers at the interface at short times (enhancing the measured optical absorbance), which subsequently desorb from the surface.

5.5 References

(1)   Nalwa, H. S., Ed. *Conductive Polymers: Transport, Photophysis and Applications*; John Wiley & Sons Ltd: Chichester, United Kingdom, 1997.

(2)   Macdiarmid, A. G.; Epstein, A. J. *Faraday Discussions* **1989**, 317.

(3)   Sapurina, I.; Stejskal, J. *Polymer International* **2008**, *57*, 1295-1325.

(4)   Letheby, H. *Journal of the Chemical Society - Transactions* **1862**, *15*, 161-163.

(5)   Monkman, A. P.; Adams, P. *Synthetic Metals* **1991**, *40*, 87-96.

(6)   Huang, W. S.; Macdiarmid, A. G. *Polymer* **1993**, *34*, 1833-1845.

(7)   Laska, J.; Widlarz, J. *Polymer* **2005**, *46*, 1485-1495.

(8)   Bormashenko, E.; Pogreb, R.; Sutovski, S.; Shulzinger, A.; Sheshnev, A.; Izakson, G.; Katzir, A. *Synthetic Metals* **2004**, *140*, 49-52.

(9)   Batich, C. D.; Laitinen, H. A.; Zhou, H. C. *Journal of the Electrochemical Society* **1990**, *137*, 883-885.

(10)   Karg, S.; Scott, J. C.; Salem, J. R.; Angelopoulos, M. *Synthetic Metals* **1996**, *80*, 111-117.

(11)   Wang, H. L.; MacDiarmid, A. G.; Wang, Y. Z.; Gebler, D. D.; Epstein, A. J. *Synthetic Metals* **1996**, *78*, 33-37.

(12)   Yang, Y.; Westerweele, E.; Zhang, C.; Smith, P.; Heeger, A. J. *Journal of Applied Physics* **1995**, *77*, 694-698.

(13)   Yang, Y. F.; Mu, S. L. *Journal of Electroanalytical Chemistry* **1997**, *432*, 71-78.

(14)   Bartlett, P. N.; Whitaker, R. G. *Biosensors* **1987**, *3*, 359-379.

(15)   Gerard, M.; Chaubey, A.; Malhotra, B. D. *Biosensors & Bioelectronics* **2002**, *17*, 345-359.

(16)   Huang, J.; Virji, S.; Weiller, B. H.; Kaner, R. B. *Journal of the American Chemical Society* **2003**, *125*, 314-315.

(17)   Virji, S.; Huang, J.; Kaner, R. B.; Weiller, B. H. *Nano Letters* **2004**, *4*, 491-496.

(18)   Virji, S.; Kaner, R. B.; Weiller, B. H. *The Journal of Physical Chemistry B* **2006**, *110*, 22266-22270.

(19)   Agbor, N. E.; Petty, M. C.; Monkman, A. P. *Sensors and Actuators B-Chemical* **1995**, *28*, 173-179.

(20)   Dhawan, S. K.; Kumar, D.; Ram, M. K.; Chandra, S.; Trivedi, D. C. *Sensors and Actuators B-Chemical* **1997**, *40*, 99-103.

(21)   Janata, J.; Josowicz, M. *Nature Materials* **2003**, *2*, 19-24.

(22)   Macdiarmid, A. G.; Mu, S. L.; Somasiri, N. L. D.; Wu, W. Q. *Molecular Crystals and Liquid Crystals* **1985**, *121*, 187-190.

(23)   Novak, P.; Muller, K.; Santhanam, K. S. V.; Haas, O. *Chemical Reviews* **1997**, *97*, 207-281.

(24)   O'Mullane, A. P.; Dale, S. E.; Day, T. M.; Wilson, N. R.; Macpherson, J. V.; Unwin, P. R. *Journal of Solid State Electrochemistry* **2006**, *10*, 792-807.

(25) O'Mullane, A. P.; Dale, S. E.; Macpherson, J. V.; Unwin, P. R. *Chemical Communications* **2004**, 1606-1607.

(26) Kang, E. T.; Neoh, K. G.; Tan, K. L. *Progress in Polymer Science* **1998**, *23*, 277-324.

(27) Stejskal, J.; Kratochvil, P.; Jenkins, A. D. *Polymer* **1996**, *37*, 367-369.

(28) Genies, E. M.; Boyle, A.; Lapkowski, M.; Tsintavis, C. *Synthetic Metals* **1990**, *36*, 139-182.

(29) Turyan, I.; Mandler, D. *Journal of the American Chemical Society* **1998**, *120*, 10733-10742.

(30) Guiseppielie, A.; Pradhan, S. R.; Wilson, A. M.; Allara, D. L.; Zhang, P.; Collins, R. W.; Kim, Y. T. *Chemistry of Materials* **1993**, *5*, 1474-1480.

(31) Kobayashi, T.; Yoneyama, H.; Tamura, H. *Journal of Electroanalytical Chemistry* **1984**, *177*, 281-291.

(32) Cao, Y.; Mallouk, T. E. *Chemistry of Materials* **2008**, *20*, 5260-5265.

(33) Huang, W. S.; Humphrey, B. D.; Macdiarmid, A. G. *Journal of the Chemical Society-Faraday Transactions I* **1986**, *82*, 2385-&.

(34) Tzou, K.; Gregory, R. V. *Synthetic Metals* **1992**, *47*, 267-277.

(35) Goldenberg, L. M.; Petty, M. C.; Monkman, A. P. *Journal of the Electrochemical Society* **1994**, *141*, 1573-1576.

(36) Nohria, R.; Khillan, R. K.; Su, Y.; Dikshit, R.; Lvov, Y.; Varahramyan, K. *Sensors and Actuators B-Chemical* **2006**, *114*, 218-222.

(37) Mandler, D.; Unwin, P. R. *Journal of Physical Chemistry B* **2003**, *107*, 407-410.

(38) Zhang, J.; Burt, D. P.; Whitworth, A. L.; Mandler, D.; Unwin, P. R. *Physical Chemistry Chemical Physics* **2009**, *11*, 3490-3496.

(39) Troitsky, V. I.; Berzina, T. S.; Fontana, M. P. *Synthetic Metals* **2002**, *129*, 39-46.

(40) Ram, M. K.; Adami, M.; Sartore, M.; Salerno, M.; Paddeu, S.; Nicolini, C. *Synthetic Metals* **1999**, *100*, 249-259.

(41) Chiou, N. R.; Lui, C. M.; Guan, J. J.; Lee, L. J.; Epstein, A. J. *Nat. Nanotechnol.* **2007**, *2*, 354-357.

(42) Sawall, D. D.; Villahermosa, R. M.; Lipeles, R. A.; Hopkins, A. R. *Chemistry of Materials* **2004**, *16*, 1606-1608.

(43) Tran, H. D.; Norris, I.; D'Arcy, J. M.; Tsang, H.; Wang, Y.; Mattes, B. R.; Kaner, R. B. *Macromolecules* **2008**, *41*, 7405-7410.

(44) Wang, Y.; Jing, X. *The Journal of Physical Chemistry B* **2008**, *112*, 1157-1162.

(45) Zhang, L. J.; Wan, M. X. *Advanced Functional Materials* **2003**, *13*, 815-820.

(46) Zhang, D. H.; Wang, Y. Y. *Materials Science and Engineering B-Solid State Materials for Advanced Technology* **2006**, *134*, 9-19.

(47) Xia, H.; Narayanan, J.; Cheng, D.; Xiao, C.; Liu, X.; Chan, H. S. O. *The Journal of Physical Chemistry B* **2005**, *109*, 12677-12684.

(48) Ding, H. J.; Zhu, C. J.; Zhou, Z. M.; Wan, M. X.; Wei, Y. *Macromolecular Rapid Communications* **2006**, *27*, 1029-1034.

(49)   Sapurina, I.; Osadchev, A. Y.; Volchek, B. Z.; Trchová, M.; Riede, A.; Stejskal, J. *Synthetic Metals* **2002**, *129*, 29-37.

(50)   Sapurina, I.; Riede, A.; Stejskal, J. *Synthetic Metals* **2001**, *123*, 503-507.

(51)   Travain, S. A.; de Souza, N. C.; Balogh, D. T.; Giacometti, J. A. *Journal of Colloid and Interface Science* **2007**, *316*, 292-297.

(52)   MacDiarmid, A. G. *Synthetic Metals* **1997**, *84*, 27-34.

(53)   Fedorova, S.; Stejskal, J. *Langmuir* **2002**, *18*, 5630-5632.

(54)   Ayad, M. M.; Gemaey, A. H.; Salahuddin, N.; Shenashin, M. A. *Journal of Colloid and Interface Science* **2003**, *263*, 196-201.

(55)   Wang, B.; Tang, J.; Wang, F. *Synthetic Metals* **1987**, *18*, 323-328.

(56)   Okabayashi, K.; Goto, F.; Abe, K.; Yoshida, T. *Synthetic Metals* **1987**, *18*, 365-370.

(57)   Genies, E. M.; Tsintavis, C. *Journal of Electroanalytical Chemistry* **1985**, *195*, 109-128.

(58)   Bard, A. J.; Faulkner, L. R. *Electrochemical Methods. Fundamentals and Applications*, 2. ed.; John Wiley & Sons, Inc., 2001.

(59)   Stejskal, J.; Sapurina, I.; Prokes, J.; Zemek, J. *Synthetic Metals* **1999**, *105*, 195-202.

(60)   Link, S.; El-Sayed, M. A. *International Reviews in Physical Chemistry* **2000**, *19*, 409-453.

(61)   Ayad, M. M.; Zaki, E. A. *Science and Technology of Advanced Materials* **2008**, *9*.

6 Monitoring the electrochemical reduction of cytochrome c immobilised on silica

In this chapter the electrochemical reduction of an adsorbed layer of cytochrome c immobilised on fused silica by ethylenediaminetetraacetic acid iron(II) complex (FeEDTA^{2-}) has been monitored using EW-CRDS. Using finite-element modelling, the rate of electron transfer (ET) between electrochemically generated FeEDTA^{2-} and cytochrome c (in its oxidised form) has been deduced. In order to monitor the time-dependent reduction of this protein spectroscopically, a frequency doubled Ti-Saphire laser (400 nm) was employed. The tunability of this laser together with an improved signal to noise ratio led to a significant improvement of the EW-CRDS technique.

6.1 Introduction

Immobilised cytochrome c on electrodes has been of great interest in the physical sciences where the redox properties, especially the ET mechanism, were studied using CV,[1-3] SERS[1-2] impedance spectroscopy[3-4] and spectroscopic techniques such as UV-vis and electron paramagnetic resonance spectroscopy[2] as well as X-ray photoelectron spectroscopy.[4] ET is fundamental to many biological processes, especially the respiration chain which involves a cascade of ET events between redox proteins.[5] In

order to understand the ET mechanism, proteins have been studied spectroscopically in solution.[7-15] The first demonstration of a CV of cytochrome *c* has been demonstrated by Eddowes and Hill[6] and Yeh and Kuwana[7] independently in 1977.

A very useful and widely used tool to study the ET between proteins and electrodes is Protein Film Voltammetry (PFV).[8] This technique is especially useful to examine electrochemically the active sites of redox proteins on surfaces in novel devices such as biosensors, bioelectronics and biofuel cells.[9-10] By varying the potential at an electrode, not only the formal potential but also kinetic information such as the rates of ET between the electrode and protein and thermodynamic constants of these electroactive proteins can be obtained.[11-14] Although PFV has been very successful in investigating redox mechanisms, it is somewhat limited due to the difficulty to arrange the proteins on the electrode in such a way that fast ET from the protein to the electrode is ensured, as well as optimal accessibility of the protein to its redox partners.[15-16] Additionally, the analysis of the ET kinetics can be quite challenging because the current is only an indirect measure for the ET between proteins.[17]

The adsorption of cytochrome *c* has been investigated recently by van der Sneppen *et al.* by mounting flow cell on top of the prism.[18] The authors showed that the adsorption of cytochrome *c* is irreversible on all investigated surfaces which were bare silica, octadecyl terminated and NH_2 terminated silica. The bare silica surface showed the highest affinity towards the cytochrome *c* followed by NH_2 coating and the octacecyl surface. In this chapter we use the thin layer cell EW-CRDS configuration

(as used in chapter 4) to study the well-known adsorption behaviour of cytochrome *c*. By introducing a redox mediator in the thin layer cell, the ET mechanism between the mediator and the cytochrome *c* could be investigated and described due to the difference of the absorbances of the two redox states of the protein. In order to discriminate between the two forms, a frequency doubled Ti-Saphire laser ($\lambda = 400$ nm) was employed since the difference in the absorbance is higher at this wavelength than at 405 nm using the diode laser employed in previous measurements (chapter 4 and 5).

6.2 Experimental

6.2.1 Materials

Horse-heart cytochrome *c*, potassium chloride, sodium dithionite and ethylenediaminetetraacetic acid iron(III) sodium salt (FeEDTA⁻) (all Sigma-Aldrich) were used as received and stored in the dark. Solutions were prepared using ultrapure Milli-Q water (Millipore) freshly prior each experiment. Solutions were deaerated with N_2 and kept under N_2 atmosphere.

6.2.2 UV-vis Spectroscopy

UV-vis spectra were recorded using a Jasco V660 spectrophotometer. 100 μM solution of reduced cytochrome *c* was degassed with N_2, added to a 1 mg cm^{-3} solution of sodium dithionite and diluted to 20 μM before the

spectrum was recorded. The oxidised cytochrome c was diluted to 20 µM without degassing with N_2.

6.2.3 EW-CRDS

EW-CRDS measurements were carried out in a similar way as described previously (Chapters 3-5). The difference in this setup however was that the light source was chosen to be the second harmonic (SHG, generated using Type I β-barium borate (BBO) crystal) of a commercially available femtosecond Ti-Saphire laser (SpectraPhysics XP Regenerative amplifier) at a repetition rate of 1 kHz. Since this type of laser allows the wavelength to be tuned, the wavelength for these experiments was chosen to be 400 nm because of the pronounced difference in the absorption spectra for the two redox forms of cytochrome c (see Figure 6.3). Figure 6.1 shows the beam path for the frequency generation and the pulse stretching. After the laser beam has been led through the two BBO crystals, a mirror reflects only the third harmonic and transmits the fundamental and the second harmonic. After a series of mirrors which filter out the fundamental frequency (800 nm) only the second harmonic eventually enters a 1 m fused silica rod in order to stretch the pulse duration and decrease the power per pulse. The laser pulse was then further stretched using a 20 m single-mode optical fibre and introduced into the optical cavity in the same way as described in previous chapters.
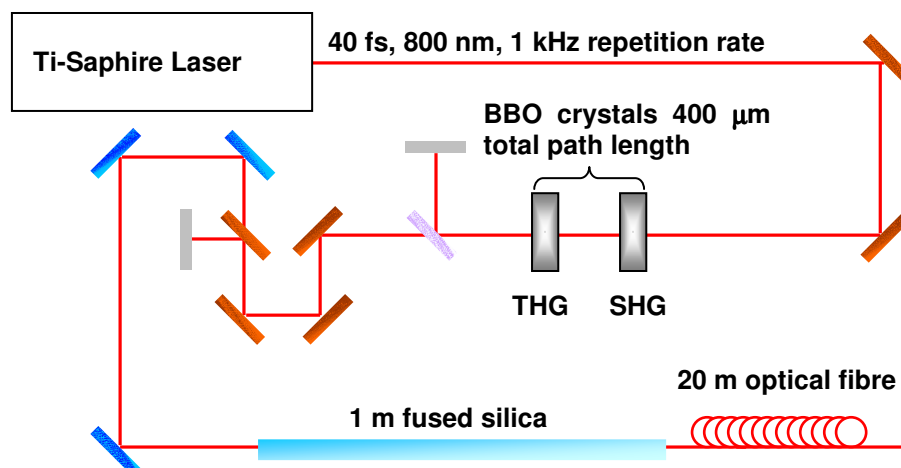
Figure 6.1: Schematic of the laser setup. The light pulses were generated using a Ti-Saphire laser. The chosen wavelength of 400 nm was obtained by SHG using a Type I BBO crystal. The BBO crystal for third harmonic generation (THG) was used to generate 266 nm light for a separate experiment. The pulse duration was stretched subsequently by two mirrors, a 1 m fused silica rod and a 20 m optical fibre. Calculations concerning the pulse duration can be found in the text.

The absorbance due to species present in the evanescent field was calculated in the same way as described in chapter 3.

6.2.3.1 Comparison of the ps laser setup to the diode laser setup

It was found, that the signal to noise ratio of the laser system described above was significantly larger than for the diode laser system described in the previous chapters. Figure 6.2A and Figure 6.2B show a comparison of the ring-down traces for a triangular ring cavity measured using a 405 nm diode laser and the 400 nm laser, respectively. In both plots, two individual ring-down traces are shown. In order to have a measure of the signal to noise ratio, the standard deviation was calculated for the two traces at each

data point. It was found that there was a ~20 fold increase in the signal to noise ratio of the fs laser compared to the continuous wave diode laser.
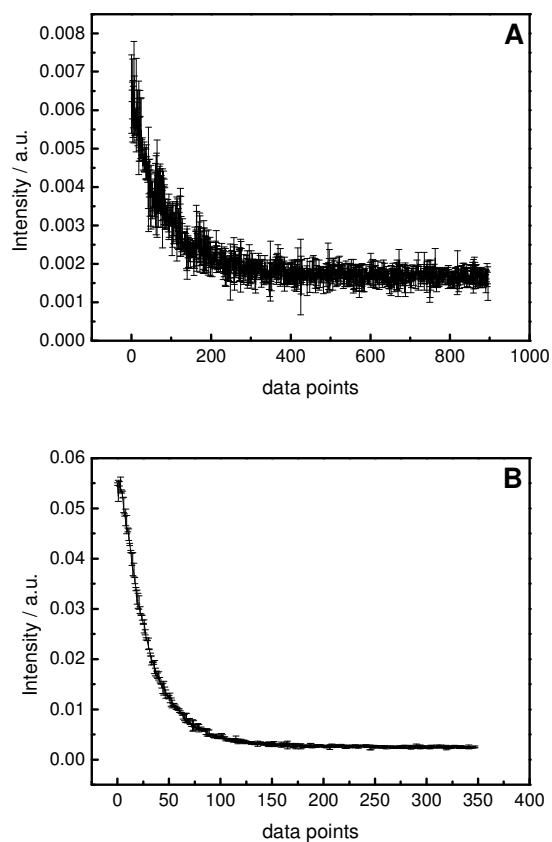
Figure 6.2: Typical ring-down traces for A) the diode laser used for the work in Chapters 4 and 5 and B) the fs laser used in this chapter. In both graphs, two traces are overlaid. The error bars are calculated using the standard deviation of the two traces at each data point.

6.2.4 Electrochemistry

Electrochemical experiments were carried out in circular PTFE cell using a standard 3 electrode system employing a 2 mm diameter Pt disc working electrode, a Pt wire counter electrode and a chlorinated (AgCl) Ag wire reference electrode. The current was measured using a homebuilt potentiostat and transferred onto a National Instruments card (NI PCIe-6251). In order to carry out electrochemical and EW-CRDS measurements

138

simultaneously, the Pt macroelectrode was carefully aligned above the evanescent field at a distance of 100 μm from the prism surface using an x, y, z micropositioner. LabVIEW software was employed to measure the electrochemical and EW-CRDS responses.

6.3 Results and Discussion

6.3.1 Calculation of pulse duration

Although the duration of a laser pulse exiting the Ti-Saphire laser is 40 fs, it gets stretched in time due to several effects. A small effect will be caused by the two crystals responsible for SHG and THG which, together, have a path length of 400 μm. Then the light travels through two mirrors which reflect the unwanted third harmonic (266 nm) and the fundamental mode (800 nm) and which have a thickness of 2 mm each. The pulse is then stretched by travelling through a fused silica rod (1 m). Finally, a 20 m silica single mode optical fibre has the biggest effect on the pulse duration. It is possible to calculate the effective pulse duration[19] using

$$t_{pulse1} = \tau_0 \left[1 + \left(\frac{4 \ln 2 \Phi''(\omega)}{t_{pulse0}^2} \right)^2 \right]^{1/2} \tag{6.1}$$

where t_{pulse1} is the broadened pulse duration, t_{pulse0} the initial pulse duration and $\Phi''(\omega)$ the frequency dependent group velocity dispersion per cm. The later constant can be described by

$$\Phi''(\omega) = \beta''(\omega) z \tag{6.2}$$

where z is the path length of the dispersive medium (*i.e.* mirrors, silica rod and optical fibre) and $\beta''(\omega)$ is the group velocity dispersion. These values depend on the material and the frequency of the light and are tabulated. In the case of silica, $\beta''(\omega) \cong 1000$.[20]

The effective pulse duration can be determined by applying eq. 6.1 to the aforementioned different effects. It has to be noted that the initial pulse duration, τ_0, is always 40 fs and does not change. If we assume transform-limited behaviour, the pulse is defined by

$$t_{\text{pulse}} = \frac{0.441}{\Delta E} \tag{6.3}$$

where ΔE is constant. This is due to the fact that short laser pulses are broad in frequency and all frequency components still have to be included in the pulse. The effect of the SHG and THG crystals is minimal and can be neglected. The two mirrors add 9 fs, the fused silica rod 6.9 ps and the optical fibre 139 ps to the pulse duration. The overall pulse duration before entering the ring-down cavity is approximately 146 ps, since pulse broadening is additive.

It was found that a typical ring-down time is 300 ns. It takes approximately 3 times longer for the light in the optical cavity to disappear; therefore after 900 ns we can assume that the light intensity in the optical cavity is negligible. If we take into account the length of the cavity (78 cm), 900 ns corresponds to 346 ring-down events.

Again, using eq. 6.1, we can calculate the stretching of the pulse due to the fused silica prism. If we assume a path length of 1 cm, the

stretching is 24 ps. The pulse duration after 900 ns is therefore ~177 ps. The time for one roundtrip in the optical cavity is defined as

$$t_{RT} = \frac{L}{c_L} \tag{6.4}$$

where L is the length of the cavity and c the speed of light. In our optical cavity, $t_{RT} = 2.6$ ns which means that even after most of the light has been extinguished; the pulse duration is still very much shorter than the length of the cavity.

6.3.2 UV-vis Spectroscopy

Figure 6.3 shows the absorption spectra of the two redox forms of cytochrome c. It was found that the extinction coefficients (at 400 nm) were 5.87 x 10^4 dm^3 mol^{-1} cm^{-1} for the oxidised and 3.79 x 10^{-4} dm^3 mol^{-1} cm^{-1} reduced cytochrome c, respectively. These values can later be used to calculate the ratio of the surface concentration of the two redox forms of cytochrome c on the prism surface during the electrochemical experiments. The peak positions of the two spectra are in good agreement with previous measurements.[9]
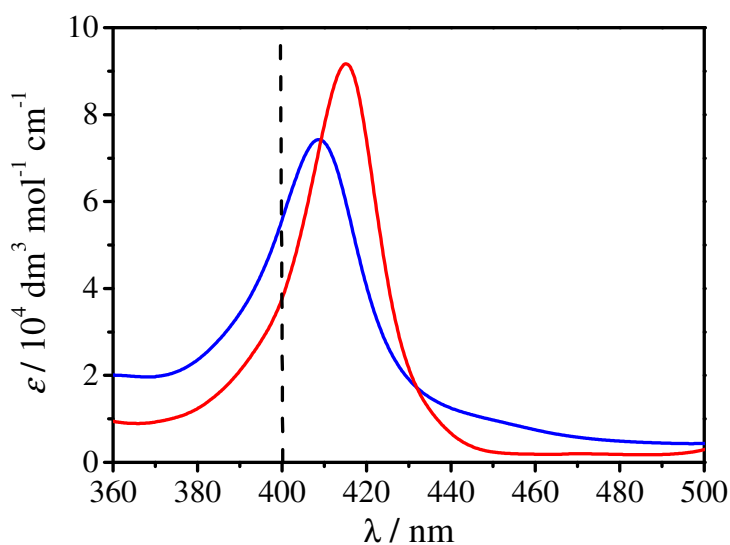
Figure 6.3: UV-vis spectra of the oxidised (blue) and reduced form of cytochrome *c*. The black dashed line represents the wavelength of the laser used for the EW-CRDS experiments.

6.3.3 Adsorption of cytochrome *c* on silica

Figure 6.4 shows a typical optical-absorbance transient for adsorption of cytochrome *c* in 0.1 M KCl (5 µM volume) on silica. The optical absorbance rises after dropping the solution onto the surface and reaches a maximum value of 0.004, which corresponds to a surface coverage of 6.8×10^{-11} mol cm^{-2}. If one takes into account a diameter of 3.4 nm for this roughly spherical protein,[21] the maximum surface concentration for a closed packed monolayer should be approximately 1.8×10^{-11} mol cm^{-2}. This is clearly much less than the maximum value in Figure 6.3. A possible explanation is that a monolayer of cytochrome *c* binds very strongly on the silica surface, but more cytochrome *c* proteins can adsorb on top of this layer (multilayer adsorption). These proteins are bound much more weakly

and can be washed away, when the solution is removed and the cell is washed with 0.1 M KCl (red line in Figure 6.4). This effect was confirmed by forming a sub-monolayer of cytochrome *c* and rinsing the cell. In this case, the absorbance stayed constant during the washing cycle and no cytochrome *c* proteins were removed from the surface. After the washing step, approximately 3×10^{-11} mol cm^{-2}. The shape and the coverage are in good agreement with earlier reports.[18] It is important to note that the conformation of cytochrome *c* does not change upon adsorption on silica and the absorbance properties of cytochrome *c* in solution are believed to be the same as on silica.[21]
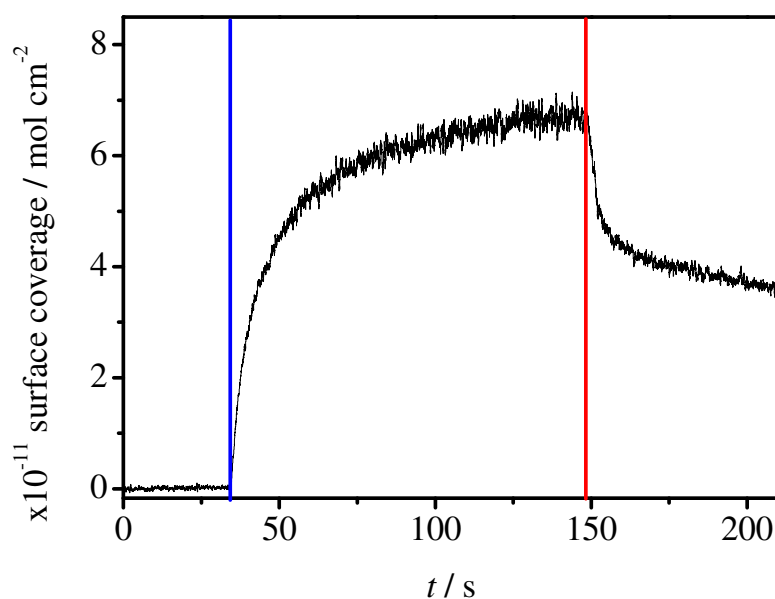
Figure 6.4: EW-CRDS response for the adsorption of 5 µM cytochrome *c* in 0.1 M KCl. The solution was introduced after 34.2 s (blue line). After 148 s the solution was removed and the surface washed with 0.1 M KCl.

6.3.4 Reduction of cytochrome *c* by electrogenerated FeEDTA^{2-}

After the adsorption and washing process, the adsorbed layer of cytochrome *c* was electrochemically reduced using different concentrations of FeEDTA^{-} in 0.1 M KCl. The introduction of the mediator solutions had no effect on the ring-down time, which indicates that the FeEDTA^{-} within the evanescent field does not contribute the optical absorbance. The cytochrome *c* did not appear to desorb from the surface (as indicated by a stable ring-down time) and it is also reasonable to assume that the FeEDTA$^{-/2-}$ redox pair does not bind to the prism surface due to charge repulsion from the negatively charged silica surface. The Pt macroelectrode was aligned 100 µm above the silica surface. In this way, a thin layer cell was formed between the electrode and the prism. The potential was stepped from 0.0 V to -0.5 V vs. Ag/AgCl for 60 s and then returned to the open circuit potential. Figure 6.5 shows the potential (A) and the current (B) as a function of time for a chronoamperometric experiment using a concentration of 0.1 mM of FeEDTA^{-}.
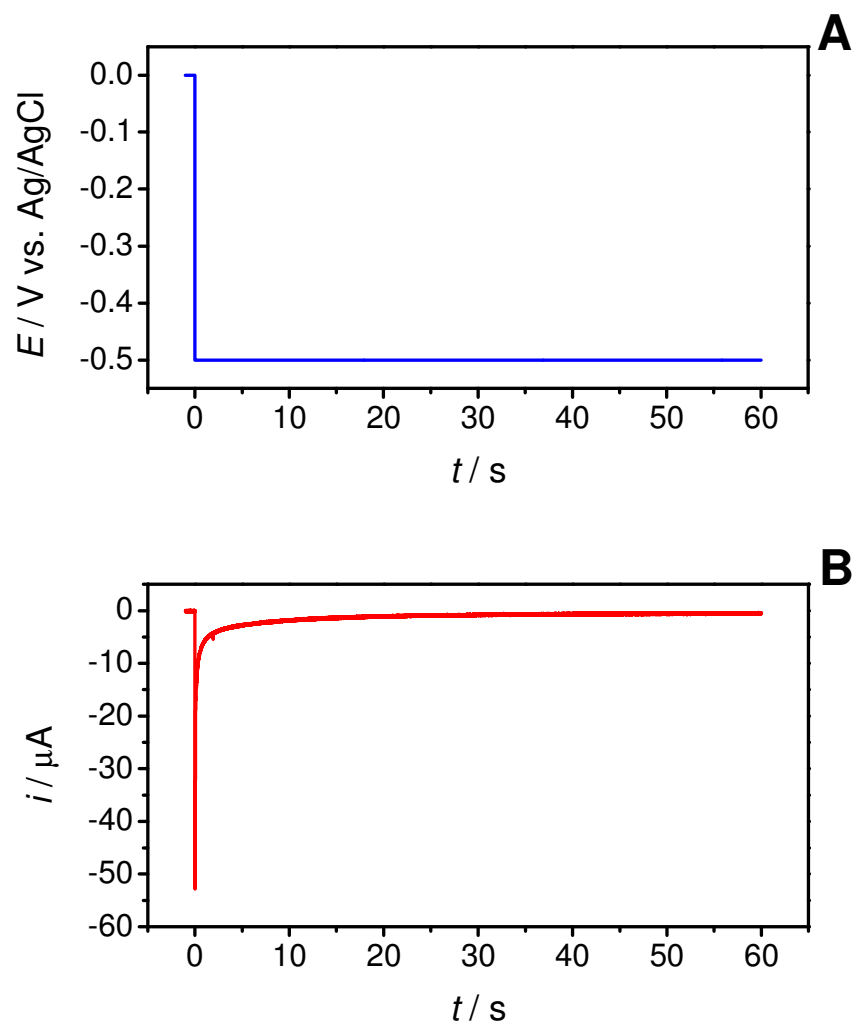
Figure 6.5: A) Potential applied to the Pt macroelectrode as a function of time. The potential was stepped from 0.0 V to – 0.5 V *vs*. Ag/AgCl at $t = 0$ for 60 s. B) Corresponding current transient as measured by the potentiostat.

The EW-CRDS responses for different FeEDTA$^-$ concentrations (0.5 mM 0.75 mM and 1 mM) were recorded simultaneously and are displayed in Figure 6.6. It was difficult to obtain exactly the same coverage of cytochrome *c* in each experiment. In order to compare different transients, the absorbance was converted into the ratio of oxidised cytochrome *c* to the total cytochrome *c* on the surface, $\theta_O(t)$. This ratio was calculated using the extinction coefficient for the two redox states,

which were obtained by UV-vis spectroscopy. Assuming that all cytochrome *c* on the surface is oxidised at *t* = 0, the surface coverage, *N*, can be described by

$$N = \frac{Abs(0)}{\varepsilon_O} \tag{6.5}$$

where $Abs(0)$ is the initial absorbance. The time-dependent absorbance is simply the sum of the absorbances due to oxidised and reduced cytochrome *c*.

$$Abs(t) = N\varepsilon_O\theta_O(t) + N\varepsilon_R\theta_R(t) \tag{6.6}$$

where $\theta_R(t)$ is the time-dependent ratio of reduced cytochrome *c* to the total cytochrome *c* on the surface. Since $\theta_O(t) + \theta_R(t) = 1$, eq. 6.6 can be solved for $\theta_O(t)$:

$$\theta_O(t) = \frac{Abs(t) - N\varepsilon_R}{N(\varepsilon_O - \varepsilon_R)} \tag{6.7}$$
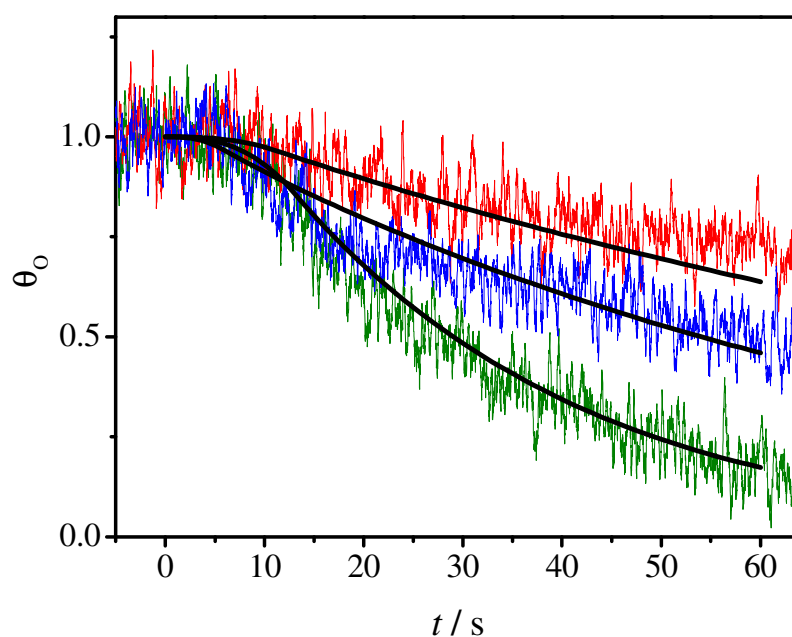
Figure 6.6: EW-CRDS transients for the electrochemical oxidation of adsorbed layers of cytochrome *c* on silica using a concentration of FeEDTA^{2-} of 0.5 mM (red), 0.75 mM (blue) and 1 mM (green). The best fits to the model (black lines) yielded rate constants of 4.0 x 10^{-9} cm s^{-1}, 4.0 x 10^{-9} cm s^{-1} and 5.0 x 10^{-9} cm s^{-1} for FeEDTA^{2-} concentrations of 0.5 mM, 0.75 mM and 1 mM, respectively.

It was shown that the reduction of FeEDTA$^-$ in a thin layer cell configuration does not have an effect on the ring-down time when the cytochrome *c* layer was absent (data not shown). Therefore the change in the absorbance in the evanescent field is only due to the change of the redox state of cytochrome *c* on the surface.

The same experiment can be carried out using the diode laser system as described in chapters 4 and 5. However, at $\lambda = 405$ nm the difference in the absorbance of the two redox states of cytochrome *c* (Figure 6.3) is not pronounced and hence no change in the ring-down time

147

can be observed (data not shown). This also means, that the change in the ring-down time as measured by the 400 nm laser setup is not due to desorption of cytochrome c from the surface. As shown in Figure 6.7, the FeEDTA$^{-/2-}$ redox pair does not contribute to the absorbance. In this control experiment, 1 mM FeEDTA- was reduced in 60 s potential step experiment without the cytochrome c adsorbed on the surface.
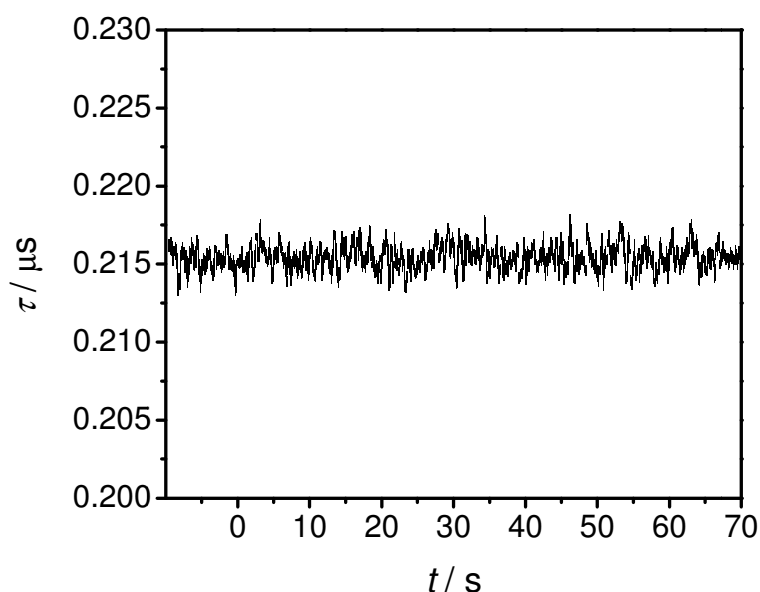
Figure 6.7: Ring-down time as a function of time for a potential step experiment (step time: 60 s) using 1 mM FeEDTA$^-$ with no cytochrome c present.

All three transients in Figure 6.6 show an initial lag time of around 5 s before the cytochrome c is reduced by the generated FeEDTA^{2-} at $t = 0$. This is due to the time it takes for the FeEDTA^{2-} to diffuse down to the prism surface. This effect has also been observed previously in such thin layer cell experiments (Chapter 4). It can be seen that nearly all cytochrome c is reduced after the potential step if 1 mM FeEDTA$^-$ is used. For lower concentrations of the mediator, the reduction process is slower

since the surface concentration of FeEDTA^{2-} is lower. The data in Figure

6.5 can be modelled using COMSOL Multiphysics 3.5 finite element

modelling (as demonstrated already in Chapter 4). The fits to the

experimental data and the calculation of the corresponding rate constants

have been carried out by Hayley Powell. Briefly, a one-dimensional

diffusion equation for the concentration of FeEDTA$^-$ was solved between

the electrode and the prism. The boundary conditions at the prism surface

take into account Butler-Volmer kinetics and can be described by

$$D\frac{\partial c_O}{\partial x} = k_0 \left(c* - c_O\right)\theta_O \exp\left(-\frac{\alpha F \Delta E}{RT}\right)$$
$$N\frac{d\theta_O}{dt} = -k_0 \left(c* - c_O\right)\theta_O \exp\left(-\frac{\alpha F \Delta E}{RT}\right)$$

$$(6.8a + 6.8b)$$

where D is the diffusion coefficient of FeEDTA$^-$, k_0 the rate constant for

the reduction of cytochrome c in cm s^{-1}, c_O the concentration of the

electrochemically generated FeEDTA^{2-}, $c*$ the bulk concentration of

FeEDTA$^-$ and α the ET coefficient (taken to be 0.5).[22] ΔE is the potential

drop at the interface and depends on the concentration for the reduced and

oxidised form of the mediator as demonstrated recently.[23-24]

$$\Delta E = E_{FeEDTA} - E_{cytc} + \frac{RT}{nF}\ln\left(\frac{c_O}{c* - c_O}\right)$$

$$(6.9)$$

where E_{FeEDTA} is the formal redox potential of FeEDTA$^{-/2-}$ (120 mV vs.

NHE)[25] and E_{cytc} the formal redox potential of cytochrome c (260 mV *vs.*

NHE).[26] Fits to the experimental data have been carried out by varying k_0

since all other factors are constant. The average rate constants were found

to be 4.0 x 10^{-9} cm s^{-1} for 0.5 mM, 4.0 x 10^{-9} cm s^{-1} for 0.75 mM and 5.0 x 10^{-9} cm s^{-1} for 1 mM, the average rate constants was 4.3 ($\pm$0.6) x 10^{-9} cm s^{-1}. This rate constant can be converted into a second-order rate constant, k, using

$$k = \frac{k_0 \exp(E_{FeEDTA} - E_{cytc})}{N} \qquad (6.10)$$

giving a value of 2.7 ($\pm$0.6) M^{-1} s^{-1}. There have been previous reports in the literature which have determined the ET rate for cytochrome c by redox mediators in solution. Most studies were employing the Marcus theory for outer sphere ET. Depending on experimental conditions such as pH and ionic strength, the ET rate constant for FeEDTA^{2-} and oxidised cytochrome c is usually in the range of 4.1 - 5.8 x 10^3 M^{-1} s^{-1}.[10, 11, 27] Rate constants have been reported for ET between cytochrome c an other small inorganic molecules such as pentaammineruthenium(II/III) complexes[7, 12] and Copper complexes.[27-28] These constants are typically of the same order of magnitude if not larger. The rate constant for ET of cytochrome c to its natural redox partners (cytochrome c peroxidase and cytochrome c oxidase) are even higher and can reach up to 4 x 10^6 M^{-1} s^{-1}.[29-30] One possibility to explain, why our ET rate is so slow compared to these other studies is the fact that cytochrome c might be oriented in such away on the fused silica surface that the electrochemically active heme groups are close to the prism surface due to electrostatic interactions between the positively charged lysine residues which surround the active site and the negatively charged silanol groups of the fused silica. Therefore, the ET mechanism between the FeEDTA^{2-} and the cytochrome c becomes less favourable.

There has been a report in the literature, where the ET rate of immobilised cytochrome *c* was obtained using a SECM setup. The proteins were adsorbed on a gold electrode using a self-assembled monolayer (11-mercaptoundecanoic acid). The electrode was held at a potential sufficient to drive the reduction of the cytochrome *c* layer. A UME was employed to study the heterogeneous ET constant between the electrochemically generated $Fe(CN)_6^{3-}$ and the cytochrome *c* at the gold electrode. The rate constant was found to be 2×10^4 M^{-1} s^{-1} which can be explained by the fact that the electrode potential of the biased gold electrode was not taken into account for calculating the ET rate constant.

6.4 Conclusions

In this chapter, the ET rate constant between a surface bound layer of cytochrome *c* on fused silica and the redox mediator $FeEDTA^{2-}$ was extracted using EW-CRDS in combination with chronoamperometry in a thin layer cell arrangement. The rate constant was obtained using finite-element modelling and was found to be 4.3 ($\pm$0.6) x 10^{-9} cm s^{-1} (which corresponds to a second order rate constant of 2.7 ($\pm$0.6) M^{-1} s^{-1}). It is hard to measure surface and ET kinetics with other techniques such as PFV since these techniques change the environment by applying a bias to the surface on which the proteins are bound. We have shown that it is possible to directly monitor ET between surface immobilised proteins and other molecules using EW-CRDS.

The EW-CRDS experiments were carried out using a Ti-Saphire laser with a pulse duration of 40 fs. The pulse duration was stretched to

146 ps using a fused silica rod and a single mode optical fibre before entering the optical cavity. It was shown, that the pulse duration was always considerable shorter than the length of the cavity. The signal to noise ratio for individual ring-down traces was found be increased by a factor of 20 compared to the conventional diode laser setup.

6.5 References

(1) Dick, L. A.; Haes, A. J.; Van Duyne, R. P. *Journal of Physical Chemistry B* **2000**, *104*, 11752.

(2) Oellerich, S.; Wackerbarth, H.; Hildebrandt, P. *Journal of Physical Chemistry B* **2002**, *106*, 6566.

(3) Sagara, T.; Niwa, K.; Sone, A.; Hinnen, C.; Niki, K. *Langmuir* **1990**, *6*, 254.

(4) Song, S.; Clark, R. A.; Bowden, E. F.; Tarlov, M. J. *Journal of Physical Chemistry* **1993**, *97*, 6564.

(5) Alberts, B. *Essential cell biology*; Garland Science: New York, 2010.

(6) Eddowes, M. J.; Hill, H. A. O. *Journal of the Chemical Society-Chemical Communications* **1977**, 771.

(7) Yeh, P.; Kuwana, T. *Chemistry Letters* **1977**, 1145.

(8) Armstrong, F. A. *Russian Journal of Electrochemistry* **2002**, *38*, 49.

(9) Macyk, J.; van Eldik, R. *Dalton Transactions* **2003**, 2704.

(10) Meier, M.; Sun, J.; Wishart, J. F.; van Eldik, R. *Inorganic Chemistry* **1996**, *35*, 1564.

(11) Gorodetsky, A. A.; Boal, A. K.; Barton, J. K. *Journal of the American Chemical Society* **2006**, *128*, 12082.

(12) Hirst, J. *Biochimica Et Biophysica Acta-Bioenergetics* **2006**, *1757*, 225.

(13) Kievit, O.; Brudvig, G. W. *Journal of Electroanalytical Chemistry* **2001**, *497*, 139.

(14) Vincent, K. A.; Armstrong, F. A. *Inorganic Chemistry* **2005**, *44*, 798.

(15) Armstrong, F. A. *Current Opinion in Chemical Biology* **2005**, *9*, 110.

(16) Armstrong, F. A.; Wilson, G. S. *Electrochimica Acta* **2000**, *45*, 2623.

(17) Astuti, Y.; Topoglidis, E.; Gilardi, G.; Durrant, J. R. *Bioelectrochemistry* **2004**, *63*, 55.

(18) van der Sneppen, L.; Gooijer, C.; Ubachs, W.; Ariese, F. *Sensors and Actuators B-Chemical* **2009**, *139*, 505.

(19) Paschotta, R. *Encyclopedia of Laser Physics and Technology*; illustrated ed.; Wiley-VCH, 2008.

(20) CVI; Optical Components and Assemblies: 2005.

(21) Cheng, Y. Y.; Lin, S. H.; Chang, H. C.; Su, M. C. *Journal of Physical Chemistry A* **2003**, *107*, 10687.

(22) Bard, A. J.; Faulkner, L. R. *Electrochemical Methods. Fundamentals and Applications*; 2. ed.; John Wiley & Sons, Inc., 2001.

(23) Solomon, T.; Bard, A. J. *Journal of Physical Chemistry* **1995**, *99*, 17487.

(24) Whitworth, A. L.; Mandler, D.; Unwin, P. R. *Physical Chemistry Chemical Physics* **2005**, *7*, 356.

(25) Kolthoff, I. M.; Auerbach, C. *Journal of the American Chemical Society* **1952**, *74*, 1452.

(26) Eddowes, M. J.; Hill, H. A. O. *Journal of the American Chemical Society* **1979**, *101*, 4461.

(27) Meier, M.; van Eldik, R. *Inorganica Chimica Acta* **1994**, *225*, 95.

(28) Meier, M.; van Eldik, R. *Chemistry-a European Journal* **1997**, *3*, 39.

(29) de Sousa, P. M. P.; Pauleta, S. R.; Rodrigues, D.; Goncalves, M. L. S.; Pettigrew, G. W.; Moura, I.; Moura, J. J. G.; dos Santos, M. M. C. *Journal of Biological Inorganic Chemistry* **2008**, *13*, 779.

(30) Silvestrini, M. C.; Tordi, M. G.; Colosimo, A.; Antonini, E.; Brunori, M. *Biochemical Journal* **1982**, *203*, 445.

7 Evanescent Wave Broadband Cavity Enhanced Absorption Spectroscopy: A New Probe of Electrochemical Processes

An evanescent-wave variant of broadband cavity enhanced absorption spectroscopy using a supercontinuum light source has been used to detect electrogenerated species at the silica-water interface. Broadband excitation is especially advantageous, since full spectra can be measured at a reasonable time resolution. In proof-of-concept experiments $[IrCl_6]^{2-}$ was produced by electro-oxidation of $[IrCl_6]^{3-}$ in a thin layer electrochemical cell. Diffusion of the $[IrCl_6]^{2-}$ across the cell to a silica interface was monitored yielding real-time concentrations within an evanescent field region at the interface. The optical response was compared with the electrochemical response during chronoamperometric step and CV experiments and both were simulated by finite element modelling. The experiment is highly sensitive to interfacial processes and its wide spectral width and fast time resolution make it a potentially powerful tool for *in situ* spectroscopic monitoring of processes and intermediates in dynamic electrochemistry.

7.1 Introduction

There has been a recent surge in efforts to bring the cavity enhanced techniques developed in the gas phase,[1] to bear on condensed phase problems.[2-4] One method capable of providing wide spectral information is broadband cavity enhanced spectroscopy (BB-CEAS). In its simplest incarnation, CEAS involves injection of light into a high finesse optical cavity. The time integrated intensity of light passing through the cavity provides a measure of inherent cavity losses and intracavity absorptions. The sensitivity is increased by the use of highly reflective cavity mirrors which vastly increases the effective path length, similar to the EW-CRDS technique (up to several km in gas-phase applications). Although mainly applied to gas-phase problems, incoherent BB-CEAS has been employed in conventional bulk liquid cells using white diodes.[5, 6]

In a recent paper, an incoherent broadband light source (short-arc Xe-lamp) was applied in a cavity-enhanced evanescent wave absorption method in order to study surface adsorbed metallo porphyrins.[7] The experimental setup involved an optical cavity in a folded cavity configuration. The light between 390 nm and 625 nm was measured using a diode array. It was found that an integration time of 100 ms was sufficient enough to obtain a strong signal. Stelmaszczyk *et al.* applied supercontinuum radiation (SCR) to CRDS and were able to measure sequentially the ring-down transients of selectively chosen wavelengths in a linear cavity but are limited to static experiments.[8] Later, the same authors measured the absorption spectrum of NO_2 using this SCR-CRDS technique.[9]

156

This chapter describes an evanescent wave variant of BB-CEAS (EW-BB-CEAS) developed to study electrochemical reactions at a silica-solution interface. The technique is sensitive to absorbing or scattering species present in the 200-500 nm deep evanescent field established beyond the interface whenever light is totally internally reflected. Typically, the time resolution of BB-CEAS is limited by the accumulation times required to establish high signal to noise. For these experiments, the speed of data acquisition was increased by incorporating an SCR source, providing both high spectral brilliance and extremely broadband wavelength coverage.[10-12] SCR is generated through nonlinear processes upon intense pumping of optical materials. The nonlinear effects are enhanced in photonic crystal fibres (PCFs)[13] and broadband SCR from the blue to the near-infrared is readily generated in PCFs using short laser pulses. The spectral brilliance of the SCR permits more rapid acquisition of spectra with higher signal to noise than other light sources such as Xe-lamps. This new instrument provides a powerful combination of broadband spectral information coupled with high sensitivity, high spatial resolution and high time resolution.

By way of demonstration of the EW-BB-CEAS technique for electrochemical applications, the electrogeneration of $[IrCl_6]^{2-}$ generated by electrochemical oxidation of $[IrCl_6]^{3-}$ in a thin layer cell arrangement is considered.[3] Both potential step (chronoamperometric) and CV experiments have been performed, during which the absorption spectrum within the evanescent field was continuously measured in the region 510-570 nm using EW-BB-CEAS. In order to improve the spectral range

and the time resolution, the high-reflectivity cavity mirrors were then replaced with broadband coated mirrors.

7.2 Experimental Section

7.2.1 EW-BB-CEAS apparatus

Figure 7.1 shows the experimental arrangement. The cavity mirrors were either two highly reflective concave mirrors (Layertec. R_{550nm} > 99.99 %, 1 m radius of curvature) or two broadband coated mirrors (R > 99.85 % in the range of 400 – 850 nm,1 m radius of curvature) and were arranged together with a custom fused silica prism in a folded cavity configuration.[2] The total internal reflection angle was 75 degrees, slightly greater than the critical angle for the silica-water interface (66 degrees). A liquid cell within which electrochemical experiments were performed was mounted above the prism.
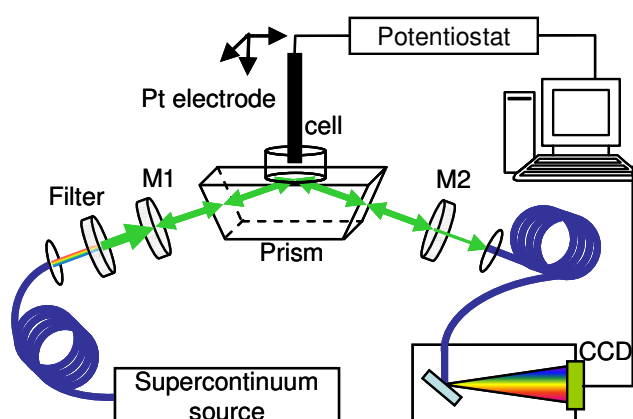

Figure 7.1: The broadband evanescent-wave cavity enhanced spectrometer employing supercontinuum radiation for detection at the silica-water interface. For clarity only the working electrode is shown.

The optical cavity was filled with broadband light from a commercial SCR source: 5 ps pulse length fibre laser operating at 10 MHz (Fianium SC400). The output power was 2 W with bandwidth 400 - 2500 nm. In most measurements, it was spectrally filtered to a bandwidth of 70 nm centred around 535 nm, to match the mirror reflectivities and to avoid saturation of the detector. After filtering, the total optical power was 9 mW. Light escaping through the back mirror (M2) was coupled via an optical multimode fibre into a grating spectrometer (PI Acton SP2300) equipped with a 1340×400 pixel CCD camera (PI Acton Pixis 400B). The signal was typically integrated for 0.5 s.

For the measurements involving the broadband mirrors, the signal was integrated for 10 μs at a repetition rate of 606 Hz and measured with an Andor Shamrock SR-303i imaging spectrograph (wavelength range 533 nm centred at 546 nm) which was attached to a cooled CCD camera (Andor iXon, 512 x 512 pixels).

7.2.2 Electrochemical measurements

Experiments were performed in a thin layer electrochemical cell arrangement with a circular 2 mm diameter platinum working electrode. The electrode was aligned between 100 and 150 ($\pm$10) μm above the evanescent field as described in previous chapters. To permit CV and chronoamperometric (potential step) experiments, a platinum wire counter electrode was employed with a chlorinated silver wire acting as a quasi reference electrode. The cell contained a solution of 10 mM $[IrCl_6]^{3-}$ in

0.1 M KNO_3(aq) (as supporting electrolyte). Electrochemical generation of $[IrCl_6]^{2-}$ was achieved by stepping the potential from 0.3 to 0.8 V *vs*. Ag/AgCl for various step times (typically 10 -120 s) or by sweeping the potential at various scan rates.

7.3 Results and Discussion

7.3.1 UV-vis Spectroscopy

Figure 7.2 shows the UV-visible absorption spectra of 0.5 mM $[IrCl_6]^{3-}$ and $[IrCl_6]^{2-}$ solutions. The spectral window for the first set of experiments, limited by filters and mirrors available, was 510-570 nm. The necessary reference spectrum required for CEAS was obtained with pure water and the spectrum of the $[IrCl_6]^{3-}$ solution in the cell was recorded before and after each electrochemical experiment to compensate for any drift in the intensity or spectrum of the SCR source.
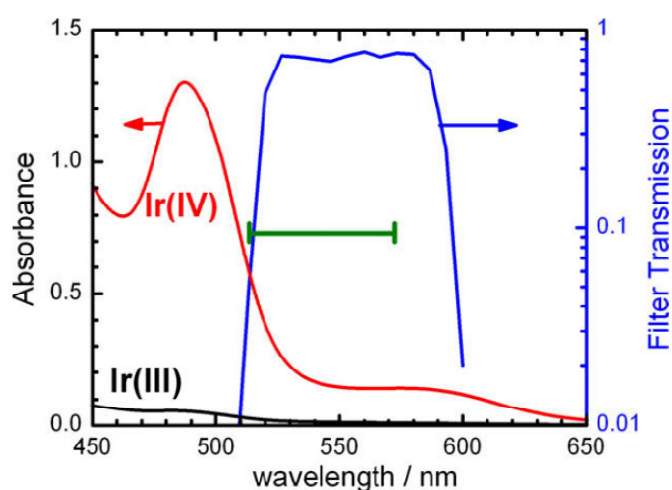

Figure 7.2: UV-vis spectra of 0.5 mM $[IrCl_6]^{3-}$ (black) and $[IrCl_6]^{2-}$ (red) solutions. The blue curve indicates the spectrum of the filtered supercontinuum radiation and the green

line the region of high mirror reflectivity for the first set of EW-BB-CEAS experiments (R>0.999).

7.3.2 EW-BB-CEAS Experiments

Figure 7.3a shows the evolution of the interfacial optical absorption spectrum during a chronoamperometry experiment using the high reflectivity mirrors, as the working electrode was stepped for 120 s from 0.3 V to 0.8 V and back. The high absorbance below 540 nm matches the $[IrCl_6]^{2-}$ absorption feature (Figure 7.2). The $[IrCl_6]^{2-}$ concentration within the evanescent field reaches a maximum after *ca.* 50 s when all $[IrCl_6]^{3-}$ in the thin layer cell has been oxidised. After 120 s, the potential was stepped to open circuit and $[IrCl_6]^{2-}$ diffuses out of the thin layer cell resulting in a slow decay of the interfacial absorbance.

Figure 7.3b shows the interfacial spectrum recorded during a CV in which the potential was swept from 0.3 V to 0.9 V (*vs*. Ag/AgCl) and back at 5 mV s^{-1}. Again, the optical absorbance increases as the electrode potential is taken in the anodic direction, but decreases on the return sweep as the $[IrCl_6]^{2-}$ is actively reduced at the electrode. The optical response trails the electrode potential by a few seconds as the electrochemically generated $[IrCl_6]^{2-}$ diffuses across the cell into the evanescent field.
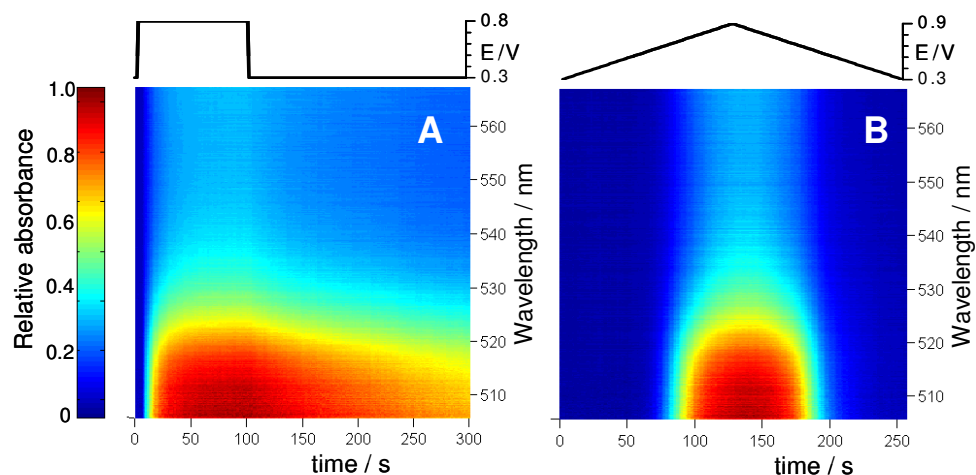
Figure 7.3: Contour plots of the interfacial absorption spectra of electrogenerated $[IrCl_6]^{2-}$ as a function of time during (A) a chronoamperometric step experiment and (B) a CV experiment.

To illustrate the quantitative nature of these measurements, Figure 7.4a shows the $[IrCl_6]^{2-}$ concentration, derived from the $\lambda = 520$ nm data, as a function of time during a 120 s potential step experiment. The current was measured simultaneously with the EW-BB-CEAS signal and gives information on the mass transport of $[IrCl_6]^{3-}$ to the electrode. Finite element simulations, performed as described in Chapter 3 and in an earlier paper,[3] were carried out in order treat to mass transport (diffusion) in the thin layer cell arrangement and are in good agreement with the experimental data. The absorbance reaches a plateau after *ca.* 50s, once all $[IrCl_6]^{3-}$ has been oxidised within the thin layer. Figure 7.4b shows the time evolution of the interfacial $[IrCl_6]^{2-}$ concentration during the CV (0.3 V to 0.8 V vs. Ag/AgCl at 5 mV s^{-1}). Again, the simulated concentration and current transients are in good agreement with the experimental data.
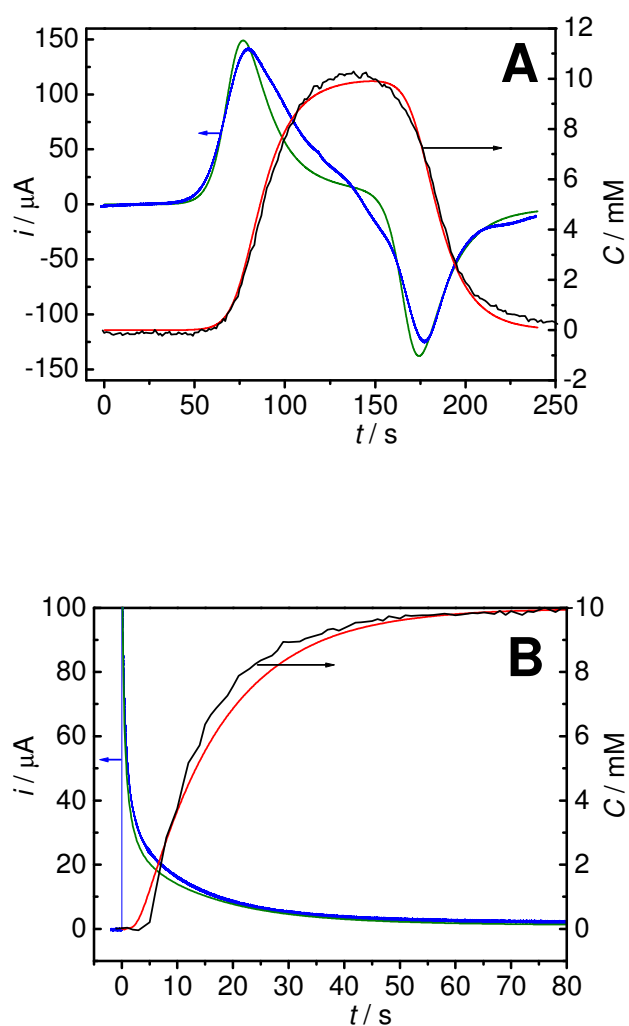
Figure 7.4: Measured (black) and simulated (red) interfacial $[IrCl_6]^{2-}$ concentration during (A) a 120 s chronoamperometry experiment (120 s at 0.8 V vs. Ag/AgCl) and (B) a CV (5 mV s^{-1}). The measured (blue) and simulated (green) current transients are also shown.

In this initial demonstration, depending on the wavelength, the light undergoes *ca.* 60-95 round trips of the cavity before the intensity falls by a factor 1/e. The sensitivity can be estimated[14] in terms of the minimal detectable extinction coefficient, $(\alpha l)_{min}$, which averages 1.4 x 10^{-5} over the spectral range of these experiments with a peak of 6.8 x 10^{-6}. For the effective path length of *ca.* 1µm,[3] the minimum detectable $[IrCl_6]^{2-}$

163

concentration for a 0.5 s acquisition, is 57μM - equivalent to detecting

5.7 nM $[IrCl_6]^{2-}$ in a conventional 1cm cuvette in the same time.

In order to extend the wavelength range, the high reflectivity

mirrors were replaced with broadband coated cavity mirrors. Figure 7.5A

shows the signal (I) and reference (I_0) spectra as measured by the

spectrometer with a solution of 10 mM $[IrCl_6]^{2-}$ in the cell above the prism.

The measurements were taken every 10 ms and the displayed spectra are

averaged 200 times (*i.e.* 2 s accumulation time). The reflectivity of the

broadband mirrors is not constant over the whole wavelength range. This

effect manifests itself in the two spectra where the transmission of light is

highest at the minima of the mirror reflectivity. Figure 7.5B shows the

relative absorbance spectrum of the 10 mM $[IrCl_6]^{2-}$ solution extracted from

the reference and signal intensity spectra from Figure 7.5A. By taking into

account a UV-vis spectrum (which is scaled for the spectral variation in the

effective thickness), the spectrum can be calibrated to obtain absolute

absorbance values from the ratio between the scaled UV-vis spectrum and

the raw CEAS spectrum, the overall loss per roundtrip can be obtained.

This loss spectrum has contributions from the oscillations of the mirror

reflectivity but is dominated from other losses, especially at higher

wavelengths. These losses most certainly arise from scattering both at the

prism surfaces and within its bulk. Other prominent features in the loss

spectrum appear at 478 nm and 547 nm. The origin of these features is

unclear but might be attributed to absorbance or etaloning with the cavity

mirrors. However, to prove this, more investigations would be required.
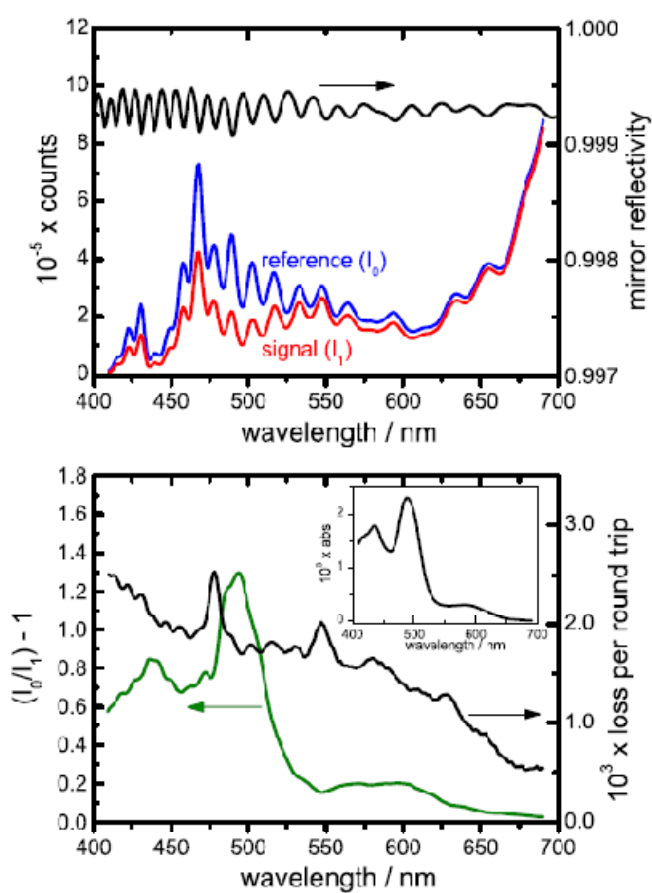
Figure 7.5: A) Raw reference and signal spectra recorded for a sample of 10 mM $[IrCl_6]^{2-}$ using the broadband coated mirrors. The mirror reflectivity as a function of wavelength is shown above. B) The extracted relative absorbance spectrum for the 10 mM $[IrCl_6]^{2-}$ solution. The loss per round trip with in the CEAS folded cavity was extracted by taking the ratio of the signal to the (single pass) UV-vis spectrum of 2 mM $[IrCl_6]^{2-}$ scaled for the (wavelength dependent) effective thickness (inset).

Figure 7.6A shows a contour plot for the electrochemical generation of $[IrCl_6]^{2-}$ in the same thin layer cell arrangement (100 μm) as described above, but for a wavelength range of 400 – 700 nm. The spectra have been corrected for the changes in the mirror reflectivity (*vide infra*) using UV-vis spectroscopy). Similar to Figure 7.3, the spectrum evolves after a certain lag time which is caused by the diffusion of $[IrCl_6]^{2-}$ to the prism

surface. After 60 s, when the potential is stepped back, the spectral features disappear again. However, in this experiment the wavelength range is greatly increased. Additionally, the spectral accumulation time was 10 μs at a repetition rate of 606 Hz which was limited only by the data acquisition from the CCD array. For purposes of plotting, a 6 times average on the data was taken. The spectral (b) and temporal (c) cuts exemplify the high signal to noise ratio, even at this very repetition rate. The effective minimum detectable absorbance is 3.9 x 10^{-5} at the peak of the absorbance spectrum.

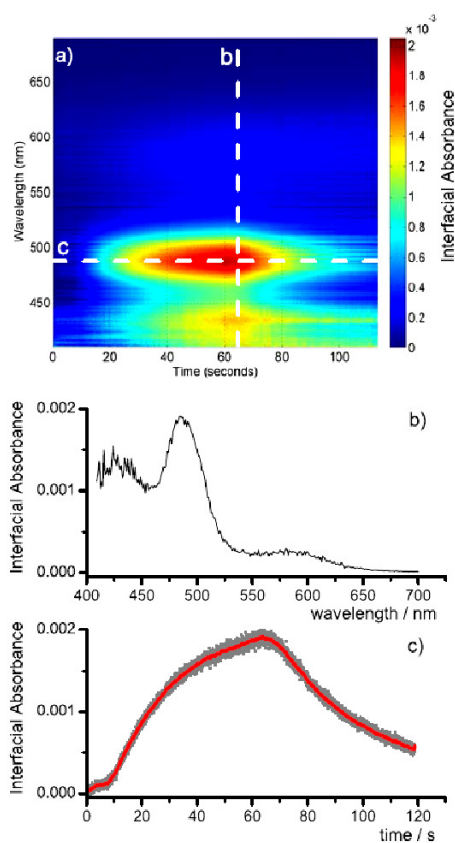Figure 7.6: a) Contour plot of the interfacial absorbance spectrum as a function of time during electrochemical generation of $[IrCl_6]^{2-}$ in a 100 mm electrochemical cell. The repetition rate for data accumulation was 10 μs. b) spectral cut at 65 s and c) temporal cut at 478 nm through the contour plot.

7.4 Conclusions

We have demonstrated an evanescent wave variant of broadband cavity enhanced spectroscopy which proves to be a sensitive technique for detecting electrogenerated species within a thin layer cell, specifically at interfaces. Use of a supercontinuum radiation source provides a significant multiplex advantage over narrow spectral line width experiments by enabling the whole absorption spectrum of species within the evanescent field to be recorded essentially continuously. The high spectral brilliance of the SCR source yielded acceptable signal to noise (>100:1) with 0.5 s accumulation. In turn, the cavity enhancement increases the sensitivity of the instrument through the multiple passes it induces. This powerful combination of broadband spectral information coupled with high spatial and temporal resolution will find a myriad of applications in monitoring surface reactions such as nucleation, dissolution and interfacial charge propagation.

The spectral window accessible in this study was initially limited to 70 nm by the mirrors and filters that were available but further measurements showed that it is possible to extend EW-BB-CEAS to the full visible range using broadband coated mirrors. It was found that the repetition rate could be increased up to 606 Hz, which opens up the possibility to study relatively fast interfacial kinetics. Even under these challenging conditions, the minimum detectable absorbance is $< 5 \times 10^{-5}$. As with EW-CRDS, the technique will be a particularly sensitive probe of interfacial processes such as adsorption and related phenomena. This will

open up many more possibilities of new applications not only in electrochemistry but also in the fields of physics, material sciences and chemical biology.

7.5 References

(1)   Engeln, R.; Berden, G.; Peeters, R.; Meijer, G. *Review of Scientific Instruments* **1998**, *69*, 3763-3769.

(2)   Everest, M. A.; Black, V. M.; Haehlen, A. S.; Haveman, G. A.; Kliewer, C. J.; Neill, H. A. *Journal of Physical Chemistry B* **2006**, *110*, 19461-19468.

(3)   Mazurenka, M.; Wilkins, L.; Macpherson, J. V.; Unwin, P. R.; Mackenzie, S. R. *Analytical Chemistry* **2006**, *78*, 6833-6839.

(4)   Pipino, A. C. R.; Hudgens, J. W.; Huie, R. E. *Chemical Physics Letters* **1997**, *280*, 104-112.

(5)   Fiedler, S. E.; Hese, A.; Ruth, A. A. *Review of Scientific Instruments* **2005**, *76*.

(6)   Islam, M.; Seetohul, L. N.; Ali, Z. *Applied Spectroscopy* **2007**, *61*, 649-658.

(7)   Ruth, A. A.; Lynch, K. T. *Physical Chemistry Chemical Physics* **2008**, *10*, 7098-7108.

(8)   Stelmaszczyk, K.; Fechner, M.; Rohwetter, P.; Queisser, M.; Czyzewski, A.; Stacewicz, T.; Woste, L. *Applied Physics B-Lasers and Optics* **2009**, *94*, 369-373.

(9)   Stelmaszczyk, K.; Rohwetter, P.; Fechner, M.; Queisser, M.; Czyzsewski, A.; Stacewicz, T.; Woste, L. *Optics Express* **2009**, *17*, 3673-3678.

(10)   Alfano, A. R. *The Supercontinuum Laser Source*, 2nd ed.; Springer: New York, 2006.

(11)   Kaminski, C. F.; Watt, R. S.; Elder, A. D.; Frank, J. H.; Hult, J. *Applied Physics B* **2008**, in press.

(12)   Langridge, J. M.; Laurila, T.; Watt, R. S.; Jones, R. L.; Kaminski, C. F.; Hult, J. *Optics Express* **2008**, *16*, 10178-10188.

(13)   Ranka, J. K.; Windeler, R. S.; Stentz, A. J. *Optics Letters* **2000**, *25*, 25-27.

(14)   Fiedler, S. E.; Hese, A.; Ruth, A. A. *Rev. Sci. Instrum.* **2005**, *76*, 7.

8 Conclusions

The aim of this thesis was to develop and apply a novel analytical spectroscopic method, EW-CRDS in order to study a wide range of interfacial phenomena. To accomplish this, several variations of these instruments were built. Chapter 3 addressed the construction of the EW-CRDS instrument used for most experiments in this thesis. However, in order to extend this technique, some modifications (especially concerning the light source) were made. For example, the electrochemical reduction of immobilised cytochrome c on silica was studied using a frequency doubled Ti-Saphire laser. This enabled kinetic measurements at a different wavelength, in this case at 400 nm. By employing a SCR source, measurements of spectra covering the whole visible range are possible without restriction of temporal resolution.

Chapter 1 described the evolution of CRDS from a gas phase spectroscopic tool for trace analysis into a surface sensitive technique which can be used to probe reaction kinetics in the condensed phase. Also, the latest developments of EW-CRDS were summarised in this chapter, as well as some basic aspects about tapping mode AFM and electrochemical techniques which in conjunction with our version of EW-CRDS provide an insight into surface kinetics. Information about the actual experimental

setup used for most measurements, alignment procedures and descriptions of most optical and electronic components were included in chapter 3.

In order to demonstrate the ability of EW-CRDS to follow time-dependent surface kinetics, it was shown in chapter 4 that one can follow the Ag nanoparticle adsorption onto a PLL-modified silica prism in real time. By carrying out complementary AFM measurements, it was possible to measure the corresponding surface coverage very accurately (down to a few tens of nanoparticles per μm^2). It was also shown that the EW-CRDS technique can be used to follow the oxidative dissolution of Ag nanoparticles immobilised on the prism. The nanoparticles were dissolved by electrochemically generated Ir(IV) in a thin layer cell configuration using a 2 mm diameter Pt working electrode. The detected change in the absorbance (due to the change of size of the nanoparticles) could be correlated to a heterogeneous rate constant for dissolution which was found to be 2.8 x 10^{-3} cm s^{-1}. In addition to this electrochemical approach of dissolution using a redox mediator, the nanoparticles could also be dissolved using convective delivery of the oxidant by employing a microcapillary setup. In summary it was shown in this chapter that chronoamperometric and convective induced surface kinetics on chemically inert surfaces such as silica and polymer-modified silica can be accurately followed in real time by EW-CRDS.

In Chapter 5 we demonstrated that the oxidative surface polymerisation of aniline can be followed *in situ* by EW-CRDS. The polymerisation was initiated using aniline hydrochloride at various concentrations. Hemispherical PAni nanoparticles were formed on the

silica prism immediately after addition of the oxidant. *Ex situ* AFM was carried out on samples at various polymerisation times. Using the height measurements of the AFM images, the absorbance could be correlated to the nanoparticle radius, thus providing the possibility to obtain the polymerisation rate constant for the aniline polymerisation using a simple theoretical model. It was found that the reaction was first-order in aniline (with 0.12 M sodium persulfate). The rate constant was found to be is $0.7 (\pm 0.4) \times 10^{-7}$ cm s^{-1} in the limit of large PAni nanoparticles. Interestingly, the polymerisation rate constant was found to be larger for the small nanoparticles and decreasing monotonically with increasing nanoparticle size. The maximum value for very small particles (at the initial stage of polymerisation) was *ca.* $2.7 (\pm 1.1) \times 10^{-7}$ cm s^{-1}. This effect might be attributed to size-dependent polymerisation kinetics, but could also be explained, at least partly, by a change in the particle morphology (since the model assumes the formation hemispherical nanoparticles) or the adsorption of oligomers. These initially adsorbed molecules would initially cause a large absorbance value at short times which then would decrease with time by subsequent desorption from the prism surface.

The experiments described in chapters 4 and 5 were carried out using a diode laser at 405 nm. As a new direction, chapter 6 described the application of EW-CRDS employing a different type of laser in order to increase the flexibility in terms of different available wavelengths. In this setup, frequency doubled laser light from a Ti-Saphire laser ($\lambda = 400$ nm, pulse duration: 40 fs) was used. It was shown that the signal-to-noise ratio for individual ring-down traces was considerably larger compared to the

conventional diode laser setup used for measurements in chapters 4 and 5. As an example, this EW-CRDS setup was used to investigate the redox properties (ET kinetics) of immobilised cytochrome c on fused silica in combination with chronoamperometry (similar as described in chapter 4). These measurements were possible, because the absorption spectra of the two redox forms of cytochrome c are sufficiently different. Especially at the wavelength used in the EW-CRDS experiment (400 nm), the extinction coefficients for the oxidised form of cytochrome c is considerably higher than for the reduced form. The ET rate constant between the cytochrome c and the redox mediator FeEDTA^{2-} was determined using finite-element modelling and was found to be 4.3 ($\pm$0.6) x 10^{-9} cm s^{-1} (which corresponds to a second-order rate constant of 2.7 ($\pm$0.6) M^{-1} s^{-1}).

A new way to obtain more spectral information is described in chapter 7. Broadband cavity enhanced spectroscopy was employed using radiation from a SCR source in order to record whole absorption spectra at the silica / liquid interface. Although less sensitive to absorbance changes in the evanescent field, this novel variant still provides high temporal resolution and a significant multiplex advantage over narrow spectral line width experiments. The minimum detectable absorbance is < 5 x 10^{-5} even with broadband coated mirrors. In proof-of-concept experiments, Ir(IV) was generated from Ir(III) in a thin layer cell configuration (essentially the same as described in chapter 4). The absorbance spectrum of Ir(IV) diffusing into the evanescent field was detected simultaneously with the electrochemical signal. It was found that the repetition rate could be

173

increased up to 606 Hz, which opens up the possibility to study fast interfacial kinetics such as dissolution, polymerisation and crystal growth.

The advantages of EW-CRDS compared to other surface sensitive techniques are its moderate cost (relatively cheap CW diode lasers) and its possibility to measure kinetic processes on surfaces very accurately and at the same time, time resolved. The principle of EW-CRDS is based on the measurement of the decay constant of light trapped in the optical cavity rather than the measurement of the light intensity. In this way, the sensitivity is not compromised by temperature or pressure changes and intensity fluctuations of the laser source. Both ATR and EW-CRDS provide measurements of optical losses originating from molecular absorption or scattering caused by local changes in the refractive index within the region of the evanescent field. However, a particular benefit of EW-CRDS is the increased pathway of light which enables much higher sensitivity compared to ATR and also provides spatial resolution since the surface is always probed in the same spot as well as operating on a faster timescale. It is also possible to investigate surface reactions in real time and monitor polarisation dependencies of adsorbed molecules simultaneously without having to make compromises in terms of sensitivity. Combinations with other techniques such as electrochemistry, SECM and flow techniques are very easy and convenient to implement.

There are techniques with higher sensitivity compared to EW-CRDS, such as QCM and ellipsometry, but these techniques either do not discriminate between different adsorbing species (QCM) or require extensive modelling to obtain quantitative information about surface

coverages. Also, ellipsometry as well as reflectometry rely on the fact that the probing light source is illuminating from the top which requires the design of special cells or cuvettes if one wants to carry out measurements *in situ*.

Limitations of the EW-CRDS techniques are the restriction of the substrate to silica or glass, since there has to be a significant difference in the refractive indices of the two media where TIR should occur. However, the surface can be modifying with polymer films or other transparent materials (at the wavelength of the employed laser) in order to open-up more possibilities for studies at solid liquid interfaces. Another drawback is that in many variants of EW-CRDS one is also bound to use a specific wavelength, since the sensitivity (and noise) depends strongly on the optical losses of all optical elements involved in the optical cavity such as narrowbanded high reflective mirrors, scattering losses in the prism and anti-reflective coatings.

In summary, this thesis showed that EW-CRDS either on its own or in combination with electrochemical or flow methods is a powerful new tool to monitor surface reactions in real time. Future investigations could be more focused on biological systems, such as lipid bilayers and membranes and could involve molecular adsorption experiments and lateral H^+ diffusion in combination with SECM. Also, Carbon nanotube network electrodes could be grown on the silica surface which enables the study of nanoparticle growth mechanisms or dye adsorption kinetics on single or multiwalled carbon nanotubes. EW-BB-CEAS, especially in conjunction with a SCR source, can yield new insights into surface kinetics

by providing information about the whole visible spectral range which opens up vast possibilities for many sensing applications.